Variationally Consistent Methods for Lagrangian Dynamics in Continuum Mechanics

by

Sudeep K. Lahiri

Submitted to the Department of Aeronautics and Astronautics
in partial fulfillment of the requirements for the degree of

Doctor of Philosophy

at the

MASSACHUSETTS INSTITUTE OF TECHNOLOGY

May 2006
[June 2006]

Author _____
Department of Aeronautics and Astronautics
May 26, 2006

Certified by _____
Jaime Peraire
Professor of Aeronautics and Astronautics
Thesis Supervisor

Certified by _____
Javier Bonet
Professor of Civil Engineering
University of Wales, Swansea, UK

Certified by _____
David L. Darmofal
Associate Professor of Aeronautics and Astronautics

Certified by _____
Raul Radovitzky
Assistant Professor of Aeronautics and Astronautics

Accepted by _____
Jaime Peraire
Professor of Aeronautics and Astronautics
Chair, Committee on Graduate Students

Variationally Consistent Methods for Lagrangian Dynamics in Continuum Mechanics

by

Sudeep K. Lahiri

Submitted to the Department of Aeronautics and Astronautics
on May 26, 2006, in partial fulfillment of the
requirements for the degree of
Doctor of Philosophy

Abstract

Rapid dynamics are commonly encountered in industrial applications such as forging, crash tests and many others. These problems are typically non-linear due to large deformations and/or non-linear constitutive relations. Such problems are typically modelled from a Lagrangian viewpoint, where the mesh is attached to the body; hence, large deformations lead to large distortions in the mesh. Explicit numerical methods are considered to be efficient in these cases where large meshes and small time-steps are employed for spatial and temporal resolution. However, incompressible and nearly incompressible materials pose a problem as the timestep stability restriction in explicit methods becomes increasingly severe.

Most of the numerical methods employed for such simulations, are developed from discretization of the equations of motion. Recently, Variational Integrators have been developed where the numerical time integration scheme is developed from a variational principle based on Hamilton's principle of stationary action. Such methods ensure conservation of linear and angular momentum, which lead to more physically consistent simulations.

In this research, numerical methods addressing incompressibility and mesh distortions have been developed under a variational framework. A variational formulation for mesh adaptation procedures, involving local mesh changes for triangular meshes, is presented. Such procedures are very well suited for explicit methods, without significant expense. Conservation properties of such methods are proved and demonstrated. Further, a Fractional Time-Step method is developed, from a variational framework, for incompressible and nearly incompressible problems. Algorithmic details are presented, followed by examples demonstrating the performance of the method.

Thesis Supervisor: Jaime Peraire
Title: Professor of Aeronautics and Astronautics

ya nisha sarva-bhutanam, tasyam jagarti sanyami |

yasyam jagrati bhutani, sa nisha pashyato muneh ||

... Shrimad Bhagavad Gita

Chapter 2.

"What is night for all beings, is the time of awakening for the self-controlled; and the time of awakening for all beings, is night for the introspective sage."

I dedicate this thesis to my mother Mrs. Namita Lahiri

and my father Mr. Salil Kumar Lahiri.

Acknowledgments

It has been a privilege to be a part of MIT. I am indeed indebted to be in the PhD program at the department of Aeronautics and Astronautics.

I am grateful to my advisor, Prof. Jaime Peraire who has guided me all along the course of the program with great patience and enthusiasm. I am also grateful to Prof. Javier Bonet, (University of Wales, Swansea, UK.) who as been like a co-advisor to me all through my research. Both of them have given me directions and advice without which this thesis would not have completed. I am indebted to them for introducing me to the world of variational integrators and mesh adaptation.

I would like to thank Dr Jim Stewart, from Sandia National Laboratory, for the research discussions and support to the project. I am indebted to the financial support from Sandia National Laboratory, USA.

I would also like to thank various faculty members of the department, especially Prof. Raul Radovitzky, with whom I had many insightful discussions regarding my research and continuum mechanics in general. I would also like to thank various faculty members like Prof. Mark Drela (Aero-Astro., MIT), Prof. K. J. Bathe (Mech. E., MIT), Prof. Simona Socrates (Mech. E., MIT) and Prof. John Hutchinson (Harvard University) whose teaching and course-work, helped me build my background in the area of continuum mechanics. I would especially like to thank Prof. Steven Hall, and the department of Aeronautics and Astronautics, for providing a great opportunity by offering a Graduate Teaching Fellowship for the course of Unified Engineering in the department. It was really a privilege to be the part of the Unified Staff and the teaching workshops conducted by Prof. Paul Lagace was highly thought provoking.

I am also grateful to be a part of ACDL (Aerospace Computational Design Laboratory) for creating such a nice and conducive academic and research environment, which helped me endure the challenges of the PhD program with sanity. I would like to thank Mr. Bob Haimes, who has been a great source of learning for me, from whom I learned a lot of programming and associated issues. I would like to thank Jean Sofranos, for her help in schedules and various lab activities. I would particularly like to thank all my co-students

at ACDL, interacting with whom was a great source of learning and fun. I would like to remember the company of my co-students like David Venditti, Victor Garzon, Tolulope Okusanya, Giuseppe Alescio, James Lu, Sean Bradshaw and especially David Willis as great moments of sharing, interactive learning and hectic activity. Discussions ranged from computations to mathematics, physics, politics, sports(cricket), society etc., which was indeed very educative, as well as very befriending. It was also enriching to interact with some of the new members, Garrett Barter, Krzysztof Fidkowski, Todd Oliver, Theresa Robinson and Tan Bui, who are very enthusiastic and are really very helpful and friendly. I would especially like to thank Garrett, Krzystoff and Todd, for their active support not only to me but to the whole lab in affairs of software support.

It has been a great experience in the department of Aeronautics and Astronautics, with great staff members, like Marie Stuppard and Barbara Lechner, who have been extremely nice and considerate to students' issues, without whose support, graduate study would have been very inconvenient.

Finally and most importantly I would like to thank my mother Mrs. Namita Lahiri, and my father Mr. Salil Kumar Lahiri, for their blessings and active support all through my academic career and life so far, without whose sacrifices and initiatives, it would have been extremely hard to avail such a great opportunity of learning and experience. I would also like to thank my sisters and my entire family who have been really concerned and helpful in my activities.

Contents

List of Figures

List of Tables

Chapter 1

Introduction

Rapid dynamics encompasses a significant section of continuum mechanics problems. Several industrial phenomena involve rapid dynamics of solids, for example forging, machining, crash-tests, collision modelling and many others. Computational simulations of such problems are used in various engineering analysis and design. These problems involve large deformations and rotations along with complex material behaviour. Hence these problems are inherently non-linear. Due to high velocities (of the order of speed of sound in the material), large meshes and many small time-steps are used for spatial and temporal accuracy. Hence explicit time-integrators become advantageous in such applications. Several codes have been developed and used for such problems [1, 2, 3, 4], based on explicit methods. The main challenges in these numerical problems lie in the proper modelling of large deformations and rotations, modelling of contact, and modelling of complex non-linear material behaviour. Explicit methods have a maximum allowable time-step limitation from stability considerations, which inversely depends on the fastest wave speed in the material. In case of nearly incompressible materials, the fastest wave speed becomes very large, causing the maximum allowable time-step to be very small. In case of completely incompressible materials explicit methods cannot be used. Thus incompressibility poses problems in use of explicit methods. One way to address this problem due to incompressibility is by using mixed formulations, where pressure is an additional degree of freedom. Mesh distortions, encountered due to large deformations/rotations lead to lack of accuracy of the solution. Problems due to mesh distortions have been addressed by mesh adaptation.

An important aspect of a time-integration method in dynamics applications is its ability to conserve mass, momentum (linear and angular) and energy, which leads to more physically consistent solutions. Methods which do not have good conservation properties, develop large errors under long time-integrations. Typically dynamics in solids are modelled from a Lagrangian formulation of the equations of motion. Hence mass conservation is automatically satisfied in such methods. Exact conservation of global energy is hard to obtain. But global momentum (linear and angular) conservation is possible. The explicit time-integrator, the Central Difference Scheme (also called the Leap-Frog Method in fluid mechanics), is found to conserve global momentum exactly. Existing codes [3, 4] have employed this method with great success.

Recent research [5] has shown that time-integration methods developed from a variational principle as that of Hamilton's principle of stationary action, necessarily conserve linear and angular momentum. Such methods are commonly called as **Variational Integrators** or **Variational methods**. The existing methods for mesh adaptation and mixed formulation (to address incompressibility) used so far in present codes, are not derived from a variational principle. Hence momentum conservation is not ensured in such methods. In this thesis, the development of mesh adaptation and mixed formulation from a Variational principle is presented.

1.1 The problem

Mesh distortion is an important problem in simulation of dynamics involving large deformations and rotations. Mesh adaptive updates can be used to reduce mesh distortions. Such use of adaptation has been limited, since these updates add errors to the solution. Existing mesh-adaptive updates do not ensure conservation of momentum which lead to errors over many time-integration steps. Hence, it is desired that such mesh updates conserve global momentum which would allow use of adaptation in reducing mesh distortions and also increase the accuracy of the solution.

Mixed formulations, where pressure is an additional unknown, are used to handle incompressibility. Several methods exist to handle incompressible material behaviour [6]. Most of

these methods are derived from discretizing the equations of motion, therefore, these methods do not ensure conservation of momentum. Hence, a variationally consistent method employing a mixed formulation that ensures conservation of momentum is desired.

1.2 Literature review

1.2.1 Variational Framework

Variational integrators have been developed by several researchers [5, 7, 8, 9, 10, 11, 12, 13], on the basis of Hamilton's principle of stationary action, rather than discretizing in time the differential equations of motion. Hamilton's principle dictates that the path followed by a body represents a stationary point of the action integral of the Lagrangian over a given time interval [14, 15]. Variational integrators take advantage of this principle by constructing a discrete approximation of this integral which then becomes a function of a finite number of positions of the body at each timestep. The stationary condition of the resulting discrete functional with respect to each body configuration leads to time stepping algorithms that retain many of the conservation properties of the continuum problem. In particular, the schemes developed in this way satisfy exact conservation of linear and angular momentum [5]. In addition, these algorithms are found to have excellent energy conservation properties even though the exact reasons for this are not fully understood [5, 16, 17, 18]. This class of variational algorithms includes both implicit and explicit schemes, and in particular, it includes some well-known members of the Newmark family [19]. A recent development in the area of variational integrators, is the development of asynchronous variational integrators [10]. The discrete energy gets computed as the variation of the Lagrangian with respect to the time-step. By altering the time step locally, it has been shown in [10], that variational integrators could have both momentum and energy conserving properties but at the cost of being asynchronous. In the research presented in this thesis, the focus will be on synchronous time-step methods, and on explicit or semi-explicit methods.

1.2.2 Mesh Adaptation

Mesh adaptation has been an active area of research in solid and fluid mechanics computations. There are three types of mesh adaptation *viz.* : (1) r-adaptation, where the number of nodes and number of elements remain same while the node locations or connectivities are changed [20], (2) h-adaptation, where the elements are refined and de-refined locally or globally [21], and (3) p-adaptation, where the order of the interpolation polynomial within the element is changed to resolve the solution locally [22]. The effectiveness of mesh adaptation depends on the mesh-adaptive-mechanism, and the adaptation criteria.

Mesh-adaptive mechanisms might include local mesh changes or global remeshing. Global mesh changes, typically involve, complete remeshing and transfer of variables from the old mesh to the new mesh [23, 24]. Local mesh changes could be achieved using explicit updates [25, 26]. Mesh changes involve node movement, changes in mesh connectivity, and coarsening and refinement of meshes. A detailed overview of such changes in meshes can be found in [27, 28]. Various such mesh update methods exist, which are used by several researchers [3, 29, 30] with success. 2D remeshing based on the advancing front methods have been used in [30] for modelling ballistic penetration problems. Severe mesh distortions encountered in 2D machining problems have been handled in [31], based on complete remeshing techniques. 2D mesh adaptation for shear bands in plane strain can be found in [32, 33] Local coarsening and refinement based on mesh size has been discussed in [29] in application to shear bands. 3D Mesh operations are discussed in [29, 27]. Mesh adaptations for metal forming can be found in [34, 35, 36]. 2D Impact problems have been modelled using global remeshing and gradient based indictors in [37]. Finally the application of mesh adaptation in shape optimization of structures is found in [38, 39].

The adaptation criteria is chosen by the analyst. Typically meshes are adapted based on either some error-estimate or mesh skewness or some output of interest. Various researchers [40, 41, 42, 43, 44, 23, 45] have described different error estimation techniques in their works. A commonly used error estimate by Zienkiewicz and Zhu, [46, 47], (Z^2 error estimate), uses the stresses within the element and describes a recovery process to obtain a reference stress. The difference of the reference and the elemental stresses, pro-

vides for an error estimate. This type of error indicator can be classified under gradient based errors indicators. Curvature based error-estimates have been used by [33], in problems of large plastic strain damage. Another approach has been found in [24, 32, 30] where gradients in direct physical quantities like the velocity field or strain field or other choice of quantities are used as empirical adaptation criteria. Recently, [48, 49, 50] have developed a new approach for error-estimation based on the constitutive relation error. They describe the finite element solution as a displacement-stress pair $(\hat{\boldsymbol{U}}_h, \hat{\boldsymbol{\sigma}}_h)$ such that the displacements satisfy kinematic constraints like boundary conditions and initial conditions while the stresses satisfy the equilibrium conditions. The displacements and stresses do not satisfy the constitutive relations (stress-strain relations) which provides an error measure which they refer to as the constitutive relation error. This error measure has been found to be effective in large strain transient problems. Similarly error-estimators based on the time update (using semi-discrete equations of motion) are formulated in [51]. Error estimates based on variational constitutive updates can be found in [23]. Variational mesh adaptation, where the error-estimate is obtained from a variational principle is found in [23, 52, 53, 54]. Recently, some researchers [39], have used the idea of configurational forces [55] for r-adaptation, for applications in shape optimization. Configurational forces are obtained as a variation of the internal energy with respect to material position vectors. This leads to the criteria to move mesh points to obtain an optimal mesh, which also leads to shape optimization. An overview of various error-estimation techniques and adaptation criteria can be found in [45, 56].

Significant research has been done in the fluid mechanics community in the area of mesh adaptation, where the main emphasis has been in proper resolution of the flow field, especially in the simulation of boundary layers, shock waves and high speed compressible flows. Several researchers like [57, 58, 59, 60, 61, 62, 63] have developed very effective mesh adaptative solvers for compressible flows. Most of these adaptations are based on error-estimates which are based on gradients of flow properties. Use of error estimators based on bounds on functional outputs [64, 65] have also proven to be very effective in the calculation of important aerodynamic properties like lift or drag of an airfoil in presence of shocks and viscous effects.

1.2.3 Incompressibility

Explicit methods perform poorly near the incompressibility limit. Explicit methods have a stability condition due to which the time-step size for time integration has to be smaller than a maximum allowable time step size dependent on the wave speeds. Near incompressibility, the material wave speeds approach infinity, leading to very small maximum allowable time-steps. Explicit methods cannot be used in case of full incompressibility (Poisson's ratio equal to 0.5). In Eulerian fluid dynamics, incompressible flows are often modelled using fractional time integration schemes [66], where the pressure is integrated in time in an implicit manner. In Eulerian fluids, incompressibility poses linear constraints on the velocity field (divergence free), but in case of displacement formulations, incompressibility constraints are non-linear. Yet, extending some of these ideas to solids by introducing the pressure as an additional variable has been attempted in [6, 67, 68, 69] using linear tetrahedral elements. In both these references, however, the motivation for treating pressure as a problem variable was to eliminate the well-known problem of volumetric locking encountered by the standard linear triangular and tetrahedral elements. Unfortunately, the pressure step was taken explicitly and the resulting critical time-step was much smaller than that obtained with standard integration [69]. Previous researchers [70] have developed similar methods for solid dynamics using fully implicit schemes. Although such methods are unconditionally stable they become very expensive for large size problems.

1.3 The Objective

The objective of this thesis is two fold:

1. To develop mesh adaptive time integration methods which conserve linear and angular momentum.

2. To develop a time integration algorithm for incompressible and nearly incompressible materials which conserves linear and angular momentum.

A variational framework was adopted as the fundamental approach for development of these methods, which ensured conservation of linear and angular momentum [5, 71].

1.4 Thesis Overview

In Chapter 2, the variational framework and the related details are presented. Examples by deriving a few numerical methods are presented, followed by proofs of conservation properties. Then, the details of space-time discretization are presented. Derivation of the simple leap frog method using space-time discretization is shown as an example. A variationally consistent, stabilized element formulation is presented, which leads to better control for long time simulations.

In Chapter 3, the space-time discretization and the variational formulation are extended to incorporate local mesh adaptations. Local remeshing is achieved by four local operations, *viz.*: (1) Diagonal Swapping, (2) Edge Splitting, (3) Node Movement and (4) Edge Collapsing. Details of the above mechanisms are presented individually. Then, implementation details of error-estimation, and adaptation criteria are mentioned followed by examples demonstrating the performance of the adaptation methods.

In Chapter 4, the details of the mixed formulation are described, wherein, the pressure (p), is introduced as an additional degree of freedom along with the position vectors, ($\boldsymbol{x}_n$). The variational formulation is presented, whereby the fractional time-step is introduced. Then, the finite element spatial discretization is used to obtain the discrete equations of motion. The underlying approximations are described, leading to the final fractional time-step algorithm. A linear stability analysis is conducted, demonstrating the stability criteria of the method, hence demonstrating the advantage of the algorithm over standard explicit method near the incompressibility limit. Pressure stabilization for the completely incompressible case is explained followed by suitable examples. Performance and advantages of the algorithm are explained with some concluding remarks.

In Chapter 5, the variational formulation using node movement and a mixed formulation are revisited. The variational formulations are combined, leading to a simple mesh-adaptive fractional time-step algorithm, as listed in table 5.1. Implementation details like that of the adaptation criteria and stabilization are mentioned, followed by examples and concluding remarks.

In Chapter 6, A brief summary of the overall developments of the research is presented,

followed by guidelines on possible future work.

1.5 Contributions

1.5.1 Mesh Adaptation

Mesh adaptation has been used by many researchers, however, existing adaptive time updates were not developed to ensure conservation of linear and angular momentum. In this research, mesh adaptive updates were developed from a variational framework, using space-time discretization, which conserve global linear and angular momentum exactly. The mesh adaptation operations were developed for linear triangular elements, using only local mesh changes. The resulting algorithms were explicit, with no significant additional computational expense over standard explicit methods. Using simple adaptation criteria, mesh control was achieved, although, further developments on mesh adaptation criteria might be required for more effective mesh control in specific cases. Such explicit, momentum conserving, local mesh adaptation procedures, can be easily incorporated in to existing methods like [2] without affecting their conservation properties.

1.5.2 Fractional time-step integration method

To develop computational methods, for incompressible and nearly incompressible Lagrangian dynamics, a fractional time-step method has been developed, [71]. This method has been developed from a variational framework, hence it conserves global linear and angular momentum. Also this method provides a significant advantage over implicit methods in 3D problems. This method gives significant advantage over explicit methods near the incompressibility limit.

1.5.3 Variationally consistent stabilization

Time-integration methods, typically incur errors over long time integrations leading to inaccurate solutions after many time steps. Such methods need to be stabilized, in order to prohibit any non-physical mechanisms in the solution. A stabilized element formulation has been employed for explicit methods, which does not disturb the momentum conservation

property of a variationally consistent algorithm. Such stabilization can be used for rapid dynamics problems or even in any other dynamic simulations, where spurious modes need to be prevented or controlled.

1.5.4 Space-Time Discretization

The space-time discretization approach, developed for the variational formulation of mesh adaptation, could be extended for further development of various variational integrators or other time integration algorithms. In this research, simple linear tetrahedra have been used to discretize the space-time volume. Higher order extensions are also possible using this approach.

1.5.5 Fractional time-step Method with adaptation

A combined algorithm involving a fractional time-step method and node movement has been developed which is generically applicable to 2-D and 3-D problems. Being variationally consistent, it conserves linear and angular momentum exactly. The combined algorithm inherits the properties of the fractional time-step method. Like the fractional time step method, it has good energy conservation behaviour. The energy of the system, although not conserved exactly, remains bounded over long time integrations. This algorithm can be useful in cases of incompressible or nearly incompressible materials undergoing severe distortions. The algorithm as presented, uses simple adaptation criteria, for demonstration purposes, wherein further work is required for application in cases of large mesh distortions.

Chapter 2

Variational Formulation

2.1 The Continuous Problem

The motion under loading of a generic three dimensional body is considered. A reference configuration, $Q \subset \mathcal{R}^3$ is adopted, corresponding to the configuration of the body at time $t = 0$. The material coordinates $\boldsymbol{X} \in Q$, are used to label the particles of the body. At an arbitrary time t, the position of particle $\boldsymbol{X}$ is given by the coordinate $\boldsymbol{x}$, and in general, the motion of the body is described by a deformation mapping,

$$\boldsymbol{x} = \phi(\boldsymbol{X}, t), \tag{2.1}$$

as illustrated in figure 2-1. In its reference configuration, the body has volume V_0 and density ρ_0, whereas at a given time t, the body has volume $V(t)$ and density $\rho(t)$.

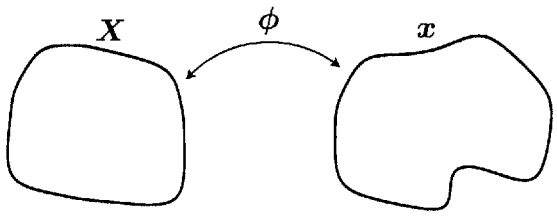

Figure 2-1: Continuous systems

2.2 The Action Integral for non-dissipative systems

For non-dissipative systems, both the internal and external forces in the system can be derived from a potential, and the motion between times $t_0 = 0$ and t, can be determine from Hamilton's principle. To this end, a Lagrangian, $\mathcal{L}$, is introduced, such that, $\mathcal{L}(\boldsymbol{x}, \dot{\boldsymbol{x}}) = K(\dot{\boldsymbol{x}}) - \Pi(\boldsymbol{x})$, where, K, denotes the kinetic energy, Π is the potential energy and $\dot{\boldsymbol{x}} = d\boldsymbol{x}/dt$ is the material velocity. The potential energy can be generally decomposed into an internal elastic component, Π_{int}, and a component accounting for the external conservative forces, Π_{ext}. Thus, $\Pi(\boldsymbol{x}) = \Pi_{\text{int}}(\boldsymbol{x}) + \Pi_{\text{ext}}(\boldsymbol{x})$.

The action integral, S, is defined as the integral of the of the Lagrangian over the time interval considered,

$$S = \int_0^t \mathcal{L}\, dt \,, \tag{2.2}$$

and Hamilton's principle states that the deformation mapping satisfying the equations of motion can be obtained by making the action integral stationary with respect to all possible deformation mappings which are compatible with the boundary conditions [15].

2.2.1 The Kinetic Energy, (K)

The kinetic energy of the body is a function of the velocity and can be written as,

$$K(\dot{\boldsymbol{x}}) = \int_{V_0} \frac{1}{2} \rho_0 \dot{\boldsymbol{x}}^2 dV_0 \,. \tag{2.3}$$

2.2.2 The Internal Potential Energy (Π_{int})

The internal potential energy depends on the constitutive relations of the materials in the system. In this research hyperelastic Neo-Hookean materials are considered, which undergo large deformations and displacements.

Let $\boldsymbol{F}$ be the deformation gradient tensor which can be written as,

$$\boldsymbol{F}_{ij} = \frac{\partial x_i}{\partial X_j} \qquad \forall\ i, j = 1, .., 3$$

The relevant kinematic quantities associated with the deformation gradient are the right Cauchy-Green tensor, $\boldsymbol{C}$, the Jacobian, J, and the isochoric component of $\boldsymbol{C}$, $\hat{\boldsymbol{C}}$, which are given by,

$$\boldsymbol{C} = \boldsymbol{F}^T\boldsymbol{F}; \qquad J = \det(\boldsymbol{F}); \qquad \hat{\boldsymbol{C}} = J^{-\frac{2}{3}}\boldsymbol{C} \ .$$

For isotropic Neo-Hookean materials, the internal potential energy can be expressed in terms of the Lame constant μ, and the bulk modulus κ as

$$\begin{aligned} \Pi_{\text{int}}(\boldsymbol{x}) &= \int_{V_0} \pi dV_0 \\ &= \int_{V_0} \left[\frac{\mu}{2}\left(tr(\hat{\boldsymbol{C}}) - 3\right) + \frac{1}{2}\kappa(J-1)^2\right] dV_0 \ . \end{aligned} \tag{2.4}$$

The above expression is well suited for compressible or nearly incompressible materials, [72]. A detailed discussion for the treatment of incompressibility will be presented in a later chapter.

The relevant stress measures and their relationship with energy can be expressed as follows [72, 73]:

$$\frac{\partial \pi(\boldsymbol{F})}{\partial \boldsymbol{F}} = \boldsymbol{P} \tag{2.5}$$

where $\boldsymbol{P}$ is the first Piola Kirchhoff (PK1) stress tensor. The PK1 stress and the true Cauchy stress $\boldsymbol{\sigma}$ are related as:

$$\boldsymbol{\sigma} = J^{-1}\,\boldsymbol{P}\,\boldsymbol{F}^T \tag{2.6}$$

The internal energy per unit volume can be split to deviatoric and Volumetric components as follows:

$$\pi(\boldsymbol{F}) = \pi_{\text{dev}}(\boldsymbol{F}) + \pi_{\text{vol}}(\boldsymbol{F}) \tag{2.7}$$

$$\pi_{\text{dev}}(\boldsymbol{F}) = \frac{\mu}{2}\left\{\text{tr}(\hat{\boldsymbol{C}}) - 3\right\} \tag{2.8}$$

$$\pi_{\text{vol}}(\boldsymbol{F}) = \frac{\kappa}{2}(J-1)^2 \tag{2.9}$$

It can be added, that, from equation, 2.7, one could similarly split the PK1 and the Cauchy stresses using the equations, 2.5, 2.6 , as follows:

$$\frac{\partial \pi(\boldsymbol{F})}{\partial \boldsymbol{F}} = \frac{\partial \pi_{\text{dev}}(\boldsymbol{F})}{\partial \boldsymbol{F}} + \frac{\partial \pi_{\text{vol}}(\boldsymbol{F})}{\partial \boldsymbol{F}} \tag{2.10}$$

$$\boldsymbol{P} = \boldsymbol{P}_{\text{dev}} + \boldsymbol{P}_{\text{vol}} \tag{2.11}$$

$$\boldsymbol{\sigma} = \boldsymbol{\sigma}_{\text{dev}} + \boldsymbol{\sigma}_{\text{vol}} \tag{2.12}$$

where the Cauchy volumetric stress, ($\boldsymbol{\sigma}_{\text{vol}}$) is the hydrostatic pressure ($p = \kappa(J-1)$) times the unit matrix ($\boldsymbol{I}$):

$$\boldsymbol{\sigma}_{\text{vol}} = p\, \boldsymbol{I}$$

and the other terms are:

$$\begin{aligned} \boldsymbol{P}_{\text{vol}} &= p\, J\, \boldsymbol{F}^{-T} \\ \boldsymbol{P}_{\text{dev}} &= \mu J^{-\frac{2}{3}} \left[\boldsymbol{F} - \frac{\boldsymbol{F} : \boldsymbol{F}}{3}\, \boldsymbol{F}^{-T} \right] \\ \boldsymbol{\sigma}_{\text{dev}} &= \mu J^{-\frac{5}{3}} \left[\boldsymbol{b} - \frac{\boldsymbol{b} : \boldsymbol{I}}{3}\, \boldsymbol{I} \right] \end{aligned}$$

2.2.3 The External Potential Energy (Π_{ext})

The external potential energy includes the work done by the external body and surface forces.

$$\Pi_{\text{ext}}(\boldsymbol{x}) = -\int_{V_0} \boldsymbol{f}^b \cdot \boldsymbol{x}\, dV_0 - \int_{\partial V_0} \boldsymbol{f}^s \cdot \boldsymbol{x}\, dS_0 \tag{2.13}$$

Here, $\boldsymbol{f}^b$ are the body forces, $\boldsymbol{f}^s$ are the surface forces, and ∂V_0 denotes the section of the boundary, in the reference configuration, where the surface forces are applied.

2.3 Discrete time integration

Consider now a sequence of timesteps $t_{n+1} = t_n + \Delta t,\ n = 0, 1, ..., N$, where for simplicity a constant step size has been taken. The position of the body at each step is defined by a mapping $\mathbf{x}_n = \phi(\mathbf{X}, t_n)$. A variational algorithm is defined by a discrete sum integral,

$$S(\mathbf{x}_0, \mathbf{x}_1, ..., \mathbf{x}_N) \approx \sum_{n=0}^{N-1} L_{n,n+1}(\mathbf{x}_n, \mathbf{x}_{n+1}) \tag{2.14}$$

where the discrete Lagrangian L approximates the integral of the continuum Lagrangian $\mathcal{L}$ over a timestep, that is,

$$L_{n,n+1}(\mathbf{x}_n, \mathbf{x}_{n+1}) \approx \int_{t_n}^{t_{n+1}} \mathcal{L}(\mathbf{x}, \dot{\mathbf{x}})\, dt\ . \tag{2.15}$$

Here, for simplicity, the case in which the Lagrangian is a function of $\mathbf{x}$ and $\dot{\mathbf{x}}$ only, is considered. The variable dependance, like that of pressure, will be considered later. There are a number of ways in which the approximation (2.15) can be chosen, and, each one will lead to a different time integration algorithm.

The stationary conditions of the discrete sum integral S with respect to a variation $\delta\mathbf{v}_n$ of the body position at time step n are now given by,

$$D_n S[\delta\mathbf{v}_n] = D_2 L_{n-1,n}(\mathbf{x}_{n-1}, \mathbf{x}_n)[\delta\mathbf{v}_n] + D_1 L_{n,n+1}(\mathbf{x}_n, \mathbf{x}_{n+1})[\delta\mathbf{v}_n] = 0 \qquad \forall \delta\mathbf{v}_n\ , \tag{2.16}$$

where D_i denotes directional derivative with respect to i-th variable. The above equation represents the statement of equilibrium at step n and will enable the positions at step $n+1$ to be evaluated in terms of positions at $n-1$ and n. It will be shown in the next section that regardless of the actual discrete Lagrangian chosen, the algorithms derived following the above variational procedure will inherit the conservation properties of the continuum system. Moreover, it is also shown in [5] that this type of algorithms are also simplectic.

As a simple example of the above variational integrators, consider first the standard case of the commonly used central difference (or leap-frog) time integrator. This well-known

scheme is arrived at by defining the discrete Lagrangian between two timesteps as,

$$L_{n,n+1}(\mathbf{x}_n, \mathbf{x}_{n+1}) = \frac{\Delta t}{2} M(\mathbf{v}_{n+1/2}, \mathbf{v}_{n+1/2}) - \Delta t\, \Pi(\mathbf{x}_n) \ , \tag{2.17}$$

where the intermediate velocity is defined as $\mathbf{v}_{n+1/2} = (\mathbf{x}_{n+1} - \mathbf{x}_n)/\Delta t$ and the mass bilinear form is given by,

$$M(\mathbf{u}, \mathbf{v}) = \int_{V_0} (\mathbf{u} \cdot \mathbf{v})\, \rho_0\, dV_0 \ . \tag{2.18}$$

Substituting into equation (2.16) for the above discrete Lagrangian expression leads, after some simple algebra, to the standard explicit central difference time integration scheme,

$$M\left(\delta\mathbf{v}_n, \frac{\mathbf{v}_{n+1/2} - \mathbf{v}_{n-1/2}}{\Delta t}\right) = F(\delta\mathbf{v}_n; \mathbf{x}_n) - T(\delta\mathbf{v}_n; \mathbf{x}_n) \ , \tag{2.19}$$

where the external and internal forces are respectively,

$$\begin{aligned} F(\delta\mathbf{v}; \mathbf{x}_n) &= -D\Pi_{\text{ext}}(\mathbf{x}_n)[\delta\mathbf{v}] \ , \\ T(\delta\mathbf{v}; \mathbf{x}_n) &= D\Pi_{\text{int}}(\mathbf{x}_n)[\delta\mathbf{v}] \ . \end{aligned} \tag{2.20}$$

Remark For a uniform step size, identical explicit equations are in fact obtained if the Lagrangian is approximated as,

$$L_{n,n+1}(\mathbf{x}_n, \mathbf{x}_{n+1}) = \frac{\Delta t}{2} M(\mathbf{v}_{n+1/2}, \mathbf{v}_{n+1/2}) - \Delta t\, \Pi(\mathbf{x}_{n+1}) \ , \tag{2.21}$$

or indeed,

$$L_{n,n+1}(\mathbf{x}_n, \mathbf{x}_{n+1}) = \frac{\Delta t}{2} M(\mathbf{v}_{n+1/2}, \mathbf{v}_{n+1/2}) - \frac{\Delta t}{2}\, \Pi(\mathbf{x}_n) - \frac{\Delta t}{2}\, \Pi(\mathbf{x}_{n+1}) \ . \tag{2.22}$$

However, for variable timestep size, only the last equation leads to the standard second order leap-frog scheme.

A different scheme, namely the mid-point rule, can be derived from an incremental

Lagrangian defined as,

$$L_{n,n+1}(\mathbf{x}_n, \mathbf{x}_{n+1}) = \frac{\Delta t}{2} M(\mathbf{v}_{n+1/2}, \mathbf{v}_{n+1/2}) - \Delta t\, \Pi(\mathbf{x}_{n+1/2}); \qquad \mathbf{x}_{n+1/2} = \frac{1}{2}(\mathbf{x}_n + \mathbf{x}_{n+1}) \ . \tag{2.23}$$

Simple algebra shows that the resulting equilibrium equations are,

$$\begin{aligned} M\left(\delta\mathbf{v}_n, \frac{\mathbf{v}_{n+1/2} - \mathbf{v}_{n-1/2}}{\Delta t}\right) &= \frac{1}{2}\left\{F(\delta\mathbf{v}_n; \mathbf{x}_{n+1/2}) + F(\delta\mathbf{v}_n; \mathbf{x}_{n-1/2})\right. \\ &\quad \left. -T(\delta\mathbf{v}_n; \mathbf{x}_{n+1/2}) - T(\delta\mathbf{v}_n; \mathbf{x}_{n-1/2})\right\} \end{aligned} \tag{2.24}$$

This is clearly an implicit scheme. It is well known, however, that for the linear case it is unconditionally stable. Note also that the mid-point rule is more commonly written in a one step for as,

$$M\left(\delta\mathbf{v}_n, \frac{\mathbf{v}_{n+1} - \mathbf{v}_n}{\Delta t}\right) = F(\delta\mathbf{v}_n; \mathbf{x}_{n+\frac{1}{2}}) - T(\delta\mathbf{v}_n; \mathbf{x}_{n+\frac{1}{2}}); \qquad \mathbf{x}_{n+1} = \mathbf{x}_n + \frac{\Delta t}{2}(\mathbf{v}_n + \mathbf{v}_{n+1}) \ . \tag{2.25}$$

Averaging this expression written between n and $n+1$, and $n-1$ and n, it is easy to show that equation (2.24) is recovered.

2.4 Conservation of System Invariants

The conservation properties of the above variational algorithms are a consequence of the invariance of the Lagrangian with respect to rigid body translation and rotations. This is simply a particular case of Noether's Theorem, whereby the symmetries of the Lagrangian lead to preserved quantities throughout the motion [15].

Consider the case of linear momentum first. This easily follows from the translational invariance of the discrete Lagrangian in the absence of external forces. To show this note first that if there are no external forces, then for any arbitrary constant vector $\mathbf{a} \in \mathcal{R}^3$,

$$L_{n,n+1}(\mathbf{x}_n + \mathbf{a}, \mathbf{x}_{n+1} + \mathbf{a}) = L_{n,n+1}(\mathbf{x}_n, \mathbf{x}_{n+1}) \ .$$

Differentiating this expression gives,

$$D_1 L_{n,n+1}(\mathbf{x}_n, \mathbf{x}_{n+1})[\mathbf{a}] + D_2 L_{n,n+1}(\mathbf{x}_n, \mathbf{x}_{n+1})[\mathbf{a}] \;=\; 0\,. \tag{2.26}$$

But from the equilibrium equation (2.16), taking $\delta\mathbf{v}_n = \mathbf{a}$, the following relation is obtained:

$$D_1 L_{n,n+1}(\mathbf{x}_n, \mathbf{x}_{n+1})[\mathbf{a}] \;=\; -D_2 L_{n,n+1}(\mathbf{x}_{n-1}, \mathbf{x}_n)[\mathbf{a}]\,.$$

Substituting into (2.26) gives,

$$D_2 L_{n,n+1}(\mathbf{x}_n, \mathbf{x}_{n+1})[\mathbf{a}] \;=\; D_2 L_{n,n+1}(\mathbf{x}_{n-1}, \mathbf{x}_n)[\mathbf{a}]\,, \tag{2.27}$$

which implies the preservation of the discrete linear momentum, $\mathbf{G}(\mathbf{x}_n, \mathbf{x}_{n+1})$, which is defined as,

$$\mathbf{G}(\mathbf{x}_n, \mathbf{x}_{n+1}) \cdot \mathbf{a} \;=\; D_2 L_{n,n+1}(\mathbf{x}_n, \mathbf{x}_{n+1})[\mathbf{a}] \qquad \forall\, \mathbf{a} \in \mathcal{R}^3\,.$$

The case of angular momentum is similarly obtained from the invariance of the Lagrangian with respect to rotations,

$$L_{n,n+1}(\mathbf{R}\mathbf{x}_n, \mathbf{R}\mathbf{x}_{n+1}) \;=\; L_{n,n+1}(\mathbf{x}_n, \mathbf{x}_{n+1}) \tag{2.28}$$

where $\mathbf{R}$ is an orthogonal rotation matrix. Differentiating this expression now gives,

$$D_1 L_{n,n+1}(\mathbf{x}_n, \mathbf{x}_{n+1})[\mathbf{w} \times \mathbf{x}_n] + D_2 L_{n,n+1}(\mathbf{x}_n, \mathbf{x}_{n+1})[\mathbf{w} \times \mathbf{x}_{n+1}] \;=\; 0 \qquad \forall\, \mathbf{w} \in \mathcal{R}^3 \tag{2.29}$$

where $\mathbf{w}$ represents a small rotation (spin) vector associated with $\mathbf{R}$ which is arbitrary since the choice of $\mathbf{R}$, in (2.28), was also arbitrary. Again from (2.16) for the particular case $\delta\mathbf{v}_n = \mathbf{w} \times \mathbf{x}_n$ the following relation is obtained:

$$D_1 L_{n,n+1}(\mathbf{x}_n, \mathbf{x}_{n+1})[\mathbf{w} \times \mathbf{x}_n] \;=\; -D_2 L_{n,n+1}(\mathbf{x}_{n-1}, \mathbf{x}_n)[\mathbf{w} \times \mathbf{x}_n]\,,$$

and substituting into equation (2.29) gives,

$$D_2L_{n,n+1}(\mathbf{x}_n,\mathbf{x}_{n+1})[\mathbf{w}\times\mathbf{x}_{n+1}] \;=\; D_2L_{n,n+1}(\mathbf{x}_{n-1},\mathbf{x}_n)[\mathbf{w}\times\mathbf{x}_n]\;, \tag{2.30}$$

which leads to the following definition of the discrete angular momentum $\mathbf{H}(\mathbf{x}_n,\mathbf{x}_{n+1})$,

$$\mathbf{H}(\mathbf{x}_n,\mathbf{x}_{n+1})\cdot\mathbf{w} \;=\; D_2L_{n,n+1}(\mathbf{x}_n,\mathbf{x}_{n+1})[\mathbf{w}\times\mathbf{x}_{n+1}]\;. \tag{2.31}$$

Note that in order to define the discrete linear and angular momentum, only the dependence of the Lagrangian on the geometry is relevant. In particular, when the Lagrangian depends explicitly on geometry and the pressure, as in the next section, the above definitions and derivations remain unaffected.

2.4.1 A simple example: System of Particles

As an illustration of the conservation laws derived above, consider the simple case of a system of particles with masses m^a for $a = 1,..,M$ as shown in figure 2-2. The configuration at

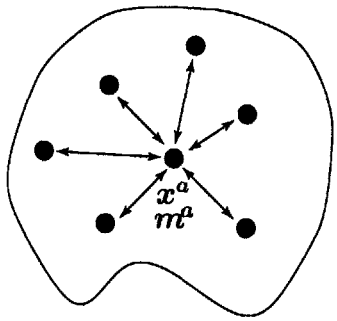

Figure 2-2: A system of particles

time t_n is given by a vector $\mathbf{x}_n \in R^{3M}$ and $\mathbf{x}_n^T = [\mathbf{x}_n^1,\ldots,\mathbf{x}_n^a,\ldots]$. Consider the discrete Lagrangian,

$$L_{n,n+1}(\mathbf{x}_n,\mathbf{x}_{n+1}) \;=\; \sum_{a=1}^{M}\frac{\Delta t}{2}\,m^a\,\mathbf{v}^a_{n+1/2}\cdot\mathbf{v}^a_{n+1/2} - \Delta t\,\Pi(\mathbf{x}_n)\;, \tag{2.32}$$

where Π represents some internal potential leading to particle interaction forces (which is typically only a function of particle distances) and $\mathbf{v}^a_{n+1/2} = (\mathbf{x}^a_{n+1} - \mathbf{x}^a_n)/\Delta t$. Both linear

and angular momentum emerge from,

$$D_2 L(\mathbf{x}_n, \mathbf{x}_{n+1})[\delta \mathbf{v}_{n+1}] \;=\; \sum_a m^a \, \mathbf{v}^a_{n+1/2} \cdot \delta \mathbf{v}^a_{n+1} \; . \tag{2.33}$$

For instance, taking $\delta \mathbf{v}^a_{n+1} = \mathbf{a}$, the standard definition of the linear momentum is recovered,

$$\mathbf{G}(\mathbf{x}_n, \mathbf{x}_{n+1}) \;=\; \sum_{a=1}^{M} m^a \, \mathbf{v}^a_{n+1/2} \; . \tag{2.34}$$

Taking $\delta \mathbf{v}^a_{n+1} = \mathbf{w} \times \mathbf{x}^a_{n+1}$ gives, after some trivial algebra, the angular momentum as

$$\mathbf{H}(\mathbf{x}_n, \mathbf{x}_{n+1}) \;=\; \sum_{a=1}^{M} m^a \, \mathbf{x}^a_{n+1} \times \mathbf{v}^a_{n+1/2} \; . \tag{2.35}$$

The conservation property shown above, remains valid as long as the internal Potential Energy $\Pi(\boldsymbol{x}_n)$ depends only on $\boldsymbol{x}_n$.

2.5 Space-Time Discretization

Variational algorithms require a definition of a discrete action integral, which requires the computation of the Lagrangian Integral between time steps t_n and t_{n+1}. To compute the integral, a discrete space-time domain needs to be studied. In this section a brief description of space-time discretization is presented. Computation of the Lagrangian Integral within generic space-time volumes is explained by the example of triangular meshes.

In case of explicit schemes, the Potential Integral (Π) is computed based on the variables lying at time level t_n. The Kinetic Energy Integral (K) depends on variables at both time levels t_n and t_{n+1}. To begin with, the computation of the Kinetic Energy Integral in a single triangular element is described.

Figure 2-3, shows the typical space-time volume of a single triangle. The triangle abc_n and triangle abc_{n+1} enclose a prismatic space-time volume. This volume is further subdivided into three tetrahedra. The task is to compute the kinetic energy integral K within each of the space-time-tetrahedra, and then sum each of the contributions to compute the net integral within the space-time-prism. To do so, a generic space-time-tetrahedron(Fig.

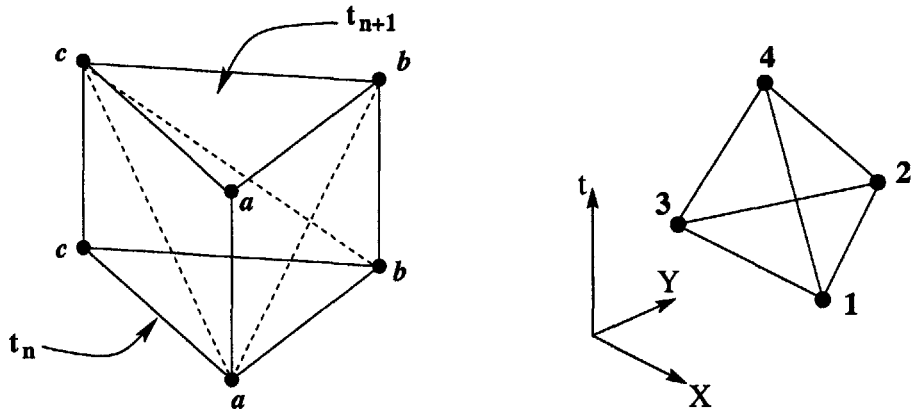

Figure 2-3: The space-time-prism (left) and a generic space-time-tetrahedron (right).

2-3, (right)) is studied and the integral is computed as follows:

$$\boldsymbol{x} = \boldsymbol{x}(\boldsymbol{X}, t) \qquad \boldsymbol{v}_{n,n+1} = \frac{\mathrm{d}\boldsymbol{x}}{\mathrm{d}t} \tag{2.36}$$

Where $\boldsymbol{x}$ is the position vector, $\boldsymbol{X}$ is the reference position vector and $\frac{\mathrm{d}}{\mathrm{d}t}$ is the total derivative. Note here, that for the Kinetic Energy Integral, total derivatives of position vectors, are considered. In the general case, any quantity (scalar or vector) would have a similar treatment. First, a set of volume coordinates are introduced, analogous to the area coordinates in case of triangles. The volume coordinates, given by $(\xi_1, \xi_2, \xi_3, \xi_4)$ attain values of 1 at their corresponding nodes and zero at other nodes, *ie.*, ξ_i is one at node i and zero at all nodes $j \neq i$. Any function *linear* in X, Y, t, say $F(X, Y, t)$, can be interpolated within the tetrahedron, based on its nodal values F_a and shape functions $N_a = \xi_a$ as $F(X, Y, t) = F_a \xi_a$. The coordinate transform between (X, Y, t) and $(\xi_1, \xi_2, \xi_3, \xi_4)$ can be written as:

$$\begin{bmatrix} 1 \\ X \\ Y \\ t \end{bmatrix} = \begin{bmatrix} 1 & 1 & 1 & 1 \\ X_1 & X_2 & X_3 & X_4 \\ Y_1 & Y_2 & Y_3 & Y_4 \\ t_1 & t_2 & t_3 & t_4 \end{bmatrix} \begin{bmatrix} \xi_1 \\ \xi_2 \\ \xi_3 \\ \xi_4 \end{bmatrix} \tag{2.37}$$

Inverting this relation gives:

$$\begin{bmatrix} \xi_1 \\ \xi_2 \\ \xi_3 \\ \xi_4 \end{bmatrix} = \frac{1}{6\mathcal{V}_0} \begin{bmatrix} 6\mathcal{V}_1 & a_1 & b_1 & c_1 \\ 6\mathcal{V}_2 & a_2 & b_2 & c_2 \\ 6\mathcal{V}_3 & a_3 & b_3 & c_3 \\ 6\mathcal{V}_4 & a_4 & b_4 & c_4 \end{bmatrix} \begin{bmatrix} 1 \\ X \\ Y \\ t \end{bmatrix} \tag{2.38}$$

where a_i's are the cofactor of the X_i elements in the transformation matrix. Similarly b_i's are the cofactors of the Y_i elements, c_i's are the cofactors of the t_i elements, and $\mathcal{V}_i$'s are one sixth the cofactor of each unit element in the transformation matrix. $\mathcal{V}_0$ is the volume of the tetrahedron given by:

$$\mathcal{V}_0 = \frac{1}{6} \begin{vmatrix} 1 & 1 & 1 & 1 \\ X_1 & X_2 & X_3 & X_4 \\ Y_1 & Y_2 & Y_3 & Y_4 \\ t_1 & t_2 & t_3 & t_4 \end{vmatrix} \tag{2.39}$$

The derivatives of the function now can be written as, using chain rule:

$$\frac{dF}{d\boldsymbol{X}^i} = \frac{\partial F}{\partial \xi^j} \frac{d\xi^j}{d\boldsymbol{X}^i} \tag{2.40}$$

where $\boldsymbol{X} = [1\ X\ Y\ t]^T$. Thus, for the time gradients we can say:

$$\frac{dF}{dt} = \frac{1}{6\mathcal{V}_0} \frac{\partial F}{\partial \xi_j} c_j \tag{2.41}$$

Now, since F is linearly interpolated, $\left(\frac{\partial F}{\partial \xi_i} = F_i\right)$ which leads to a simple relation for the

derivatives:

$$\frac{dF}{dt} = \frac{\begin{vmatrix} 1 & 1 & 1 & 1 \\ X_1 & X_2 & X_3 & X_4 \\ Y_1 & Y_2 & Y_3 & Y_4 \\ F_1 & F_2 & F_3 & F_4 \end{vmatrix}}{\begin{vmatrix} 1 & 1 & 1 & 1 \\ X_1 & X_2 & X_3 & X_4 \\ Y_1 & Y_2 & Y_3 & Y_4 \\ t_1 & t_2 & t_3 & t_4 \end{vmatrix}} \tag{2.42}$$

Similarly, assuming a linear interpolation of $\boldsymbol{x}$ in space and time, the velocity within the tetrahedron is obtained as a ratio of two determinants:

$$\boldsymbol{v}_{n,n+1} = \frac{\begin{vmatrix} 1 & 1 & 1 & 1 \\ X_1 & X_2 & X_3 & X_4 \\ Y_1 & Y_2 & Y_3 & Y_4 \\ \boldsymbol{x}_1 & \boldsymbol{x}_2 & \boldsymbol{x}_3 & \boldsymbol{x}_4 \end{vmatrix}}{\begin{vmatrix} 1 & 1 & 1 & 1 \\ X_1 & X_2 & X_3 & X_4 \\ Y_1 & Y_2 & Y_3 & Y_4 \\ t_1 & t_2 & t_3 & t_4 \end{vmatrix}} \tag{2.43}$$

Note here, that in the special case where two nodes of a given space-time-tetrahedron have the same reference coordinate (implying the same point) then, the velocity in the tetrahedron simply becomes (in this case assuming $X_1 = X_4$ and $Y_1 = Y_4$):

$$\boldsymbol{v}_{n,n+1} = \frac{\boldsymbol{x}_4 - \boldsymbol{x}_1}{t_4 - t_1} \tag{2.44}$$

This simplification leads to a criteria for the choice of subdivision of any generic space-time volume. One should choose to sub-divide a given space-time volume into as many tetrahedra with common nodes as possible. This would lead to a simple velocity interpolation within

the tetrahedron. Now the Kinetic Energy Integral K is computed within the space-time-tetrahedron:

$$K_{n,n+1} = \int_{\mathcal{V}_0} \frac{1}{2}\rho_0 \left(\boldsymbol{v}_{n,n+1} \cdot \boldsymbol{v}_{n,n+1}\right) d\mathcal{V}_0 \tag{2.45}$$

In the case of a tetrahedron with common nodes this volume, simply becomes:

$$\mathcal{V}_0 = \frac{A_{123}}{3}(t_4 - t_1) \tag{2.46}$$

where A_{123} is the area of the triangle with nodes 1,2 and 3.

$$A_{123} = \frac{1}{2}\begin{vmatrix} 1 & 1 & 1 \\ X_1 & X_2 & X_3 \\ Y_1 & Y_2 & Y_3 \end{vmatrix}$$

In the generic case the Kinetic Energy Integral $K_{n,n+1}$ would take the form:

$$K_{n,n+1} = \mathcal{V}_0 \frac{1}{2}\rho_0 \left(\boldsymbol{v}_{n,n+1} \cdot \boldsymbol{v}_{n,n+1}\right) \tag{2.47}$$

But in the case of a tetrahedron with common nodes, the Kinetic Energy Integral $K_{n,n+1}$ would take the simple form ($m_{123} = \rho_0 A_{123}$):

$$K_{n,n+1} = (t_4 - t_1)\frac{m_{123}}{3}\frac{1}{2}\left(\boldsymbol{v}_{n,n+1} \cdot \boldsymbol{v}_{n,n+1}\right) \tag{2.48}$$

Now, revisiting the space-time-prism of the triangle (Fig. 2-3) it is observed, that it is subdivided into three tetrahedra, each one of them have a common node. Hence, using the above simplified relations, a very simple form of the Kinetic Energy Integral is obtained:

$$K_{n,n+1}^{\text{prism}} = \frac{m_{abc}}{3}\frac{\Delta t}{2}\left[\left(\boldsymbol{v}^a_{n+1/2} \cdot \boldsymbol{v}^a_{n+1/2}\right) + \left(\boldsymbol{v}^b_{n+1/2} \cdot \boldsymbol{v}^b_{n+1/2}\right) + \left(\boldsymbol{v}^c_{n+1/2} \cdot \boldsymbol{v}^c_{n+1/2}\right)\right] \tag{2.49}$$

Where m_{abc} is the mass of the triangle abc and:

$$\begin{aligned} \Delta t &= t_{n+1} - t_n \\ \boldsymbol{v}^i_{n+1/2} &= \frac{\boldsymbol{x}_{n+1} - \boldsymbol{x}_n}{\Delta t} \qquad \forall i = a, b, c \end{aligned}$$

In case of a finite element mesh, the space-time volume of the entire mesh can be subdivided into space-time-prisms corresponding to each element. Hence, the net Kinetic Energy Integral obtained for the whole mesh would be:

$$K_{n,n+1} = \sum_a \frac{\Delta t}{2} M^a \, \boldsymbol{v}^a_{n+1/2} \cdot \boldsymbol{v}^a_{n+1/2} \tag{2.50}$$

Where M^a is the lumped mass of each node(a) in the mesh. Similarly, the Potential Energy Integral can be calculated as:

$$\Pi_n = \sum_e \pi^e_n A_e \tag{2.51}$$

Where π^e_n is the potential energy per unit area in a given triangle. Thus, the net Lagrangian of the entire mesh would be:

$$\begin{aligned} L_{n,n+1} &= K_{n,n+1} - \Delta t \, \Pi_n \\ &= \sum_a \frac{\Delta t}{2} M^a \, \boldsymbol{v}^a_{n+1/2} \cdot \boldsymbol{v}^a_{n+1/2} \quad - \quad \Delta t \sum_e \pi^e_n A^n_e \end{aligned} \tag{2.52}$$

This leads to the discrete Lagrangian Integral of the Leap Frog method, as discussed in section 2.3.

Hence, it is shown that the Leap Frog scheme, with lumped mass, can be interpreted as an outcome of linear interpolations in space-time. In this section some generic space-time discretization principles have been presented and used to develop the standard Leap Frog time-marching scheme. The objective was to present the generic treatment of space-time discretizations, which could be used in the further development of time-integration algorithms.

2.6 Standard finite element formulation

In the previous section, the discrete Kinetic Energy integral was obtained using a space-time discretization. In this section, the variational formulation is studied along with spatial discretization. A spatial discretization using linear elements (triangles in 2D and tetrahedra in 3D) will be discussed. Based upon linear interpolation, the position vector $\boldsymbol{x}_e^n$ in an element e, can be written as:

$$\boldsymbol{x}_e^n = N_a^e \boldsymbol{x}_a^n \tag{2.53}$$

where N_a^e are linear shape functions within an element e. The action integral as discretized in time in equation 2.14 now can be rewritten as:

$$\begin{aligned} S &= S(\boldsymbol{x}_a^n; a = 1, \ldots, N^d; n = 1, \ldots, N) \\ &\approx \sum_{n=0}^{N} L_{n,n+1}(\boldsymbol{x}_a^n, \boldsymbol{x}_a^{n+1};\ a = 1, \ldots, N^d) \end{aligned} \tag{2.54}$$

where N^d are the number of nodes and N are the number of time steps. For the Leap Frog Method, the Lagrangian within the time steps n and $n+1$ can be written as:

$$L_{n,n+1}(\boldsymbol{x}_a^n, \boldsymbol{x}_a^{n+1}) = K_{n,n+1}(\boldsymbol{x}_a^n, \boldsymbol{x}_a^{n+1}) - \Delta t \left(\Pi_n^{\text{ext}}(\boldsymbol{x}_a^n) + \Pi_n^{\text{int}}(\boldsymbol{x}_a^n)\right) \tag{2.55}$$

The stationarity condition then becomes:

$$\frac{\partial S}{\partial \boldsymbol{x}_a^n} = \frac{\partial L_{n,n+1}}{\partial \boldsymbol{x}_a^n} + \frac{\partial L_{n-1,n}}{\partial \boldsymbol{x}_a^n} = 0 \tag{2.56}$$

which leads to the relations between the derivatives of the Kinetic and Potential integrals as:

$$\frac{\partial K_{n,n+1}}{\partial \boldsymbol{x}_a^n} - \Delta t \frac{\partial \Pi_n^{\text{ext}}}{\partial \boldsymbol{x}_a^n} - \Delta t \frac{\partial \Pi_n^{\text{int}}}{\partial \boldsymbol{x}_a^n} + \frac{\partial K_{n-1,n}}{\partial \boldsymbol{x}_a^n} = 0 \tag{2.57}$$

Now, the internal Potential Energy and its derivative with respect to $\boldsymbol{x}_a^n$ are studied. The Potential Energy is a function of $\boldsymbol{x}_a$ at time level n. For convenience, the time index n is

dropped for the rest of this section, therefore, $\boldsymbol{x}_a$ implies $\boldsymbol{x}_a^n$ unless mentioned otherwise. In addition, the following index notation is used. Indices e, f are used to denote elements, a, b are used to denote nodes, i, j, k, l are used to denote vector directions in the current (spatial) configuration and I, J, K, L are used to denote the directions of vectors in the reference (material) configuration. First, the deformation gradient within the element e, is considered:

$$\boldsymbol{F}^e = \frac{\partial \boldsymbol{x}}{\partial \boldsymbol{X}} = \boldsymbol{x}_a^e \otimes \frac{\partial N_a^e}{\partial \boldsymbol{X}} \tag{2.58}$$

where $\boldsymbol{X}$ is the position vector of the reference configuration. Note that since the shape functions are linear in the element the gradients are constant within an element hence the the deformation gradient is a constant within the element. Based on the Neo-Hookean model, the potential energy can be written as:

$$\Pi_{\text{int}}(\boldsymbol{x}) = \sum_e \int_{V_e^0} \pi^e(\boldsymbol{F}^e)\, dV_e^0 \tag{2.59}$$

$$\pi^e(\boldsymbol{F}^e) = \pi^e_{\text{dev}}(\boldsymbol{F}^e) + \pi^e_{\text{vol}}(\boldsymbol{F}^e) \tag{2.60}$$

$$\pi^e_{\text{dev}}(\boldsymbol{F}^e) = \frac{\mu}{2}\left\{\text{tr}(\hat{\boldsymbol{C}}_e) - 3\right\} \tag{2.61}$$

$$\pi^e_{\text{vol}}(\boldsymbol{F}^e) = \frac{\kappa}{2}(J_e - 1)^2 \tag{2.62}$$

where

$$J_e = \det(\boldsymbol{F}^e); \quad \boldsymbol{C}_e = \boldsymbol{F}^{eT}\boldsymbol{F}^e; \quad \boldsymbol{b}_e = \boldsymbol{F}^e\boldsymbol{F}^{eT}; \quad \hat{\boldsymbol{C}}_e = J_e^{-\frac{2}{3}}\boldsymbol{C}_e;$$

Therefore, the derivative of potential energy *wrt.* $\boldsymbol{x}$ can be written as (using Eqn. 2.5) :

$$\frac{\partial \pi(\boldsymbol{F})}{\partial x_i} = \frac{\partial \pi(\boldsymbol{F})}{\partial \boldsymbol{F}} : \frac{\partial \boldsymbol{F}}{\partial x_i} \tag{2.63}$$

$$= \boldsymbol{P} : \frac{\partial \boldsymbol{F}}{\partial x_i} \tag{2.64}$$

Further simplifying this in indicial notation, it leads to:

$$\frac{\partial \pi}{\partial x_i^a} = P_{kL} \frac{\partial F_{kL}}{\partial x_i^a} \tag{2.65}$$

$$= P_{kL} \frac{\partial N_a^e}{\partial X_L} \delta_{ik} \tag{2.66}$$

$$= P_{iL} \frac{\partial N_a^e}{\partial X_L} \tag{2.67}$$

$$= P_{iL} \frac{\partial N_a^e}{\partial x_j} F_{jL}^e \tag{2.68}$$

Now, introducing a global index of a node as, b, such that it is the a'th node of element e, (from connectivity) and revisiting equation, 2.59, one can express the derivative of the Potential as:

$$\frac{\partial \Pi_{\text{int}}(\boldsymbol{x})}{\partial x_i^b} = \sum_{(e,a)\in b} \int_{V_e^0} \frac{\partial \pi^e(\boldsymbol{F}^e)}{\partial x_i^a} dV_e^0 \tag{2.69}$$

$$= \sum_{(e,a)\in b} \int_{V_e^0} P_{iL} \frac{\partial N_a^e}{\partial x_j} F_{jL}^e \, dV_e^0 \tag{2.70}$$

Now, changing the reference volume V^0 to V a current volume one can obtain:

$$\frac{\partial \Pi_{\text{int}}(\boldsymbol{x})}{\partial x_i^b} = \sum_{(e,a)\in b} \int_{V_e} P_{iL} \frac{\partial N_a^e}{\partial x_j} F_{jL}^e \, J_e^{-1} dV_e \tag{2.71}$$

Inserting equation 2.6 into equation 2.71, one can obtain:

$$\frac{\partial \Pi_{\text{int}}(\boldsymbol{x})}{\partial x_i^b} = \sum_{(e,a)\in b} \int_{V_e} \frac{\partial N_a^e}{\partial x_j} \sigma_{ij}^e dV_e$$

$$= T_i^b = \sum_{(e,a)\in b} T_{ai}^e \tag{2.72}$$

where T_i^b are the internal tractions at node b along direction i, and the T_{ai}^e are the elemental internal tractions at a'th node of the element along direction i. Hence, it is shown that the internal tractions, based on standard finite element, can be obtained, from the derivative of the potential energy *wrt.* $\boldsymbol{x}$. Similar to the internal Potential Energy, it can be shown that

the external Potential Energy (2.13) would have similar derivatives:

$$\begin{aligned}\frac{\partial \Pi_{\text{ext}}(\boldsymbol{x})}{\partial x_i^b} &= -\sum_{(e,a)\in b}\int_{V_e^0}\rho_0 N_a^e\, f_i^b dV_e^0 - \sum_{(e,a)\in b}\int_{\partial V_e} N_a^e\, f_i^s dS_e \\ &= -F_i^b = -\sum_{(e,a)\in b} F_{ai}^e \end{aligned} \tag{2.73}$$

where f_i^s are external surface force per unit area, and f_i^b are the body forces per unit mass. Further, from the Kinetic Energy integral obtained in the previous section, one could derive expressions for its derivates:

$$\begin{aligned} K_{n,n+1}(\boldsymbol{x}_n, \boldsymbol{x}_{n+1}) &= \sum_a \frac{\Delta t}{2} M^a \boldsymbol{v}_{n+1/2}^a \cdot \boldsymbol{v}_{n+1/2}^a \\ v_{n+1/2}^{a_i} &= \frac{1}{\Delta t}\left(x_{n+1}^{a_i} - x_n^{a_i}\right) \\ \frac{\partial K_{n,n+1}}{\partial x_{b_i}^n} &= -M^b v_{n+1/2}^{b_i} \end{aligned} \tag{2.74}$$

$$\begin{aligned} K_{n-1,n}(\boldsymbol{x}_{n-1}, \boldsymbol{x}_n) &= \sum_a \frac{\Delta t}{2} M^a \boldsymbol{v}_{n-1/2}^a \cdot \boldsymbol{v}_{n-1/2}^a \\ v_{n-1/2}^{a_i} &= \frac{1}{\Delta t}\left(x_n^{a_i} - x_{n-1}^{a_i}\right) \\ \frac{\partial K_{n-1,n}}{\partial x_{b_i}^n} &= M^b v_{n-1/2}^{b_i} \end{aligned} \tag{2.75}$$

Using equation 2.57, we obtain the final discrete equation of motion as:

$$\begin{aligned} \frac{\partial K_{n,n+1}}{\partial x_{b_i}^n} - \Delta t\frac{\partial \Pi_n^{\text{ext}}}{\partial x_{b_i}^n} - \Delta t\frac{\partial \Pi_n^{\text{int}}}{\partial x_{b_i}^n} + \frac{\partial K_{n-1,n}}{\partial x_{b_i}^n} &= M^b\left(-v_{n+1/2}^{b_i} + v_{n-1/2}^{b_i}\right) - \Delta t\left(T_n^{b_i} - F_n^{b_i}\right) = 0 \\ M^b\left(v_{n+1/2}^{b_i} - v_{n-1/2}^{b_i}\right) &= \Delta t\left(F_n^{b_i} - T_n^{b_i}\right) \end{aligned}$$

which can be written in the vector form:

$$M^b\left(\boldsymbol{v}_{n+1/2}^b - \boldsymbol{v}_{n-1/2}^b\right) = \Delta t\left(\boldsymbol{F}_n^b - \boldsymbol{T}_n^b\right) \tag{2.76}$$

Thus, we obtain the time marching algorithm with the Central Difference Scheme, using the spatial discretization of the standard linear element. The standard linear element described above is commonly found in literature [74]. It was shown here that the standard

element formulation is derived from a variational framework. This formulation performs well, but it is known to be very stiff near incompressibility (volumetric locking), especially for beam bending problems. A nodal element formulation has been developed [69], where the deformation gradient tensor $\boldsymbol{F}$ is averaged at the nodes. This formulation is very well suited for large strain explicit dynamic problems as it does not lock near incompressibility. In the next section, the details of the averaged nodal element formulation are presented. In addition, it will also be shown that the nodal element formulation is derived from a variational formulation.

2.7 Averaged nodal element formulation

In this formulation, the interpolation of the position vectors is similar to the standard element, but the deformation gradient tensor $\boldsymbol{F}$ is averaged at the nodes in the following manner:

$$\boldsymbol{F}^a = \frac{\sum_{e \in a} \boldsymbol{F}^e V_e^0}{\sum_{e \in a} V_e^0} \tag{2.77}$$

Similarly, the volumes are also averaged at the nodes:

$$V_0^a = \sum_{e \in a} \frac{V_e^0}{\eta} \tag{2.78}$$

$$V^a = \sum_{e \in a} \frac{V_e}{\eta} \tag{2.79}$$

where η is 3 for triangles and 4 for tetrahedra. The Jacobian at the nodes are then computed by:

$$J^a = \frac{V^a}{V_0^a} \tag{2.80}$$

Now, the total internal Potential energy, for the averaged nodal element, can be written as:

$$\bar{\Pi}(\boldsymbol{x}) = \sum_a \left(\pi^a_{\text{dev}}(\boldsymbol{F}^a) + \pi^a_{\text{vol}}(J^a)\right) V^0_a \tag{2.81}$$

$$\pi^a_{\text{dev}}(\boldsymbol{F}^a) = \frac{\mu}{2}\left\{\text{tr}(\hat{\boldsymbol{C}}_a) - 3\right\} \tag{2.82}$$

$$\pi^a_{\text{vol}}(J^a) = \frac{\kappa}{2}(J_a - 1)^2 \tag{2.83}$$

where,

$$\boldsymbol{C}_a = \boldsymbol{F}^{aT}\boldsymbol{F}^a;\ \ \boldsymbol{b}_a = \boldsymbol{F}^a\boldsymbol{F}^{aT};\ \ \hat{\boldsymbol{C}}_a = \det(\boldsymbol{C}_a)^{-\frac{1}{3}}\boldsymbol{C}_a;$$

Differentiating the total internal potential *wrt.* a position vector at node b in the direction k, (x^b_k), one can obtain:

$$\frac{\partial \Pi}{\partial x^b_k} = \sum_a \left(\frac{\partial \pi_{\text{dev}}(\boldsymbol{F}^a)}{\partial x^b_k} + \frac{\partial \pi_{\text{vol}}(J^a)}{\partial x^b_k}\right) V^0_a \tag{2.84}$$

$$\frac{\partial \pi_{\text{dev}}(\boldsymbol{F}^a)}{\partial x^b_k} = \frac{\partial \pi_{\text{dev}}(\boldsymbol{F}^a)}{\partial \boldsymbol{F}^a} : \frac{\partial \boldsymbol{F}^a}{\partial x^b_k}$$

$$= \boldsymbol{P}^a_{\text{dev}} : \frac{\partial \boldsymbol{F}^a}{\partial x^b_k} \tag{2.85}$$

$$\frac{\partial \pi_{\text{vol}}(J^a)}{\partial x^b_k} = \frac{\partial \pi_{\text{dev}}(J^a)}{\partial J^a}\frac{\partial J^a}{\partial x^b_k}$$

$$= p^a \frac{\partial J^a}{\partial x^b_k} \tag{2.86}$$

Now, rewriting the expressions for $\boldsymbol{F}^a$ and J^a in equations 2.77 and 2.80, in the following manner:

$$\boldsymbol{F}^a = \frac{1}{V^0_a}\sum_{e\in a}\int_{V^0_e} \boldsymbol{F}^e N^e_a dV^0_e \tag{2.87}$$

$$J^a = \frac{1}{V^0_a}\sum_{e\in a}\int_{V^0_e} J^e N^e_a dV^0_e \tag{2.88}$$

Now, differentiating F^a_{iJ}, *wrt.* x^b_k we get:

$$\begin{aligned}
\frac{\partial F^a_{iJ}}{\partial x^b_k} &= \frac{1}{V^0_a}\sum_{e\in a}\int_{V^0_e}\frac{\partial F^e_{iJ}}{\partial x^b_k}\,N^e_a dV^0_e \\
&= \frac{1}{V^0_a}\sum_{e\in a}\int_{V^0_e}\frac{\partial N^e_b}{\partial X_J}\,\delta_{ik}\,N^e_a dV^0_e \\
&= \frac{1}{V^0_a}\sum_{e\in a}\int_{V^0_e}\frac{\partial N^e_b}{\partial x_j}\,F^e_{jJ}\,\delta_{ik}\,N^e_a\,dV^0_e
\end{aligned} \tag{2.89}$$

which leads to:

$$\frac{\partial \pi_{\text{dev}}(\boldsymbol{F}^a)}{\partial x^b_k} = \frac{P^a_{iJ}}{V^0_a}\sum_{e\in a}\int_{V^0_e}\frac{\partial N^e_b}{\partial x_j}F^e_{jJ}\delta_{ik}N^e_a dV^0_e \tag{2.90}$$

Similarly, for the volumetric parts, one can write as:

$$\begin{aligned}
\frac{\partial J^a}{\partial x^b_k} &= \frac{1}{V^0_a}\sum_{e\in a}\int_{V^0_e}\frac{\partial J^e}{\partial x^b_k}N^e_a dV^0_e \\
&= \frac{1}{V^0_a}\sum_{e\in a}\int_{V^0_e}\frac{\partial J^e}{\partial F^e_{iJ}}\,\frac{\partial F^e_{iJ}}{\partial x^b_k}\,N^e_a\,dV^0_e \\
&= \frac{1}{V^0_a}\sum_{e\in a}\int_{V^0_e}J^e\,F^{e\,-1}_{Ji}\,\frac{\partial N^e_b}{\partial X_J}\delta_{ik}\,N^e_a\,dV^0_e \\
&= \frac{1}{V^0_a}\sum_{e\in a}\int_{V^0_e}J^e\,F^{e\,-1}_{Jk}\,\frac{\partial N^e_b}{\partial x_j}F^e_{jJ}\,N^e_a\,dV^0_e \\
&= \frac{1}{V^0_a}\sum_{e\in a}\int_{V_e}\frac{\partial N^e_b}{\partial x_j}\,\delta_{kj}\,N^e_a\,dV_e
\end{aligned} \tag{2.91}$$

which leads to:

$$\frac{\partial \pi_{\text{vol}}(J^a)}{\partial x^b_k} = \frac{p^a}{V^0_a}\sum_{e\in a}\int_{V_e}\frac{\partial N^e_b}{\partial x_k}\,N^e_a\,dV_e \tag{2.92}$$

Now, substituting 2.90 and 2.92 in 2.84 one can obtain:

$$\begin{aligned}
\frac{\partial \Pi}{\partial x^b_k} &= \sum_a\left(\frac{P^a_{\text{dev}_{iJ}}}{V^0_a}\sum_{e\in a}\int_{V^0_e}\frac{\partial N^e_b}{\partial x_j}F^e_{jJ}\delta_{ik}N^e_a J^{e-1}dV_e \;+\; \frac{p^a}{V^0_a}\sum_{e\in a}\int_{V_e}\frac{\partial N^e_b}{\partial x_j}\,\delta_{kj}\,N^e_a\,dV_e\right)V^0_a \\
&= \sum_{e\in a}\left[\int_{V_e}\frac{\partial N^e_b}{\partial x_j}\left\{J^{e-1}\left(\sum_{a\in e}P^a_{\text{dev}_{kJ}}N^e_a\right)F^e_{jJ} + \left(\sum_{a\in e}p^a N^e_a\right)\delta_{kj}\right\}dV_e\right]
\end{aligned} \tag{2.93}$$

The final relation can be simply stated as:

$$\frac{\partial \Pi}{\partial \boldsymbol{x}^b} = \sum_{(e,a)\in b} \int_{V_e} \bar{\boldsymbol{\sigma}}^e \frac{\partial N_a^e}{\partial \boldsymbol{x}} dV_e \tag{2.94}$$

$$= \boldsymbol{T}_b = \sum_{(e,a)\in b} \boldsymbol{T}_a^e \tag{2.95}$$

$$\tag{2.96}$$

where $\boldsymbol{T}_b$ are the global internal tractions at node b, and the $\boldsymbol{T}_a^e$ are the internal elemental tractions at element e, and node a, such that the a'th node of element e is the global node b. Thus, the average nodal element is derived from a variational formulation. The standard stresses ($\boldsymbol{\sigma}^e$) (as mentioned in the previous section) and the average stress ($\bar{\boldsymbol{\sigma}}^e$) (mentioned above) in an element can be obtained as:

$$J_e = \det(\boldsymbol{F}^e)$$

$$p^e = \kappa(J_e - 1)$$

$$\boldsymbol{P}^e_{\text{dev}} = \mu J_e^{-\frac{2}{3}} \left[\boldsymbol{F}^e - \frac{\boldsymbol{F}^e : \boldsymbol{F}^e}{3} \boldsymbol{F}^{e-T} \right]$$

$$\boldsymbol{\sigma}^e = J_e^{-1} \boldsymbol{P}^e_{\text{dev}} \boldsymbol{F}_e^T + p_e \boldsymbol{I} \tag{2.97}$$

$$\bar{\boldsymbol{\sigma}}^e = J_e^{-1} \bar{\boldsymbol{P}}^e_{\text{dev}} \boldsymbol{F}_e^T + \bar{p}_e \boldsymbol{I} \tag{2.98}$$

$$\bar{\boldsymbol{P}}^e_{\text{dev}} = \sum_{a\in e} \frac{\boldsymbol{P}^a_{\text{dev}}(\boldsymbol{F}^a)}{\eta} \tag{2.99}$$

$$\bar{p}^e = \sum_{a\in e} \frac{p^a(J^a)}{\eta} \tag{2.100}$$

where η is 3 for triangles and 4 for tetrahedra.

This formulation has been studied in [68, 69] and has been found to resolve the drawback (excess stiff behaviour) of the standard element in case of near incompressible beam bending type of problems. But in some cases [75], this develops some non-physical low-energy modes. To stabilize this element a stabilized element, used in this research, is presented.

2.8 Stabilized element

2.8.1 Stiffness stabilization

A stiffness stabilization using the finite element formulations in the previous sections has been developed which addresses the problems encountered by the standard and average nodal elements. In the previous sections, it has been shown that both formulations, are variationally consistent. Hence, it can be shown that a linear combination of the two element formulations would also be variationally consistent. A stabilized internal potential energy comprising of linear combinations of standard and averaged nodal element can be written as:

$$\Pi^{\text{kstab}} = \bar{\Pi}_{\text{dev}} + \alpha_{\text{dev}}(\Pi_{\text{dev}} - \bar{\Pi}_{\text{dev}}) + \bar{\Pi}_{\text{vol}} + \alpha_{\text{vol}}(\Pi_{\text{vol}} - \bar{\Pi}_{\text{vol}}) \tag{2.101}$$

where the $\bar{(\,)}$ quantities represent the average nodal stresses, and α terms are scalar parameters ranging from 0 to 1. Here $\alpha = 0$ leads to the averaged nodal element, and $\alpha = 1$ gives the standard element formulation. From equation 2.97, 2.98 and 2.101 a stiffness stabilized elemental stress can be calculated as follows:

$$\boldsymbol{\sigma}^{\text{kstab}} = \bar{\boldsymbol{\sigma}}_{\text{dev}} + \alpha_{\text{dev}}\,(\boldsymbol{\sigma}_{\text{dev}} - \bar{\boldsymbol{\sigma}}_{\text{dev}}) + \bar{p}\,\boldsymbol{I} + \alpha_{\text{vol}}\,(p - \bar{p})\,\boldsymbol{I} \tag{2.102}$$

The choice of α parameters allow control in removing instabilities observed in standard and averaged nodal formulations. The standard element has problems near incompressibility where it shows volumetric locking, and in bending dominated problems it exhibits a very stiff behaviour. The volumetric locking can be resolved by using the averaged nodal element. To demonstrate the performance of the two formulations a beam bending case is chosen. A vertical cantilever beam of length $L = 10\,\text{m}$ and width $w = 1\,\text{m}$, is considered as shown in the figure 2-4. The beam is fixed at the bottom and punched at the top half with a velocity of $v_0 = 2.0\,\text{m/s}$. The material properties of the beam are ($E = 1.17 \times 10^7\,\text{Pa}$, $\nu = 0.49$ and $\rho = 1.1 \times 10^3\,\text{kg/m}^3$). The solution was computed at $t = 0.5\,\text{s}$.

Figure 2-5 demonstrates how the averaged nodal element can be used to resolve the problems

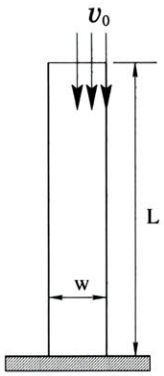

Figure 2-4: A schematic of the beam bending case used to demonstrate the performance of the standard and averaged nodal element.

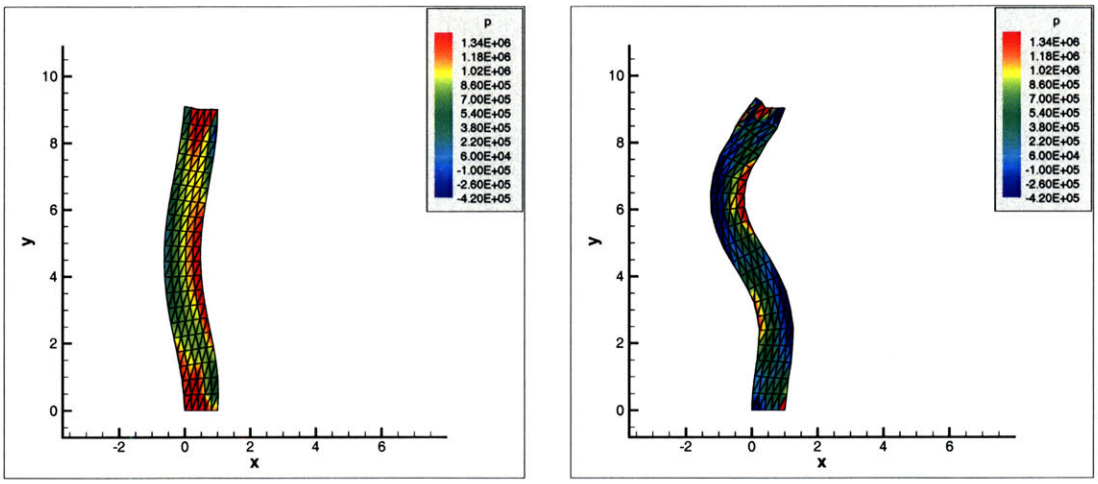

Figure 2-5: The standard element (left) shows excessive stiff behaviour undergoing less deformation. The averaged nodal element (right) does not show any volumetric locking, undergoing larger deformations.

with the standard element.

On the other hand, the average nodal element, develops mechanisms in some 2D plane strain cases [75]. To demonstrate the performance of the averaged nodal element, the same beam bending case is considered, with a Poisson's ratio of $\nu = 0.35$. It is observed that the averaged nodal element shows some hour-glass modes, where it undergoes unphysical shear deformation (shear locking). To remedy this problem, the stabilized formulation, mentioned above is used, with $\alpha_{\text{dev}} = 1$ and $\alpha_{\text{vol}} = 0$, implying that it has the averaged nodal pressures, and the deviatoric stresses of the standard element. The solutions obtained from the two formulations are compared in figure 2-6.

This combination of ($\alpha_{\text{dev}} = 1$) and ($\alpha_{\text{vol}} = 0$) has been tried in simulation of plane

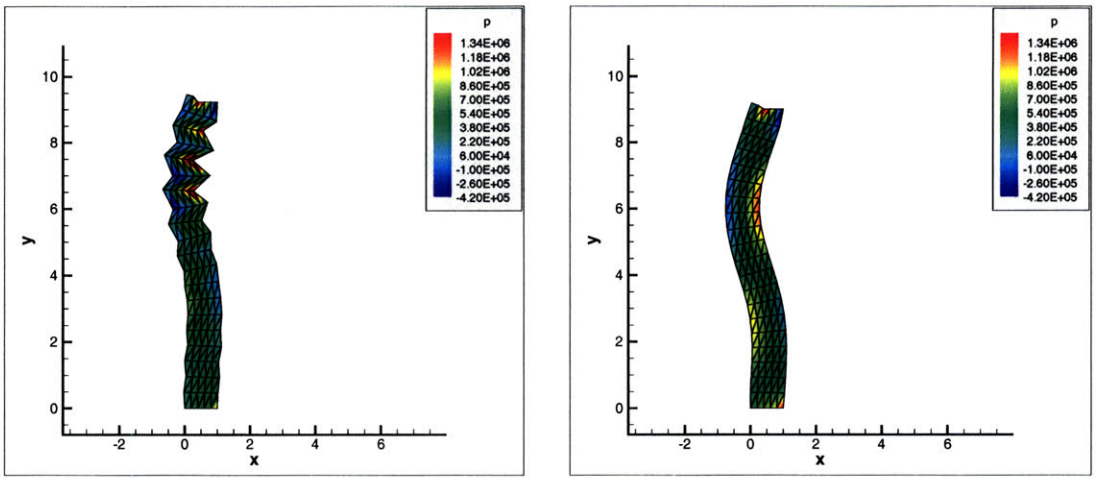

Figure 2-6: The averaged nodal element shows shear locking (left) which is rectified by the stabilized element (right)

strain problems without any apparent non-physical behaviour. It has to be noted, that for all choices of α_{dev} and α_{vol}, the element formulation remains variationally consistent.

2.8.2 Viscous stabilization

Time-integration methods are known to have dispersive errors which begin to corrupt the solution over time. Especially in case of non-linear problems this issue becomes even more severe. Due to the non-linearity, there is a strong coupling within the different modes in the solution, which creates an exchange between the high frequency eigenmodes and low frequency eigenmodes.

In the present case, variational methods have been presented, which ensure conservation of linear and angular momentum. But no promise is made in terms of conservation of energy. Although the energy is not conserved exactly, it has been found that the energy remains bounded for long time integrations. But in case of severe non-linearities, there might be some high frequency non-physical mechanism growing in the system, which needs to be damped. Hence, there arises a need of a stabilizing viscous term which would damp, the very high frequency modes, and yet would not dissipate the low frequency modes, which would be of interest.

A dissipation term has been developed under the variational framework. The idea of using viscous terms for stabilization is quite intuitive, but in order to maintain the conser-

vation property of the system, the viscous stabilization has to be momentum conserving. In addition, the dissipation term has to be of a higher order in order to have minimal effect on the net energy of the system. Similar to the development of the potential energy, where a deformation gradient was used, here a velocity gradient is introduced:

$$\begin{aligned} \boldsymbol{d}(\boldsymbol{v}_{n-1/2}) &= \frac{1}{2}\left(\nabla \boldsymbol{v}_{n-1/2} + \nabla^T \boldsymbol{v}_{n-1/2}\right) \\ d_{ij} &= \frac{1}{2}\left(\frac{\partial v_i^{n-1/2}}{\partial x_j} + \frac{\partial v_j^{n-1/2}}{\partial x_i}\right) \end{aligned} \tag{2.103}$$

which can be split into deviatoric and volumetric parts as:

$$\begin{aligned} \boldsymbol{d} &= \boldsymbol{d}_{\text{dev}} + \boldsymbol{d}_{\text{vol}} \\ d_{ij}^{\text{dev}} &= \left(d_{ij} - \frac{d_{kk}}{3}\delta_{ij}\right) \\ d_{ij}^{\text{vol}} &= \left(\frac{d_{kk}}{3}\delta_{ij}\right) \end{aligned} \tag{2.104}$$

such that $(d_{ii}^{\text{dev}} = 0)$. For linear elements these velocity gradients are constant within the element. Then, the velocity gradients are recovered at the nodes, and an average velocity gradient is computed at the element by the expression:

$$\begin{aligned} \hat{\boldsymbol{d}}^a &= \left(\frac{\int_{V_e:e\in a} \boldsymbol{d}^e dV_e}{\int_{V_e:e\in a} dV_e}\right) \\ \bar{\boldsymbol{d}}^e &= \boldsymbol{N}_e^a \hat{\boldsymbol{d}}^a \end{aligned} \tag{2.105}$$

In case of linear triangular element, this simply becomes:

$$\begin{aligned} \hat{\boldsymbol{d}}^a &= \left(\frac{\sum_{V_e:e\in a} \boldsymbol{d}^e V_e}{\sum_{V_e:e\in a} V_e}\right) \\ \bar{\boldsymbol{d}}^e &= \frac{1}{3}\sum_{a:a\in e} \hat{\boldsymbol{d}}^a \end{aligned} \tag{2.106}$$

Note here that the $\bar{\boldsymbol{d}}^e$ is the value calculated at the centroid of the triangle. It shall be shown later on that this will be sufficient for further calculations. Now a Dissipation Potential Φ

can be defined as:

$$\Phi(\boldsymbol{x}_n, \boldsymbol{v}_{n-1/2}) = \int_{V_n} \phi(\boldsymbol{d}^e) dV_n \tag{2.107}$$

$$\phi(\boldsymbol{d}^e) = \phi_{\text{dev}}(\boldsymbol{d}^e_{\text{dev}}) + \phi_{\text{vol}}(\boldsymbol{d}^e_{\text{vol}}) \tag{2.108}$$

$$\phi_{\text{dev}}(\boldsymbol{d}^e_{\text{dev}}) = \nu_{\text{dev}}(\boldsymbol{d}^e_{\text{dev}} : \boldsymbol{d}^e_{\text{dev}}) \tag{2.109}$$

$$\phi_{\text{vol}}(\boldsymbol{d}^e_{\text{vol}}) = \frac{1}{2}\nu_{\text{vol}}(\boldsymbol{d}^e_{\text{vol}} : \boldsymbol{d}^e_{\text{vol}}) \tag{2.110}$$

where ν_{dev} and ν_{vol} are the viscosities. Similarly, a dissipation potential based on smoothed rate of deformation gradients can be calculated as:

$$\bar{\Phi}(\boldsymbol{x}_n, \boldsymbol{v}_{n-1/2}) = \sum_a \bar{\phi}(\hat{\boldsymbol{d}}^a) V^a_n \tag{2.111}$$

$$\bar{\phi}(\hat{\boldsymbol{d}}^a) = \bar{\phi}_{\text{dev}}(\hat{\boldsymbol{d}}^a_{\text{dev}}) + \bar{\phi}_{\text{vol}}(\hat{\boldsymbol{d}}^a_{\text{vol}}) \tag{2.112}$$

$$\bar{\phi}_{\text{dev}}(\hat{\boldsymbol{d}}^a_{\text{dev}}) = \nu_{\text{dev}}(\hat{\boldsymbol{d}}^a_{\text{dev}} : \hat{\boldsymbol{d}}^a_{\text{dev}}) \tag{2.113}$$

$$\bar{\phi}_{\text{vol}}(\hat{\boldsymbol{d}}^a_{\text{vol}}) = \frac{1}{2}\nu_{\text{vol}}(\hat{\boldsymbol{d}}^a_{\text{vol}} : \hat{\boldsymbol{d}}^a_{\text{vol}}) \tag{2.114}$$

So far, using the rate of deformation tensor, we have defined dissipation potentials which are a function of $\boldsymbol{v}_{n-1/2}$. In presence of viscosity, Hamilton's principle of stationary action (2.56) modifies to:

$$D_n S[\delta \boldsymbol{v}_n] = \Delta t D_n \Phi[\delta \boldsymbol{v}_n] \tag{2.115}$$

$$\frac{\partial S}{\partial \boldsymbol{x}^n_a} = \Delta t \frac{\partial \Phi(\boldsymbol{x}_n, \boldsymbol{v}_{n-1/2})}{\partial \boldsymbol{v}^a_{n-1/2}} \tag{2.116}$$

Now, expressing the action integral in terms of Kinetic energy integral and potential energy integrals as shown in 2.57 equation, we obtain:

$$\frac{\partial K_{n,n+1}}{\partial \boldsymbol{x}^n_a} - \Delta t \frac{\partial \Pi^{\text{ext}}_n}{\partial \boldsymbol{x}^n_a} - \Delta t \frac{\partial \Pi^{\text{int}}_n}{\partial \boldsymbol{x}^n_a} + \frac{\partial K_{n-1,n}}{\partial \boldsymbol{x}^n_a} = \Delta t \frac{\partial \Phi(\boldsymbol{x}_n, \boldsymbol{v}_{n-1/2})}{\partial \boldsymbol{v}^a_{n-1/2}} \tag{2.117}$$

Now, using the relation between $\boldsymbol{v}_{n-1/2}$ and $\boldsymbol{x}_n$ as:

$$\begin{aligned} \boldsymbol{v}^a_{n-1/2} &= \frac{\boldsymbol{x}^a_n - \boldsymbol{x}^a_{n-1}}{\Delta t} \\ \frac{\partial \boldsymbol{v}^a_{n-1/2}}{\partial \boldsymbol{x}^a_n} &= \frac{1}{\Delta t} \end{aligned} \tag{2.118}$$

The equation 2.117 can be written as:

$$\begin{aligned} \frac{\partial K_{n,n+1}}{\partial \boldsymbol{x}^n_a} - \Delta t \frac{\partial \Pi^{\text{ext}}_n}{\partial \boldsymbol{x}^n_a} - \Delta t \frac{\partial \Pi^{\text{int}}_n}{\partial \boldsymbol{x}^n_a} + \frac{\partial K_{n-1,n}}{\partial \boldsymbol{x}^n_a} &= \Delta t^2 \frac{\partial \Phi(\boldsymbol{x}_n, \boldsymbol{v}_{n-1/2})}{\partial \boldsymbol{x}^a_n} \\ \frac{\partial K_{n,n+1}}{\partial \boldsymbol{x}^n_a} - \Delta t \frac{\partial \Pi^{\text{ext}}_n}{\partial \boldsymbol{x}^n_a} - \Delta t \frac{\partial \left(\Pi^{\text{int}}_n + \Delta t \Phi\right)}{\partial \boldsymbol{x}^n_a} + \frac{\partial K_{n-1,n}}{\partial \boldsymbol{x}^n_a} &= 0 \end{aligned} \tag{2.119}$$

In order to incorporate a higher order dissipation potential, the difference of standard dissipation potential Φ and nodally averaged potential $\bar{\Phi}$ is used. This leads to stabilization of the internal energy in the following manner:

$$\Pi^{\text{vstab}}_n(\boldsymbol{x}_n, \boldsymbol{v}_{n-1/2}) = \Pi^{\text{kstab}}_n(\boldsymbol{x}_n) + \Delta t \left(\Phi(\boldsymbol{x}_n, \boldsymbol{v}_{n-1/2}) - \bar{\Phi}(\boldsymbol{x}_n, \boldsymbol{v}_{n-1/2})\right) \tag{2.120}$$

Note that the additional terms are invariant to rigid body displacements and rotations, hence they do not disturb the momentum conservation property of any variationally consistent algorithm. Now the derivatives of the Dissipation Potentials are studied. First the standard Dissipation Potential Φ is considered. The derivative of this potential with respect to $\boldsymbol{x}^b$ can be written as:

$$\begin{aligned} \frac{\partial \Phi}{\partial x^b_i} &= \sum_{e:(e,a)\in b} \frac{\partial \phi^e}{\partial x^a_i} V^e \\ &= \sum_{e:(e,a)\in b} \frac{\partial \phi^e_{\text{dev}}}{\partial x^a_i} + \frac{\partial \phi^e_{\text{vol}}}{\partial x^a_i} V^e \\ &= \sum_e \left[\left\{ \frac{\partial \phi^e_{\text{dev}}}{\partial (d_{\text{dev}})^e_{kl}} \frac{\partial (d_{\text{dev}})^e_{kl}}{\partial x^a_i} \right\} + \left\{ \frac{\partial \phi^e_{\text{vol}}}{\partial (d_{\text{vol}})^e_{kl}} \frac{\partial (d_{\text{vol}})^e_{kl}}{\partial x^a_i} \right\} \right] V^e \end{aligned} \tag{2.121}$$

Using equations 2.109 and 2.110 one can obtain:

$$\frac{\partial \phi^e_{\text{dev}}}{\partial (d_{\text{dev}})^e_{kl}} = 2\nu_{\text{dev}}(d_{\text{dev}})^e_{kl} \tag{2.122}$$

$$\frac{\partial \phi^e_{\text{vol}}}{\partial (d_{\text{vol}})^e_{kl}} = \nu_{\text{vol}}(d_{\text{vol}})^e_{kl} \tag{2.123}$$

Now, considering only the deviatoric part:

$$\begin{aligned}
\sum_e \left\{ \frac{\partial \phi^e_{\text{dev}}}{\partial (d_{\text{dev}})^e_{kl}} \frac{\partial (d_{\text{dev}})^e_{kl}}{\partial x^a_i} \right\} V^e &= \sum_e 2\nu_{\text{dev}}(d_{\text{dev}})^e_{kl} \frac{\partial (d_{\text{dev}})^e_{kl}}{\partial x^a_i} V^e \\
&= \sum_e \frac{2\nu_{\text{dev}}(d_{\text{dev}})^e_{kl}}{\Delta t} \left\{ \frac{\partial N^e_a}{\partial x_j} \left(\frac{\delta_{ik}\delta_{lj} + \delta_{il}\delta_{kj}}{2} - \frac{\delta_{ij}\delta_{kl}}{3} \right) \right\} V^e \\
&= \sum_e \frac{2\nu_{\text{dev}}(d_{\text{dev}})^e_{ij}}{\Delta t} \frac{\partial N^e_a}{\partial x_j} V^e
\end{aligned} \tag{2.124}$$

Now, considering the volumetric part:

$$\begin{aligned}
\sum_e \left\{ \frac{\partial \phi^e_{\text{vol}}}{\partial (d_{\text{vol}})^e_{kl}} \frac{\partial (d_{\text{vol}})^e_{kl}}{\partial x^a_i} \right\} V^e &= \sum_e \nu_{\text{vol}}(d_{\text{vol}})^e_{kl} \frac{\partial (d_{\text{vol}})^e_{kl}}{\partial x^a_i} V^e \\
&= \sum_e \frac{\nu_{\text{vol}}(d_{\text{vol}})^e_{kl}}{\Delta t} \left\{ \frac{\partial N^e_a}{\partial x_j} \left(\frac{\delta_{ij}\delta_{kl}}{3} \right) \right\} V^e \\
&= \sum_e \frac{\nu_{\text{vol}}(d_{\text{vol}})^e_{ij}}{\Delta t} \frac{\partial N^e_a}{\partial x_j} V^e
\end{aligned} \tag{2.125}$$

Thus, the derivative of the standard dissipation potential becomes:

$$\Delta t \frac{\partial \Phi}{\partial x^b_i} = \sum_{e:(e,a)\in b} \frac{\partial N^e_a}{\partial x_j} \left\{ 2\nu_{\text{dev}}(d_{\text{dev}})^e_{ij} + \nu_{\text{vol}}(d_{\text{vol}})^e_{ij} \right\} V^e \tag{2.126}$$

Now, considering the averaged nodal dissipation potential:

$$\begin{aligned}
\frac{\partial \bar{\Phi}}{\partial x^b_i} &= \sum_c \left[\left\{ \frac{\partial \phi^c_{\text{dev}}}{\partial (\hat{d}_{\text{dev}})^c_{kl}} \frac{\partial (\hat{d}_{\text{dev}})^c_{kl}}{\partial x^b_i} \right\} + \left\{ \frac{\partial \phi^c_{\text{vol}}}{\partial (\hat{d}_{\text{vol}})^c_{kl}} \frac{\partial (\hat{d}_{\text{vol}})^c_{kl}}{\partial x^b_i} \right\} \right] \hat{V}^c \\
&= \sum_c \left[\left\{ 2\nu_{\text{dev}}(\hat{d}_{\text{dev}})^c_{kl} \frac{\partial (\hat{d}_{\text{dev}})^c_{kl}}{\partial x^b_i} \right\} + \left\{ \nu_{\text{vol}}(\hat{d}_{\text{vol}})^c_{kl} \frac{\partial (\hat{d}_{\text{vol}})^c_{kl}}{\partial x^b_i} \right\} \right] \hat{V}^c
\end{aligned} \tag{2.127}$$

Now, considering only the deviatoric part:

$$\sum_c \left\{ 2\nu_{\text{dev}} (\hat{d}_{\text{dev}})^c_{kl} \frac{\partial (\hat{d}_{\text{dev}})^c_{kl}}{\partial x^b_i} \right\} \hat{V}^c = \sum_c \left\{ \frac{2\nu_{\text{dev}}}{\eta \hat{V}^c} (\hat{d}_{\text{dev}})^c_{kl} \frac{\partial}{\partial x^b_i} \left(\sum_{e \in c} (d_{\text{dev}})^e_{kl} V^e \right) \right\} \hat{V}^c \tag{2.128}$$

where $\hat{V}^c = \sum_{e \in c} V^e / \eta$ is the nodal volume at node c, and η is 3 for triangles and 4 for tetrahedra. Further simplifying this equation leads to:

$$\begin{aligned}
&= \sum_c \left\{ \frac{2\nu_{\text{dev}}}{\eta} (\hat{d}_{\text{dev}})^c_{kl} \left(\sum_{e \in c, (e,a) \in b} \frac{\partial}{\partial x^a_i} (d_{\text{dev}})^e_{kl} V^e \right) \right\} \\
&= \sum_c \left\{ \frac{2\nu_{\text{dev}}}{\eta \Delta t} (\hat{d}_{\text{dev}})^c_{kl} \left(\sum_{e \in c, (e,a) \in b} \frac{\partial N^e_a}{\partial x_j} \left(\frac{\delta_{ik}\delta_{lj} + \delta_{il}\delta_{kj}}{2} - \frac{\delta_{ij}\delta_{kl}}{3} \right) V^e \right) \right\} \\
&= \sum_c \left\{ \frac{2\nu_{\text{dev}}}{\eta \Delta t} (\hat{d}_{\text{dev}})^c_{kl} \left(\frac{\delta_{ik}\delta_{lj} + \delta_{il}\delta_{kj}}{2} - \frac{\delta_{ij}\delta_{kl}}{3} \right) \left(\sum_{e \in c, (e,a) \in b} \frac{\partial N^e_a}{\partial x_j} V^e \right) \right\} \\
&= \sum_c \left\{ \frac{2\nu_{\text{dev}}}{\eta \Delta t} (\hat{d}_{\text{dev}})^c_{ij} \left(\sum_{e \in c, (e,a) \in b} \frac{\partial N^e_a}{\partial x_j} V^e \right) \right\} \\
&= \sum_{(e,a) \in b} \left\{ \frac{1}{\Delta t} \frac{\partial N^e_a}{\partial x_j} \left(\sum_{c \in e} \frac{2\nu_{\text{dev}}}{\eta} (\hat{d}_{\text{dev}})^c_{ij} \right) \right\} V^e \\
&= \sum_{(e,a) \in b} \left\{ \frac{1}{\Delta t} \frac{\partial N^e_a}{\partial x_j} 2\nu_{\text{dev}} (\bar{d}_{\text{dev}})^e_{ij} \right\} V^e
\end{aligned} \tag{2.129}$$

Now, looking at the volumetric part:

$$\sum_c \left\{ \nu_{\text{vol}} (\hat{d}_{\text{vol}})^c_{kl} \frac{\partial (\hat{d}_{\text{vol}})^c_{kl}}{\partial x^b_i} \right\} \hat{V}^c = \sum_c \left\{ \frac{\nu_{\text{vol}}}{\eta \hat{V}^c} (\hat{d}_{\text{vol}})^c_{kl} \frac{\partial}{\partial x^b_i} \left(\sum_{e \in c} (d_{\text{vol}})^e_{kl} V^e \right) \right\} \hat{V}^c \tag{2.130}$$

Now, simplifying in a similar manner shown in equation 2.129:

$$
\begin{aligned}
&= \sum_c \left\{ \frac{\nu_{\text{vol}}}{\eta} (\hat{d}_{\text{vol}})^c_{kl} \left(\sum_{e \in c,(e,a) \in b} \frac{\partial}{\partial x^a_i} (d_{\text{vol}})^e_{kl} V^e \right) \right\} \\
&= \sum_c \left\{ \frac{\nu_{\text{vol}}}{\eta \Delta t} (\hat{d}_{\text{vol}})^c_{kl} \left(\sum_{e \in c,(e,a) \in b} \frac{\partial N^e_a}{\partial x_j} \left(\frac{\delta_{ij}\delta_{kl}}{3} \right) V^e \right) \right\} \\
&= \sum_c \left\{ \frac{\nu_{\text{vol}}}{\eta \Delta t} (\hat{d}_{\text{vol}})^c_{kl} \left(\frac{\delta_{ij}\delta_{kl}}{3} \right) \left(\sum_{e \in c,(e,a) \in b} \frac{\partial N^e_a}{\partial x_j} V^e \right) \right\} \\
&= \sum_c \left\{ \frac{\nu_{\text{vol}}}{\eta \Delta t} (\hat{d}_{\text{vol}})^c_{ij} \left(\sum_{e \in c,(e,a) \in b} \frac{\partial N^e_a}{\partial x_j} V^e \right) \right\} \\
&= \sum_{(e,a) \in b} \left\{ \frac{1}{\Delta t} \frac{\partial N^e_a}{\partial x_j} \left(\sum_{c \in e} \frac{\nu_{\text{vol}}}{\eta} (\hat{d}_{\text{vol}})^c_{ij} \right) \right\} V^e \\
&= \sum_{(e,a) \in b} \left\{ \frac{1}{\Delta t} \frac{\partial N^e_a}{\partial x_j} \nu_{\text{vol}} (\bar{d}_{\text{vol}})^e_{ij} \right\} V^e
\end{aligned} \tag{2.131}
$$

Thus, the derivative of the averaged nodal dissipation potential becomes:

$$
\Delta t \frac{\partial \bar{\Phi}}{\partial x^b_i} = \sum_{e:(e,a) \in b} \frac{\partial N^e_a}{\partial x_j} \left\{ 2\nu_{\text{dev}} (\bar{d}_{\text{dev}})^e_{ij} + \nu_{\text{vol}} (\bar{d}_{\text{vol}})^e_{ij} \right\} V^e \tag{2.132}
$$

Thus, based on equations 2.126 and 2.132, the stabilization of the Potential Energy, leads to stabilized stresses in the elements, which can be calculated as:

$$
\boldsymbol{\sigma}^{\text{vstab}} = \boldsymbol{\sigma}^{\text{kstab}} + 2\nu_{\text{dev}} \left(\boldsymbol{d}_{\text{dev}} - \bar{\boldsymbol{d}}_{\text{dev}} \right) + \nu_{\text{vol}} \left(\boldsymbol{d}_{\text{vol}} - \bar{\boldsymbol{d}}_{\text{vol}} \right) \tag{2.133}
$$

Clearly the changes in the stresses are variationally consistent. The viscosities can be non-dimensionalized based on mesh size as:

$$
\nu_{\text{dev}} = \tilde{\nu}_{\text{dev}} \frac{\rho \Delta x^2}{\Delta t} \tag{2.134}
$$

$$
\nu_{\text{vol}} = \tilde{\nu}_{\text{vol}} \frac{\rho \Delta x^2}{\Delta t} \tag{2.135}
$$

Thus, the amount of dissipation could be controlled by the non-dimensionalised parameters $\tilde{\nu}_{\text{dev}}$ and $\tilde{\nu}_{\text{vol}}$. A typical choice of 1, was effective to damp high frequency noise. To study

the effect of such a dissipation term the following tests were conducted.

Patch Test

As a patch test, for the damping term, the stresses on a unit square plate, with the following position and velocity field $(\boldsymbol{x}, \boldsymbol{v})$ was calculated.

$$\begin{aligned} x &= \epsilon\left(a_x + b_x X + c_x Y + d_x X^2 + e_x Y^2 + f_x XY\right) \\ y &= \epsilon\left(a_y + b_y X + c_y Y + d_y X^2 + e_y Y^2 + f_y XY\right) \\ v_x &= \frac{\epsilon}{\Delta t_{\text{ref}}}\left(a_x + b_x x + c_x y + d_x x^2 + e_x y^2 + f_x xy\right) \\ v_y &= \frac{\epsilon}{\Delta t_{\text{ref}}}\left(a_y + b_y x + c_y y + d_y x^2 + e_y y^2 + f_y xy\right) \end{aligned} \tag{2.136}$$

where $(a_x, b_x, c_x, d_x, e_x, f_x)$ and $(a_y, b_y, c_y, d_y, e_y, f_y)$ were non-zero constants. The average stress computed as:

$$\bar{\boldsymbol{\sigma}} = \frac{\sum_e \left(\boldsymbol{\sigma}^{\text{vstab}} - \boldsymbol{\sigma}^{\text{kstab}}\right)_e A_e^0}{\sum_e A_e^0} \tag{2.137}$$

The average stabilized stresses $(\bar{\boldsymbol{\sigma}})$ were compared for different mesh sizes as shown in figure 2-7. In the above case, $\epsilon = 0.1\text{m}$, $\Delta t_{\text{ref}} = 0.01\text{s}$ and unit values for all the above constants were chosen. The viscous parts of the stabilized stress which were the dissipation terms only, showed a quadratic dependance on mesh size, and hence was a higher order term.

Beam Bending

Next the dynamic solution of cantilever beam was computed, exciting its first (lowest) eigen-mode, for almost 20 cycles, to study the behaviour of the dissipation as shown in figure 2-8. The beam was $L = 20\text{m}$ long along the Y direction, and $w = 1\text{m}$ wide along X direction, hence it could be considered a slender beam. Using Euler-Bernoulli beam theory,

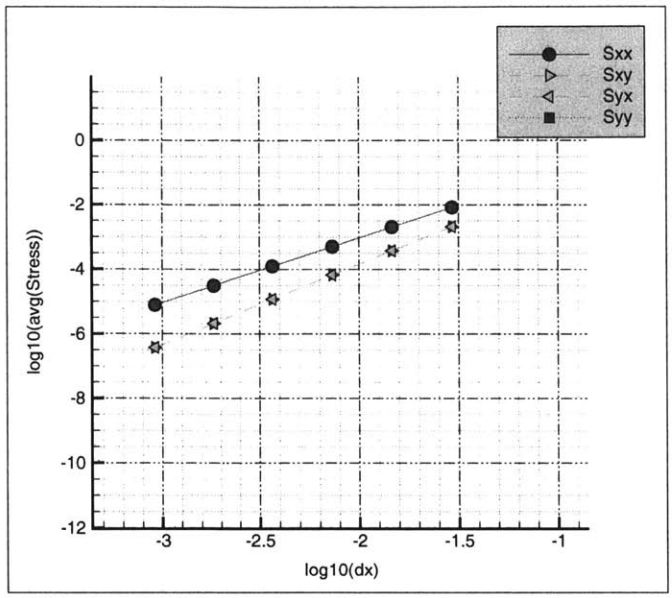

Figure 2-7: Patch test showing the mesh dependancy of the viscous parts of the average stabilized stresses.

the eigen-modes, are:

$$u(Y) = \delta\left[\{cos(kY) - cosh(kY)\} + \frac{\{-cos(kL) - cosh(kL)\}}{\{sin(kL) + sinh(kL)\}}\{sin(kY) - sinh(kY)\}\right] \tag{2.138}$$

where the eigenvalues are discrete values of kL, the lowest eigenvalue being $kL = 1.875105$, and δ was the initial deformation. Based on this, the initial deformation of the beam was set as:

$$\boldsymbol{x} = \boldsymbol{X} + \boldsymbol{u} \tag{2.139}$$

$$\boldsymbol{u} = \begin{Bmatrix} u(Y) \\ -u'(Y)\left(X - \left(\frac{w}{2}\right)\right) \end{Bmatrix} \tag{2.140}$$

and the value of delta chosen was ($\delta = 0.001$m). To test the dissipation term, the non-dimensional terms chosen were ($\tilde{\nu}_{\text{dev}} = \tilde{\nu}_{\text{vol}} = 0.01$) and the solution and the energy was monitored over the solution. The energy was assumed to be decaying in the following

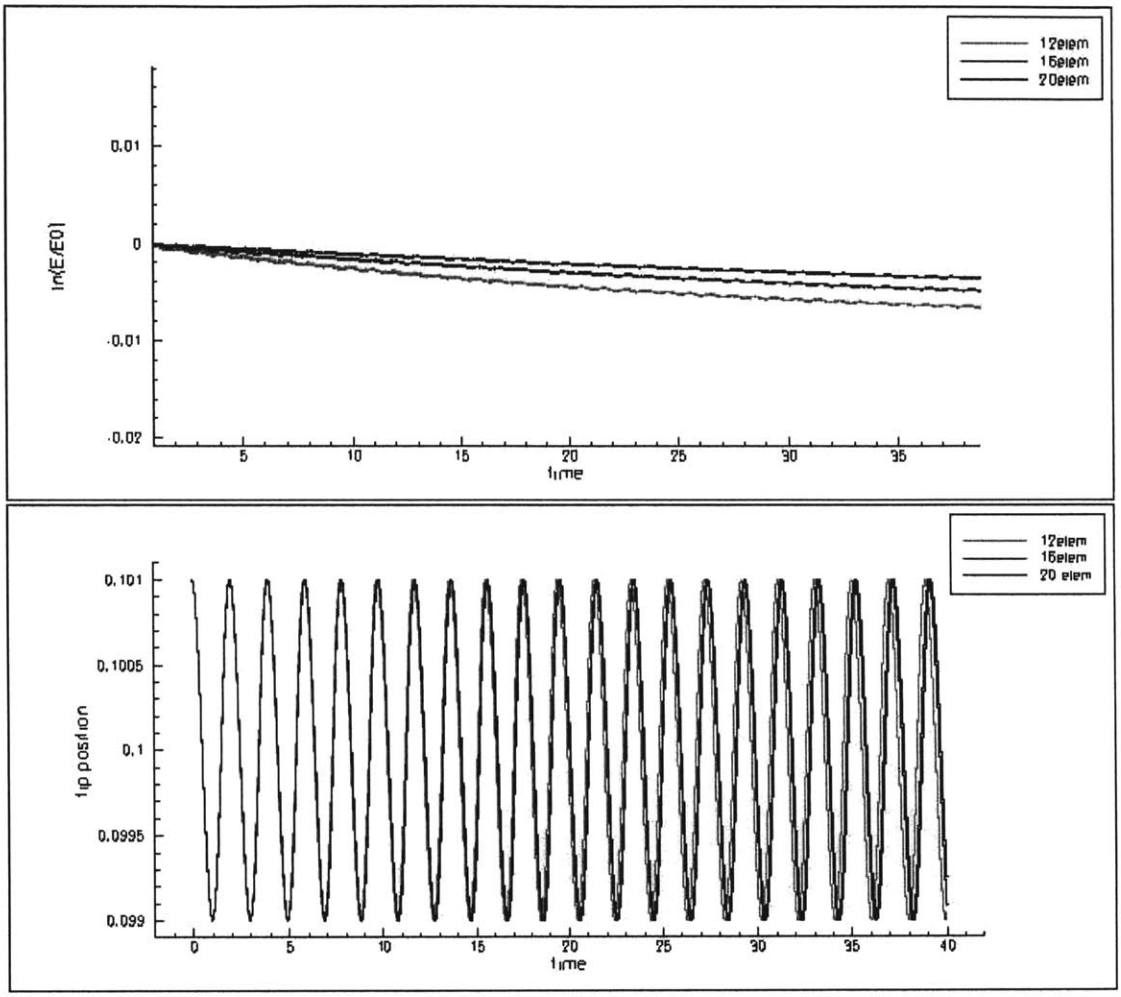

Figure 2-8: The energy history and the tip deflection for cantilever beam.

manner:

$$\begin{aligned} E(t) &= E_0 e^{-at} \\ \dot{E}(t) &= -a\,E(t) \\ \frac{\partial}{\partial t}\left\{\ln\left(\frac{E}{E_0}\right)\right\} &= a \\ a &= Ch^{\alpha} \end{aligned} \tag{2.141}$$

where α would be the order of the energy decay. Tip deflection solutions were computed upto a common time instant for different meshes, and the energy decay rate was computed

from the energy history, using a regression relation as follows:

$$y = \ln\left(\frac{E}{E_0}\right) \tag{2.142}$$

$$\dot{y} = \frac{\dot{E}}{E} = a \approx \frac{(\sum t_i y_i) - (\sum t_i)(\sum y_i)}{(\sum t_i^2) - (\sum t_i)(\sum t_i)} \tag{2.143}$$

Due to the decay nature, the absolute value of a ($|a|$) was monitored, for different mesh levels as shown in figure 2-9 The energy decay rates showed close to quadratic dependance

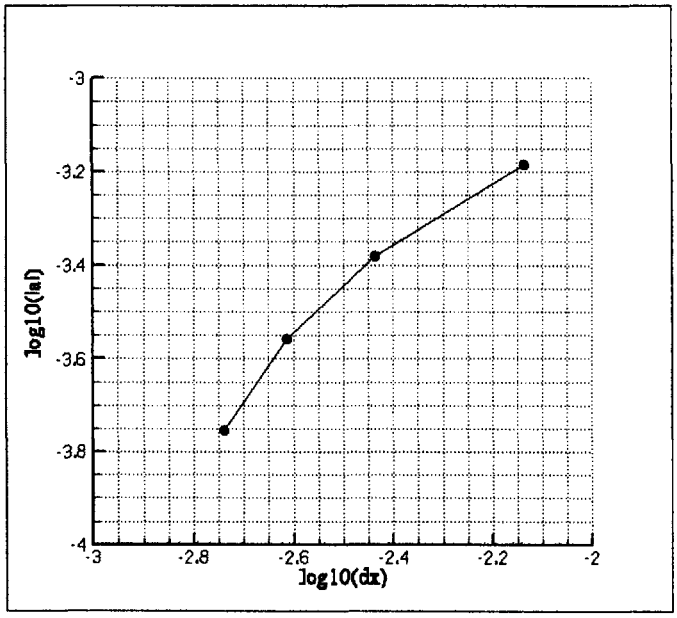

Figure 2-9: Energy decay rate variations with mesh size for beam bending.

($\alpha = 1.7$) on mesh size for finer meshes 2-9, which was in accordance with the previous observation in patch test. The the viscous stabilization is a high order dissipation term, which becomes negligible in case of very fine meshes.

This dissipation term could be generically used in cases of explicit time integration, just to filter out the high frequency noise generated due to the dispersion errors. It becomes even more effective in case of non-linear problems. The non-dimensionalised parameters $\tilde{\nu}_{\text{dev}}$ and $\tilde{\nu}_{\text{vol}}$ were typically chosen to be 1 or less.

Chapter 3

Mesh Adaptation

In this section, the previously mentioned variational formulation, is extended to mesh adaptation. Mesh adaptations which involve local mesh changes for 2D triangular meshes, are considered. The following operations are formulated separately:

1. Diagonal Swapping.
2. Node Movement.
3. Edge Splitting.
4. Edge Collapsing.

Each of these operations is developed with the assumption that only one of these operations takes place between time level n and $n+1$ on a local patch.

3.1 Diagonal Swapping

A discussion of diagonal swapping is presented, by studying a local patch of two triangular elements *abc* and *acd* at time level t_n, as shown in Fig. 3-1. The patch is time marched to time level t_{n+1} where the common diagonal *ac* is swapped with the new diagonal *bd*, thus leading to two different element configurations, *abd* and *bcd* at time level t_{n+1}. The space-time volume thus formed, can be subdivided into five tetrahedra: $(a_n b_n c_n b_{n+1})$, $(a_n c_n d_n d_{n+1})$, $(a_{n+1} b_{n+1} d_{n+1} a_n)$, $(b_{n+1} c_{n+1} d_{n+1} c_n)$ and $(a_n c_n b_{n+1} d_{n+1})$ as shown in the

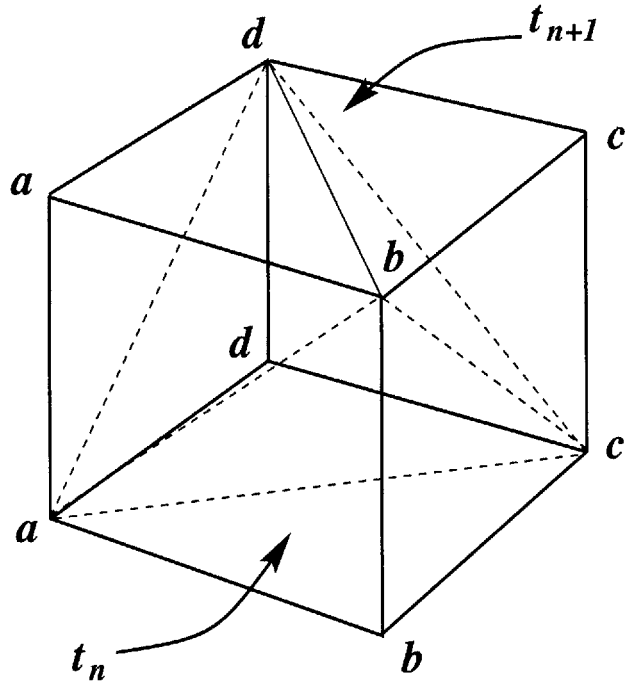

Figure 3-1: The space-time volume for the diagonal swapping.

figure 3-1. Note that, the first four tetrahedra, have common nodes, hence the velocity interpolation is simple. The velocity in the fifth(central) tetrahedra is computed by the full expression, (as explained in chapter 2). Hence, the net Kinetic Energy Integral within the space-time volume can be written as:

$$\begin{aligned} K^{abcd}_{n,n+1} &= \frac{\Delta t}{2}\frac{m_{abc}}{3}\boldsymbol{v}^b_{n+1/2}\cdot\boldsymbol{v}^b_{n+1/2} + \frac{\Delta t}{2}\frac{m_{acd}}{3}\boldsymbol{v}^d_{n+1/2}\cdot\boldsymbol{v}^d_{n+1/2} + \frac{\Delta t}{2}\frac{m_{abd}}{3}\boldsymbol{v}^a_{n+1/2}\cdot\boldsymbol{v}^a_{n+1/2} \\ &\quad + \frac{\Delta t}{2}\frac{m_{bcd}}{3}\boldsymbol{v}^c_{n+1/2}\cdot\boldsymbol{v}^c_{n+1/2} + \frac{\Delta t}{2}\frac{m_{abcd}}{3}\boldsymbol{v}^{abcd}_{n+1/2}\cdot\boldsymbol{v}^{abcd}_{n+1/2} \qquad (3.1) \\ \boldsymbol{v}^{abcd}_{n+1/2} &= \frac{\left(m_{acd}\boldsymbol{x}^b_{n+1} + m_{abc}\boldsymbol{x}^d_{n+1} - m_{bcd}\boldsymbol{x}^a_n + m_{abd}\boldsymbol{x}^c_n\right)}{\Delta t m_{abcd}} \qquad (3.2) \end{aligned}$$

Using stationarity *wrt.* $\boldsymbol{x}_n$, the equilibrium relations at t_n are obtained as:

$$\begin{aligned} -D_1 K^{abcd}_{n,n+1}[\delta\boldsymbol{x}_n] &= \frac{m_{abc}}{3}\boldsymbol{v}^b_{n+1/2}\cdot\delta\boldsymbol{x}^b_n + \frac{m_{acd}}{3}\boldsymbol{v}^d_{n+1/2}\cdot\delta\boldsymbol{x}^d_n \\ &+ \left(\frac{m_{abd}}{3}\boldsymbol{v}^a_{n+1/2} + \frac{m_{bcd}}{3}\boldsymbol{v}^{abcd}_{n+1/2}\right)\cdot\delta\boldsymbol{x}^a_n \\ &+ \left(\frac{m_{bcd}}{3}\boldsymbol{v}^c_{n+1/2} + \frac{m_{abd}}{3}\boldsymbol{v}^{abcd}_{n+1/2}\right)\cdot\delta\boldsymbol{x}^c_n \qquad (3.3) \end{aligned}$$

Similarly, using stationarity *wrt.* $\boldsymbol{x}_{n+1}$, the equilibrium relations at t_{n+1} are obtained as:

$$\begin{aligned} -D_2 K^{abcd}_{n,n+1}[\delta \boldsymbol{x}_{n+1}] &= \frac{m_{abd}}{3} \boldsymbol{v}^a_{n+1/2} \cdot \delta \boldsymbol{x}^a_{n+1} + \frac{m_{bcd}}{3} \boldsymbol{v}^c_{n+1/2} \cdot \delta \boldsymbol{x}^c_{n+1} \\ &+ \left(\frac{m_{abc}}{3} \boldsymbol{v}^b_{n+1/2} + \frac{m_{acd}}{3} \boldsymbol{v}^{abcd}_{n+1/2} \right) \cdot \delta \boldsymbol{x}^b_{n+1} \\ &+ \left(\frac{m_{acd}}{3} \boldsymbol{v}^d_{n+1/2} + \frac{m_{abc}}{3} \boldsymbol{v}^{abcd}_{n+1/2} \right) \cdot \delta \boldsymbol{x}^d_{n+1} \end{aligned} \tag{3.4}$$

Thus, the finite element algorithm at step t_n is:

$$M^n_b \left(\boldsymbol{v}^{n+1/2}_b - \boldsymbol{v}^{n-1/2}_b \right) = \Delta t \left(\boldsymbol{F}^b_n - \boldsymbol{T}^b_n \right) \tag{3.5}$$

$$M^n_d \left(\boldsymbol{v}^{n+1/2}_d - \boldsymbol{v}^{n-1/2}_d \right) = \Delta t \left(\boldsymbol{F}^d_n - \boldsymbol{T}^d_n \right) \tag{3.6}$$

Note that as soon as the position of nodes b and d have been updated, using equations 3.5 and 3.6, it is possible to calculate $\boldsymbol{v}^{abcd}_{n+1/2}$ using 3.2 and this update of a and c :

$$M^{n+1}_a \boldsymbol{v}^{n+1/2}_a - M^n_a \boldsymbol{v}^{n-1/2}_a + \frac{m_{bcd}}{3} \boldsymbol{v}^{n+1/2}_{abcd} = \Delta t \left(\boldsymbol{F}^a_n - \boldsymbol{T}^a_n \right) \tag{3.7}$$

$$M^{n+1}_c \boldsymbol{v}^{n++/2}_c - M^n_c \boldsymbol{v}^{n-1/2}_c + \frac{m_{abd}}{3} \boldsymbol{v}^{n+1/2}_{abcd} = \Delta t \left(\boldsymbol{F}^c_n - \boldsymbol{T}^c_n \right) \tag{3.8}$$

And the finite element algorithm at step t_{n+1} :

$$M^{n+1}_a \left(\boldsymbol{v}^{n+3/2}_a - \boldsymbol{v}^{n+1/2}_a \right) = \Delta t \left(\boldsymbol{F}^a_{n+1} - \boldsymbol{T}^a_{n+1} \right) \tag{3.9}$$

$$M^{n+1}_c \left(\boldsymbol{v}^{n+3/2}_c - \boldsymbol{v}^{n+1/2}_c \right) = \Delta t \left(\boldsymbol{F}^c_{n+1} - \boldsymbol{T}^c_{n+1} \right) \tag{3.10}$$

$$M^{n+1}_b \boldsymbol{v}^{n+3/2}_b - M^n_b \boldsymbol{v}^{n+1/2}_b - \frac{m_{acd}}{3} \boldsymbol{v}^{n+1/2}_{abcd} = \Delta t \left(\boldsymbol{F}^b_{n+1} - \boldsymbol{T}^b_{n+1} \right) \tag{3.11}$$

$$M^{n+1}_d \boldsymbol{v}^{n+3/2}_d - M^n_d \boldsymbol{v}^{n+1/2}_d - \frac{m_{abc}}{3} \boldsymbol{v}^{n+1/2}_{abcd} = \Delta t \left(\boldsymbol{F}^d_{n+1} - \boldsymbol{T}^d_{n+1} \right) \tag{3.12}$$

The momentum within time step t_n and t_{n+1} is ($D_2 L_{n,n+1}$):

$$\boldsymbol{P}_{n,n+1} = \sum_j \boldsymbol{P}^j_{n,n+1} \tag{3.13}$$

$$\boldsymbol{P}^j_{n,n+1} = \begin{cases} M^{n+1}_j \boldsymbol{v}^{n+1/2}_j & \text{for } j = a \text{ or } c, \\ M^n_j \boldsymbol{v}^{n+1/2}_j + (\frac{m_{acd}}{3}) \boldsymbol{v}^{abcd}_{n+1/2} & \text{for } j = b, \\ M^n_j \boldsymbol{v}^{n+1/2}_j + (\frac{m_{abc}}{3}) \boldsymbol{v}^{abcd}_{n+1/2} & \text{for } j = d. \end{cases} \tag{3.14}$$

$$\boldsymbol{H}_{n,n+1} = \sum_j \boldsymbol{x}^j_{n+1} \times \boldsymbol{P}^j_{n,n+1} \tag{3.15}$$

3.2 Edge Splitting

Now another patch of elements as shown in Fig. 3-2, is considered to develop the algorithm for edge-splitting. As shown in the figure, a patch of two triangles, *abd* and *bcd*, at time level t_n, is time marched to time level t_{n+1}. The common edge *bd* is split at midpoint

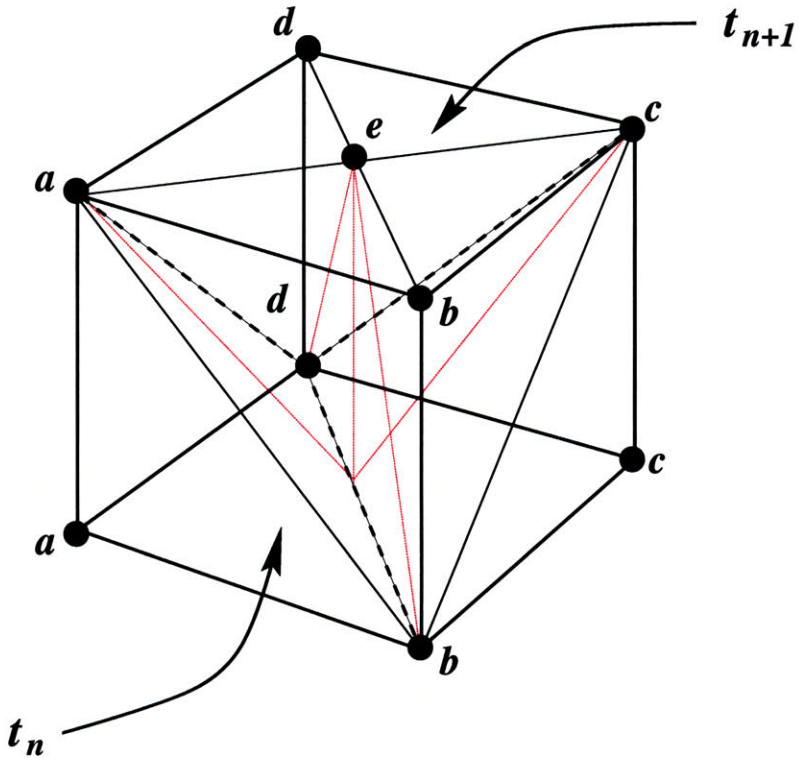

Figure 3-2: The space-time volume for edge splitting.

e to form four child elements, *abe*, *aed*, *bce* and *ecd*, at time level t_{n+1}. The space-time

volume is now subdivided to five tetrahedra: $(a_n b_n d_n a_{n+1})$, $(b_n c_n d_n c_{n+1})$, $(a_n c_n d_n d_{n+1})$, $(a_n c_n b_n b_{n+1})$, and $(b_n d_n a_{n+1} c_{n+1})$. Note that the first four tetrahedra have common nodes, hence the velocity interpolation is simple. The fifth tetrahedra, is further subdivided into four tetrahedra (as shown in red dotted lines in Fig. 3-2), each having a common node as e. The point e and the mid point of b and d have the same reference coordinates, $(\boldsymbol{X}_e = \frac{\boldsymbol{X}_b + \boldsymbol{X}_d}{2})$. Thus the Kinetic Energy Integral can be written as:

$$\begin{aligned} K^{abcd}_{n,n+1} &= \frac{\Delta t}{2}\frac{m_{abd}}{3}\boldsymbol{v}^a_{n+1/2}\cdot\boldsymbol{v}^a_{n+1/2} + \frac{\Delta t}{2}\frac{m_{bcd}}{3}\boldsymbol{v}^c_{n+1/2}\cdot\boldsymbol{v}^c_{n+1/2} \\ &+ \frac{\Delta t}{2}\frac{m_{abe}+m_{bce}}{3}\boldsymbol{v}^c_{n+1/2}\cdot\boldsymbol{v}^c_{n+1/2} + \frac{\Delta t}{2}\frac{m_{dae}+m_{dec}}{3}\boldsymbol{v}^c_{n+1/2}\cdot\boldsymbol{v}^c_{n+1/2} \\ &+ \frac{\Delta t}{2}m_e\boldsymbol{v}^e_{n+1/2}\cdot\boldsymbol{v}^e_{n+1/2} \qquad (3.16) \\ m_e &= \frac{(m_{abd}+m_{bcd})}{3} \qquad (3.17) \\ \boldsymbol{v}^e_{n+1/2} &= \frac{1}{\Delta t}\left[\boldsymbol{x}^e_{n+1} - \frac{(\boldsymbol{x}^b_n + \boldsymbol{x}^d_n)}{2}\right] \qquad (3.18) \end{aligned}$$

Using stationarity *wrt.* $\boldsymbol{x}_n$ one can obtain:

$$\begin{aligned} -D_1 K^{abcd}_{n,n+1}[\delta\boldsymbol{x}_n] &= \frac{m_{abd}}{3}\boldsymbol{v}^a_{n+1/2}\cdot\delta\boldsymbol{x}^a_n + \frac{m_{bcd}}{3}\boldsymbol{v}^c_{n+1/2}\cdot\delta\boldsymbol{x}^c_n \\ &+ \frac{m_{abe}+m_{bce}}{3}\boldsymbol{v}^b_{n+1/2}\cdot\delta\boldsymbol{x}^b_n + \frac{m_{dae}+m_{dec}}{3}\boldsymbol{v}^d_{n+1/2}\cdot\delta\boldsymbol{x}^d_n \\ &+ \frac{m_e}{2}\boldsymbol{v}^e_{n+1/2}\cdot\delta\boldsymbol{x}^b_n + \frac{m_e}{2}\boldsymbol{v}^e_{n+1/2}\cdot\delta\boldsymbol{x}^d_n \qquad (3.19) \end{aligned}$$

Thus, the update algorithm at step t_n :

$$\begin{aligned} M^n_a\left(\boldsymbol{v}^{n+1/2}_a - \boldsymbol{v}^{n-1/2}_a\right) &= \Delta t\left(\boldsymbol{F}^a_n - \boldsymbol{T}^a_n\right) \qquad (3.20) \\ M^n_c\left(\boldsymbol{v}^{n+1/2}_c - \boldsymbol{v}^{n-1/2}_c\right) &= \Delta t\left(\boldsymbol{F}^c_n - \boldsymbol{T}^c_n\right) \qquad (3.21) \end{aligned}$$

$$\begin{aligned} M^{n+1}_b\boldsymbol{v}^{n+1/2}_b - M^n_b\boldsymbol{v}^{n-1/2}_b - \frac{m_e}{2}\boldsymbol{v}^{n+1/2}_e &= \Delta t\left(\boldsymbol{F}^a_n - \boldsymbol{T}^a_n\right) \qquad (3.22) \\ M^{n+1}_d\boldsymbol{v}^{n+1/2}_d - M^n_d\boldsymbol{v}^{n-1/2}_d - \frac{m_e}{2}\boldsymbol{v}^{n+1/2}_e &= \Delta t\left(\boldsymbol{F}^d_n - \boldsymbol{T}^d_n\right) \qquad (3.23) \end{aligned}$$

Choosing the velocity at the new node to be:

$$\boldsymbol{v}_e^{n+1/2} = \frac{1}{2}\left(\boldsymbol{v}_b^{n+1/2} + \boldsymbol{v}_d^{n+1/2}\right) \tag{3.24}$$

Thus a 2×2 system of equation is obtained, to be solved, to obtain the other velocities.

$$\begin{bmatrix} M_b^{n+1} + \frac{1}{4}m_e & \frac{1}{4}m_e \\ \frac{1}{4}m_e & M_d^{n+1} + \frac{1}{4}m_e \end{bmatrix} \begin{bmatrix} \boldsymbol{v}_b^{n+1/2} \\ \boldsymbol{v}_d^{n+1/2} \end{bmatrix} = \begin{bmatrix} M_b^n \boldsymbol{v}_b^{n+1/2} \\ M_d^n \boldsymbol{v}_d^{n+1/2} \end{bmatrix} + \Delta t \begin{bmatrix} \boldsymbol{F}_n^b - \boldsymbol{T}_n^b \\ \boldsymbol{F}_n^d - \boldsymbol{T}_n^d \end{bmatrix} \tag{3.25}$$

The update at equations at $n+1$ are unchanged. The momentum within time step t_n and t_{n+1} is $(D_2 L_{n,n+1})$:

$$\boldsymbol{P}_{n,n+1} = \sum_j \boldsymbol{P}_{n,n+1}^j \tag{3.26}$$

$$\boldsymbol{P}_{n,n+1}^j = M_j^{n+1} \boldsymbol{v}_{n+1/2}^j \qquad \forall\, j$$

$$\boldsymbol{H}_{n,n+1} = \sum_j \boldsymbol{x}_{n+1}^j \times \boldsymbol{P}_{n,n+1}^j \tag{3.27}$$

3.3 Node Movement

In order to initiate a study of node movement, the mapping of the present(spatial) configuration to the reference(material) configuration, is revisited. An arbitrary intermediate configuration(ξ, η) is introduced, as shown in Fig. [3-3], as is typically done in the case of Arbitrary Lagrangian and Eulerian formulation. The relations between the true and the observed velocity fields can then be written in the following manner:

$$\boldsymbol{v} = \frac{\partial}{\partial t}\phi(\boldsymbol{X}, t); \quad \nu = \frac{\partial}{\partial t}\varphi(\xi, t); \quad \boldsymbol{V} = \frac{\partial}{\partial t}\psi(\xi, t); \tag{3.28}$$

$$\boldsymbol{v} = \nu - \boldsymbol{F}\boldsymbol{V} \tag{3.29}$$

The Kinetic Energy can then be written as:

$$K_{n,n+1}\left(\boldsymbol{x}_n, \boldsymbol{x}_{n+1}\right) = \frac{\Delta t}{2} \sum_I M_I^{n+1/2} \boldsymbol{v}_{n,n+1}^I \cdot \boldsymbol{v}_{n,n+1}^I \tag{3.30}$$

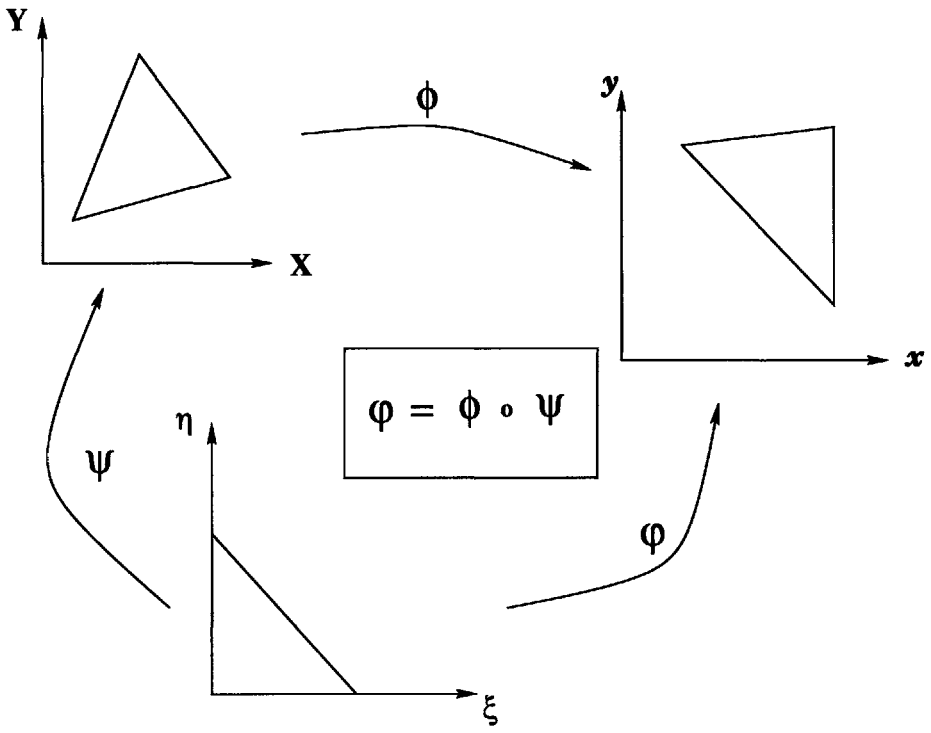

Figure 3-3: Understanding node movement with an intermediate mapping.

where:

$$M_I^{n+1/2} = \frac{1}{2}\left(M_I^n + M_I^{n+1}\right) \tag{3.31}$$

$$\boldsymbol{v}_{n,n+1}^I = \nu_{n+1/2}^I - \boldsymbol{F}_n^I \boldsymbol{V}_{n+1/2}^I \tag{3.32}$$

$$\nu_{n+1/2}^I = \frac{1}{\Delta t}\left(\boldsymbol{x}_{n+1}^I - \boldsymbol{x}_n^I\right) \tag{3.33}$$

$$\boldsymbol{V}_{n+1/2}^I = \frac{1}{\Delta t}\left(\boldsymbol{X}_{n+1}^I - \boldsymbol{X}_n^I\right) \tag{3.34}$$

$$\boldsymbol{F}_n^I = \left(\frac{\int_{V_0} N_I^n \boldsymbol{F}_n dm}{\int_{V_0} N_I^n dm}\right) \tag{3.35}$$

The deformation gradient $\boldsymbol{F}_n$ as used in equation 3.32 is evaluated at time level n in order to make the update explicit. The corresponding equilibrium equations are (for any generic node I, and its neighbouring nodes J):

$$M_I^{n+1/2}\boldsymbol{v}_{n,n+1}^I - M_I^{n-1/2}\boldsymbol{v}_{n-1,n}^I = -\Delta t \boldsymbol{Q}_{n,n+1}^I + \Delta t\left(\boldsymbol{F}_n^I - \boldsymbol{T}_n^I\right) \tag{3.36}$$

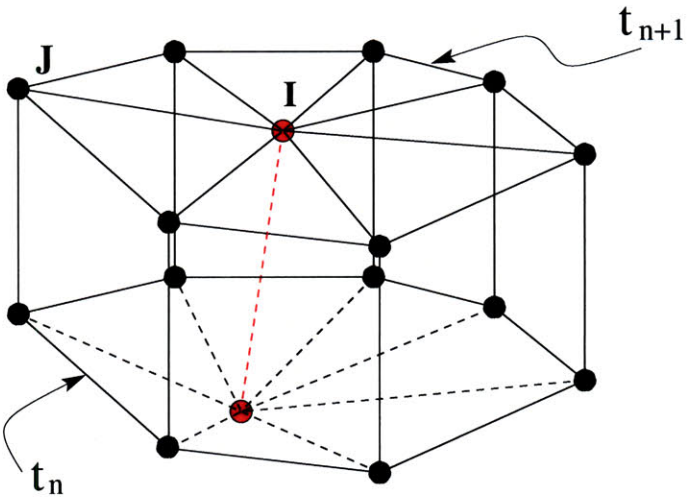

Figure 3-4: Space-time volume for node movement.

where:

$$\boldsymbol{v}^I_{n,n+1} = \frac{1}{\Delta t}\left[\left(\boldsymbol{x}^I_{n+1} - \boldsymbol{x}^I_n\right) - \boldsymbol{F}^I_n\left(\boldsymbol{X}^I_{n+1} - \boldsymbol{X}^I_n\right)\right] \tag{3.37}$$

$$\boldsymbol{Q}^I_{n,n+1} = \sum_J \frac{m^{n+1/2}_J}{m^n_J}\left(\boldsymbol{v}^J_{n,n+1} \otimes \boldsymbol{V}^J_{n,n+1}\right)\int_{V_0} N^n_J \nabla_0 N^n_I dm \tag{3.38}$$

This expression remains explicit if the neighbouring J nodes remain fixed i.e. ($\boldsymbol{V}^J_{n,n+1} = 0$) in which case:

$$\boldsymbol{Q}^I_{n,n+1} = \left(\boldsymbol{v}^I_{n,n+1} \otimes \boldsymbol{V}^I_{n,n+1}\right)\int_{V_0} N^n_I \nabla_0 N^n_I dm = 0$$

Provided that either I is an internal node or V^I remains tangential to the reference boundary Γ_0. Thus for the node to be moved (I) the update step becomes:

$$M^{n+1/2}_I \boldsymbol{v}^I_{n,n+1} - M^{n-1/2}_I \boldsymbol{v}^I_{n-1,n} = \Delta t\left(\boldsymbol{F}^I_n - \boldsymbol{T}^I_n\right) \tag{3.39}$$

And for the neighbouring nodes (J) the update step becomes:

$$M^{n+1/2}_J \boldsymbol{v}^J_{n,n+1} - M^{n-1/2}_J \boldsymbol{v}^J_{n-1,n} = -\Delta t \boldsymbol{Q}^J_{n,n+1} + \Delta t\left(\boldsymbol{F}^J_n - \boldsymbol{T}^J_n\right) \tag{3.40}$$

$$\boldsymbol{Q}^J_{n,n+1} = \left(\boldsymbol{v}^I_{n,n+1} \otimes \boldsymbol{V}^I_{n,n+1}\right)\int_{V_0} N^n_I \nabla_0 N^n_J dm \tag{3.41}$$

The momentum within time step t_n and t_{n+1} is $(D_2 L_{n,n+1})$:

$$\boldsymbol{P}_{n,n+1} = \sum_j \boldsymbol{P}^j_{n,n+1} \tag{3.42}$$

$$\boldsymbol{P}^j_{n,n+1} = M^{n+1/2}_j \boldsymbol{v}^j_{n+1/2} \qquad \forall\, j$$

$$\boldsymbol{H}_{n,n+1} = \sum_j \boldsymbol{x}^j_{n+1} \times \boldsymbol{P}^j_{n,n+1} \tag{3.43}$$

3.4 Edge Collapsing

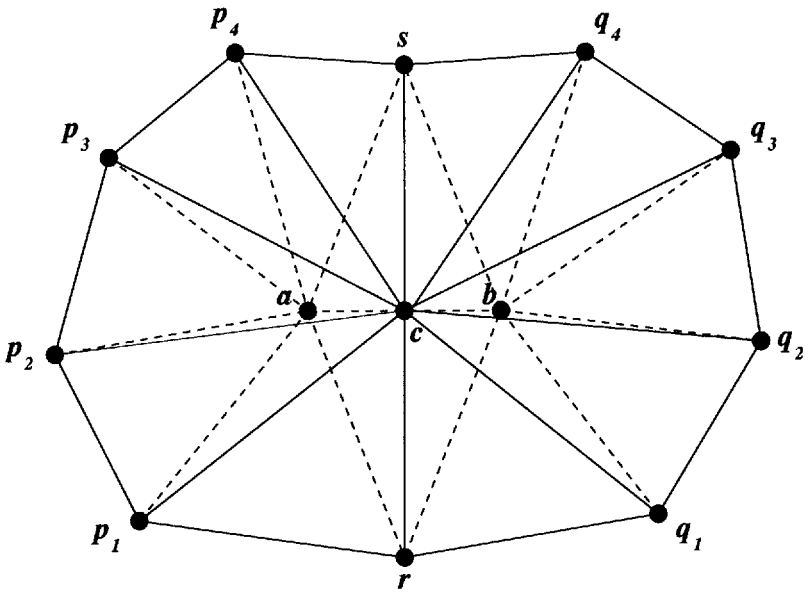

Figure 3-5: Collapsing the edge ab to the point c.

Edge collapsing operation is approached by visualizing a generic patch of elements, as shown in Fig. [3-5]. In the triangular element arb, the edge ab is wished to be collapsed, leading to removal of the triangles arb and abs. The points a and b, belonging to time level n, is substituted by the new point c at time level $n+1$ as shown.

The space-time volume as shown in Fig. [3-6] is the volume over which the Lagrangian is to be computed. To do so, the space-time volume is sub-divided into tetrahedra. There are mainly three types of tetrahedra as shown in Fig. [3-7]. The first type (I) encloses the volume $arbsc$. Then based on the surrounding nodes there are two types of tetrahedra, as shown in Fig. [3-7]. The tetrahedra having a or b as one of the vertices, are labeled type (II) and the ones having c as one of their vertices are labeled type (III). The location of the

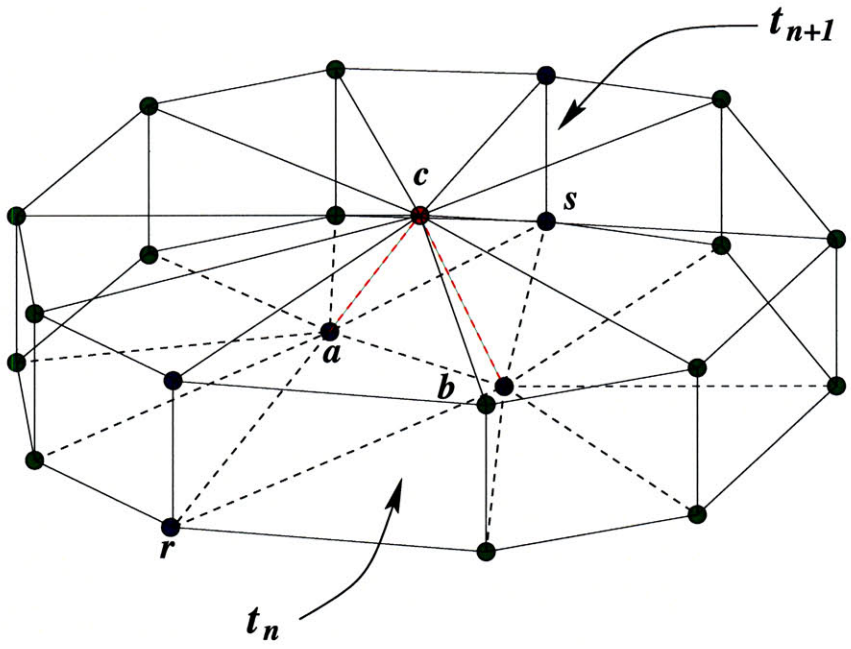

Figure 3-6: The space-time volume for Edge collapsing operation.

new node c is chosen to be a linear interpolation of the locations of nodes a, b and r.

$$\boldsymbol{X}^c_{n+1} = \xi \boldsymbol{X}^a_n + \eta \boldsymbol{X}^b_n + (1-\xi-\eta)\boldsymbol{X}^r_n \tag{3.44}$$

$$\boldsymbol{x}^c_n = \xi \boldsymbol{x}^a_n + \eta \boldsymbol{x}^b_n + (1-\xi-\eta)\boldsymbol{x}^r_n \tag{3.45}$$

The Kinetic Energy Integral and the velocity interpolation within the tetrahedra of type (I) can be written as follows:

$$K^I_{n,n+1} = \frac{\Delta t}{2}\frac{m^n_{ab}}{3}\boldsymbol{v}^c_{n+1/2}\cdot\boldsymbol{v}^c_{n+1/2} \tag{3.46}$$

$$m^n_{ab} = m^n_{arb} + m^n_{abs}$$

$$v^c_{n+1/2} = \frac{\boldsymbol{x}^c_{n+1} - (\xi \boldsymbol{x}^a_n + \eta \boldsymbol{x}^b_n + (1-\xi-\eta)\boldsymbol{x}^r_n)}{\Delta t} \tag{3.47}$$

Similarly the Kinetic Energy Integral and the velocity interpolation within the tetrahedra of type (II) can be written as:

$$K^{II}_{n,n+1} = \frac{\Delta t}{2} m^n_{g_i}\boldsymbol{v}^{g_i}_{n+1/2}\cdot\boldsymbol{v}^{g_i}_{n+1/2} \tag{3.48}$$

$$v^{g_i}_{n+1/2} = \frac{\boldsymbol{x}^{g_i}_{n+1} - \boldsymbol{x}^{g_i}_n}{\Delta t} \tag{3.49}$$

Interior tetrahedra

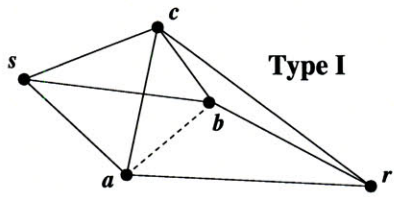

Surrounding tetrahedra

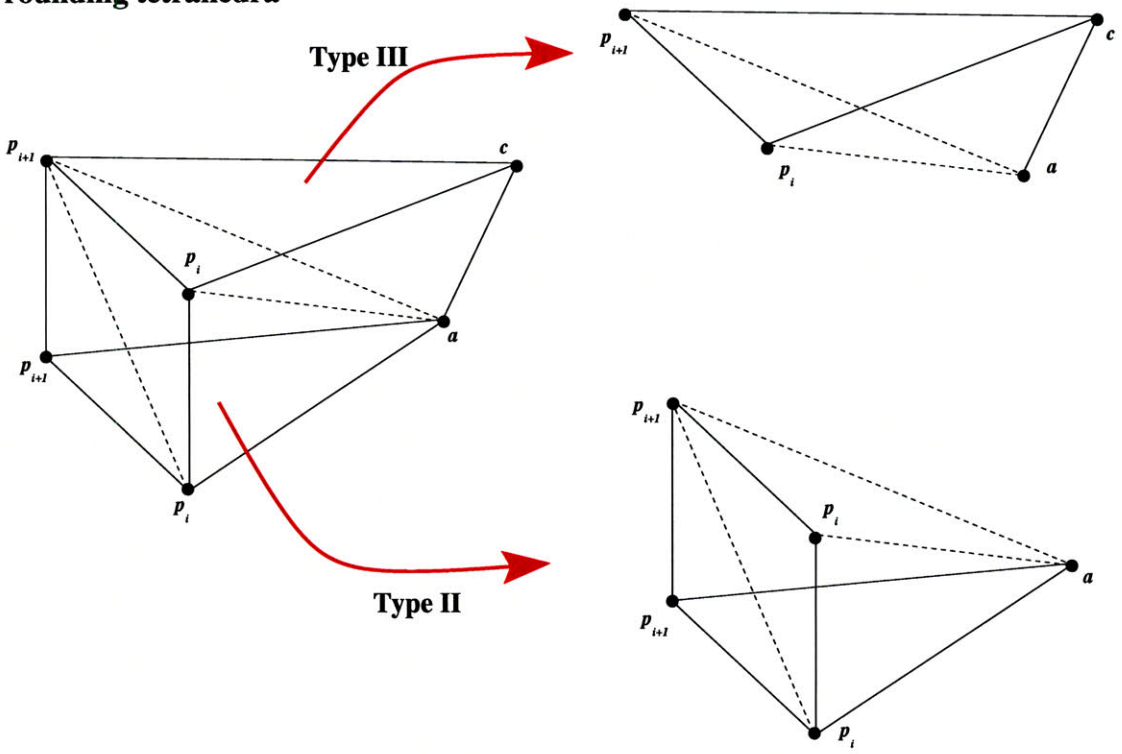

Figure 3-7: The subdivision of the space-time volume into different types of tetrahedra.

where the index g_i is the overall index of all the neighbouring nodes, ordered as $(g_i = r, q_i, s, p_i)$.

The velocity in the tetrahedra of type (III) is not straight forward, since there is no common node in each tetrahedron. Hence the full expression of the velocity (described previously) is used.

$$v_{n+1/2}^{g_i g_{i+1} ac} = \frac{A_{g_{i+1}ac}\boldsymbol{x}_{n+1}^{g_i} + A_{g_i ac}\boldsymbol{x}_{n+1}^{g_{i+1}} + A_{g_i c g_{i+1}}\boldsymbol{x}_{n+1}^{c} - A_{g_i a g_{i+1}}\boldsymbol{x}_{n}^{a}}{6\mathcal{V}_{g_i g_{i+1} ac}} \tag{3.50}$$

$$K_{n,n+1}^{g_i (III)} = m_{g_i g_{i+1} ac}^{n} \boldsymbol{v}_{n+1/2}^{g_i g_{i+1} ac} \cdot \boldsymbol{v}_{n+1/2}^{g_i g_{i+1} ac} \tag{3.51}$$

This makes the algorithm very complex. In order to simplify the algorithm, an approxima-

tion is made. The Kinetic Energy Integral from each of the tetrahedra, of type (III), are added together, and the sum is expressed by the following approximation :

$$\sum_{g_i} K_{n,n+1}^{g_i(III)} = \frac{\Delta t}{2} m_c^{n+1} \boldsymbol{v}_{n+1/2}^* \cdot \boldsymbol{v}_{n+1/2}^* \tag{3.52}$$

$$\boldsymbol{v}_{n+1/2}^* = \frac{1}{\Delta t m_c^{n+1}} \left[m_c^* \boldsymbol{x}_{n+1}^c + \sum_i \Delta m_{g_i} \boldsymbol{x}_{n+1}^{g_i} - m_a^* \boldsymbol{x}_n^a - m_b^* \boldsymbol{x}_n^b \right] \tag{3.53}$$

$$m_c^* = m_c^{n+1} - \frac{m_{ab}^n}{3} \tag{3.54}$$

$$\Delta m_{g_i} = m_{g_i}^{n+1} - m_{g_i}^n \tag{3.55}$$

$$m_a^* = m_a^n - \frac{m_{ab}^n}{3} + M_{arcs} \tag{3.56}$$

$$m_b^* = m_b^n - \frac{m_{ab}^n}{3} + M_{bscr} \tag{3.57}$$

Where M_{arcs} and M_{bscr} are the masses enclosed within *arcs* and *bscr* respectively. Note that Δm_{g_i}, m_a^* and m_b^* can be expressed as linear functions of ξ and η. The velocity $\boldsymbol{v}_{n+1/2}^*$ is a weighted average of the velocities of all the tetrahedra of type III as calculated in equation 3.50 In addition, since the neighbouring nodes are not moved, nor are any neighbouring edge allowed to be collapsed, the mass m_c^{n+1} is known *apriori*. Thus the net Kinetic Energy integral becomes:

$$\begin{aligned} K_{n,n+1} &= K_{n,n+1}^I + K_{n,n+1}^{II} + K_{n,n+1}^{III} \\ &= \frac{\Delta t}{2} \frac{m_{ab}^n}{3} \boldsymbol{v}_{n+1/2}^c \cdot \boldsymbol{v}_{n+1/2}^c + \frac{\Delta t}{2} m_c^{n+1} \boldsymbol{v}_{n+1/2}^* \cdot \boldsymbol{v}_{n+1/2}^* \\ &\quad + \sum_i \frac{\Delta t}{2} m_{g_i}^n \boldsymbol{v}_{n+1/2}^{g_i} \cdot \boldsymbol{v}_{n+1/2}^{g_i} \end{aligned} \tag{3.58}$$

Using stationarity *wrt.* $\boldsymbol{x}_n$, the equilibrium equations obtained at time level n are as follows:

$$(\forall\ g_i \neq r) \qquad m_{g_i}^n\ \boldsymbol{v}_{n+1/2}^{g_i} - m_{g_i}^n\ \boldsymbol{v}_{n-1/2}^{g_i} = \Delta t\ (\boldsymbol{F}_n^{g_i} - \boldsymbol{T}_n^{g_i}) \tag{3.59}$$

$$(1-\xi-\eta)\ \frac{m_{ab}^n}{3}\ \boldsymbol{v}_{n+1/2}^c + m_r^n\ \boldsymbol{v}_{n+1/2}^r - m_r^n\ \boldsymbol{v}_{n-1/2}^r = \Delta t\ (\boldsymbol{F}_n^r - \boldsymbol{T}_n^r) \tag{3.60}$$

$$\xi\ \frac{m_{ab}^n}{3}\ \boldsymbol{v}_{n+1/2}^c + m_a^*\ \boldsymbol{v}_{n+1/2}^* - m_a^n\ \boldsymbol{v}_{n-1/2}^a = \Delta t\ (\boldsymbol{F}_n^a - \boldsymbol{T}_n^a) \tag{3.61}$$

$$\eta\ \frac{m_{ab}^n}{3}\ \boldsymbol{v}_{n+1/2}^c + m_b^*\ \boldsymbol{v}_{n+1/2}^* - m_b^n\ \boldsymbol{v}_{n-1/2}^b = \Delta t\ \left(\boldsymbol{F}_n^b - \boldsymbol{T}_n^b\right) \tag{3.62}$$

Here, a new variable $\boldsymbol{R}_n^j$ is introduced, where

$$(\forall\ j = g_i, a, b) \qquad \boldsymbol{R}_n^j \;=\; m_j^n\ \boldsymbol{v}_{n-1/2}^j + \Delta t\ \left(\boldsymbol{F}_n^j - \boldsymbol{T}_n^j\right) \tag{3.63}$$

Note that $\boldsymbol{R}_n^j$ is known *apriori*. Hence the set of equations, can be rewritten as:

$$(\forall\ g_i \neq r) \qquad m_{g_i}^n\ \boldsymbol{v}_{n+1/2}^{g_i} \;=\; \boldsymbol{R}_n^{g_i} \tag{3.64}$$

$$(1-\xi-\eta)\ \frac{m_{ab}^n}{3}\ \boldsymbol{v}_{n+1/2}^c \;+\; m_r^n\ \boldsymbol{v}_{n+1/2}^r \;=\; \boldsymbol{R}_n^r \tag{3.65}$$

$$\xi\ \frac{m_{ab}^n}{3}\ \boldsymbol{v}_{n+1/2}^c \;+\; m_a^*\ \boldsymbol{v}_{n+1/2}^* \;=\; \boldsymbol{R}_n^a \tag{3.66}$$

$$\eta\ \frac{m_{ab}^n}{3}\ \boldsymbol{v}_{n+1/2}^c \;+\; m_b^*\ \boldsymbol{v}_{n+1/2}^* \;=\; \boldsymbol{R}_n^b \tag{3.67}$$

Note here that Eqn. 3.64 is fully explicit, hence, $\boldsymbol{x}_{n+1}^{g_i}$ for all g_i except r are known. Now revisiting Eqn. 3.53 one can rewrite the expression for $\boldsymbol{v}_{n+1/2}^*$ using Eqn. 3.65 as:

$$\boldsymbol{v}_{n+1/2}^* \;=\; S_m(\xi,\eta)\boldsymbol{v}_{n+1/2}^c + \boldsymbol{W}(\xi,\eta) \tag{3.68}$$

$$\begin{aligned}\boldsymbol{W}(\xi,\eta) \;&=\; \frac{1}{\Delta t m_c^{n+1}}\left[\sum_i \Delta m_{g_i}\boldsymbol{z}_{n+1}^{g_i} - m_a^*\boldsymbol{x}_n^a - m_b^*\boldsymbol{x}_n^b + m_c^*\boldsymbol{x}_n^c + \Delta m_r \boldsymbol{x}_n^r\right] \\ &=\; \boldsymbol{W}_0 + \xi\ \boldsymbol{W}_\xi + \eta\ \boldsymbol{W}_\eta \end{aligned} \tag{3.69}$$

where,

$$\begin{aligned} \boldsymbol{z}_{n+1}^{g_i} \;&=\; \boldsymbol{x}_{n+1}^{g_i} \qquad (\forall\ g_i \neq r) \\ &=\; \frac{\Delta t\ \boldsymbol{R}_n^r}{m_n^r} \qquad (\ g_i = r) \\ S_m(\xi,\eta) \;&=\; \frac{m_{ab}^n}{3m_{n+1}^c m_n^r}\left[\frac{3m_c^* m_n^r}{m_{ab}^n} - (\Delta m_r(1-\xi-\eta))\right] \\ &=\; S_0 + S_\xi^1\xi + S_\eta^1\eta + S_\xi^2\xi^2 + S_\eta^2\eta^2 + S_{\xi\eta}^2\xi\eta \end{aligned} \tag{3.70}$$

Note that the vector coefficients ($\boldsymbol{W}_0$, $\boldsymbol{W}_\xi$, $\boldsymbol{W}_\eta$) and the scalar coefficients ($S_0, S_\xi^1, S_\eta^1, S_\xi^2, S_\eta^2, S_{\xi\eta}^2$) are known *apriori*. Using Eqn. 3.68 in Eqns. 3.66 & 3.67 the two equations are rewritten

as:

$$K_a(\xi,\eta)\ \boldsymbol{v}^c_{n+1/2} + m^*_a(\xi,\eta)\ \boldsymbol{W}(\xi,\eta) = \boldsymbol{R}^a_n \tag{3.71}$$

$$K_b(\xi,\eta)\ \boldsymbol{v}^c_{n+1/2} + m^*_b(\xi,\eta)\ \boldsymbol{W}(\xi,\eta) = \boldsymbol{R}^b_n \tag{3.72}$$

where,

$$K_a(\xi,\eta) = \xi\ \frac{m^n_{ab}}{3} + m^*_a(\xi,\eta)\ S_m(\xi,\eta) \tag{3.73}$$

$$K_b(\xi,\eta) = \eta\ \frac{m^n_{ab}}{3} + m^*_b(\xi,\eta)\ S_m(\xi,\eta) \tag{3.74}$$

Now, eliminating $\boldsymbol{v}^c_{n+1/2}$ from both the above equation, the following equations are obtained:

$$\boldsymbol{v}^c_{n+1/2} = \frac{\boldsymbol{R}^a_n - m^*_a(\xi,\eta)\ \boldsymbol{W}(\xi,\eta)}{K_a(\xi,\eta)} \tag{3.75}$$

$$\boldsymbol{f}(\xi,\eta) \equiv \frac{K_b}{K_a}\left(\boldsymbol{R}^a_n - m^*_a\ \boldsymbol{W}\right) + \left(m^*_b\ \boldsymbol{W} - \boldsymbol{R}^b_n\right) = 0 \tag{3.76}$$

Thus, a simple vector equation (3.76) is obtained, which is used to determine the scalars ξ and η by which, the position of the new node c is determined. This is a coupled quadratic equation which is solved by iteration. A simple Newton iteration leads to quadratic convergence. This leads to the position of the new node ($\boldsymbol{X}^c_{n+1}$) to be a solution of the local equilibrium. Edge ab is collapsed only if the node c lies within the area included by all the surrounding nodes g_i.

Once the position of the node c is obtained, the velocity updates are obtained through simple explicit equations mentioned above (3.75,3.68 and 3.65). The position updates are obtained by the Eqns. 3.47 & 3.49. The momentum conserved in this time-step is of the

form:

$$\boldsymbol{P}_{n,n+1} = \sum_j \boldsymbol{P}^j_{n,n+1} \tag{3.77}$$

$$\boldsymbol{P}^j_{n,n+1} = \begin{cases} m^j_n \boldsymbol{v}^j_{n+1/2} + \Delta m_j \boldsymbol{v}^*_{n+1/2}, & \text{for } j = g_i \\ \frac{1}{3} m^n_{ab} \boldsymbol{v}^j_{n+1/2} + (m^j_{n+1} - \frac{m^n_{ab}}{3}) \boldsymbol{v}^*_{n+1/2}, & \text{for } j = c \end{cases} \tag{3.78}$$

$$\boldsymbol{H}_{n,n+1} = \sum_j \boldsymbol{x}^j_{n+1} \times \boldsymbol{P}^j_{n,n+1} \tag{3.79}$$

Similar to the previous time-step, using stationarity *wrt.* $\boldsymbol{x}_{n+1}$, the equilibrium equations for the next time step t_{n+1} are obtained. The final update equations are:

$$m^{g_i}_{n+1} \boldsymbol{v}^{g_i}_{n+1/2} - m^{g_i}_n \boldsymbol{v}^{g_i}_{n+1/2} - \Delta m_{g_i} \boldsymbol{v}^*_{n+1/2} = \Delta t \, (\boldsymbol{F}^{g_i}_{n+1} - \boldsymbol{T}^{g_i}_{n+1}) \tag{3.80}$$

$$m^c_{n+1} \boldsymbol{v}^c_{n+1/2} - \frac{1}{3} m^n_{ab} \boldsymbol{v}^c_{n+1/2} - (m^c_{n+1} - \frac{m^n_{ab}}{3}) \boldsymbol{v}^*_{n+1/2} = \Delta t \, (\boldsymbol{F}^c_{n+1} - \boldsymbol{T}^c_{n+1}) \tag{3.81}$$

3.5 Implementation

With the mesh adaptation procedures, explained, so far, an effective mesh-adaptive solver can be implemented which is momentum conserving. In order to develop a mesh adaptive solver, a suitable mesh adaptation, criteria based on error estimates was used. In this section details of mesh adaptation criteria and other implementation details are presented.

3.5.1 Error Estimate

There are various error estimates used in the literature based on gradients or functional outputs or from residues or from constitutive relations. Due to the local mesh operations, described in the previous section, a particular gradient-type error estimate was used, based on a recovered solution in a local patch. The error-estimate described by Zienkiewicz and Zhu,[46, 47]y commonly known as Z^2 error-estimate was used. This error estimate, although described for linear material properties has been extended for non-linear materials, and has been found quite effective in the present genre of problems.

To begin with the description of the error-estimate, the computed solution on an 'h'

level grid can be written as:

$$\boldsymbol{x}_h = \boldsymbol{N}\hat{\boldsymbol{x}} \tag{3.82}$$

where $\hat{\boldsymbol{x}}$ are the nodal positions vectors and $\boldsymbol{N}$ are the shape functions. The stresses in the elements can then be computed from the the position vectors through a non-linear relation as:

$$\boldsymbol{\sigma}_h = \boldsymbol{\sigma}(\boldsymbol{x}_h) \tag{3.83}$$

This stress $\boldsymbol{\sigma}_h$, is the stress tensor, at each element. From this stress, the Z^2 error suggests, a recovered stress, such that:

$$\boldsymbol{\sigma}^* = \boldsymbol{N}\hat{\boldsymbol{\sigma}^*} \tag{3.84}$$

where $\hat{\boldsymbol{\sigma}^*}$ are nodal values of the stresses, which satisfy:

$$\int_\Omega \boldsymbol{N}^T \left(\boldsymbol{\sigma}^* - \boldsymbol{\sigma}_h\right) d\Omega = 0 \tag{3.85}$$

which leads to a simple evaluation of $\hat{\boldsymbol{\sigma}}^*$ as follows:

$$\hat{\boldsymbol{\sigma}}^* = \frac{\int_\Omega \boldsymbol{N}^T \boldsymbol{\sigma}_h d\Omega}{\int_\Omega \boldsymbol{N}^T \boldsymbol{N} d\Omega} \tag{3.86}$$

Note here that the stresses can be recovered at each element from the above relation, in case of linear triangular elements, as:

$$\hat{\boldsymbol{\sigma}}_a^* = \frac{\sum_{e \in a} \boldsymbol{\sigma}_h^e A_e}{\sum_{e \in a} A_e} \tag{3.87}$$

$$\boldsymbol{\sigma}_e^* = \boldsymbol{N}_a^e \hat{\boldsymbol{\sigma}}_a^* \tag{3.88}$$

This involves lumping of the $\int_\Omega \boldsymbol{N}^T \boldsymbol{N} d\Omega$ matrix in the denominator. Now from this recovered stress at each element, an error-norm is suggested, to get a measure of a local and the

global norm.

$$\|\bar{e}\|^{\mathrm{R}} = \left\{ \sum_{e=1}^{N} \left(\|e\|_e^{\mathrm{R}} \right)^2 \right\}^{1/2} \tag{3.89}$$

$$\|e\|_e^{\mathrm{R}} = \left\{ \int_{\Omega_e} (\boldsymbol{\sigma}^* - \boldsymbol{\sigma}_h) : (\boldsymbol{\sigma}^* - \boldsymbol{\sigma}_h) \, d\Omega \right\}^{1/2} \tag{3.90}$$

It has been shown in the papers by Zienkiewicz and Zhu [46, 47] that such a recovered stress has super-convergence with mesh size, and the error-estimate shown above has quadratic convergence with mesh size. In those works, examples were chosen from linear problems, where as the present research involves non-linear problems. In addition, due to the lumping of the $\int_\Omega \boldsymbol{N}^T \boldsymbol{N} d\Omega$ matrix, the super-convergence of the recovered stresses with mesh size is also not guaranteed. Hence to test the behaviour of the error-estimate, a punch problem was used as a test case. The unit thickness square plate with material properties ($E = 1.7 \times 10^7\,\mathrm{Pa}$, $\nu = 0.450$ and $\rho = 1.1 \times 10^3\,\mathrm{kg/m^3}$), and the applied punch velocity $v_{\mathrm{punch}} = 2\mathrm{m/s}$., was chosen, as shown in figure 3-8. For a uniform mesh, error growth and instantaneous

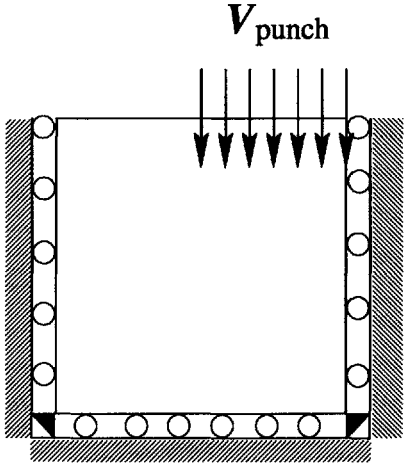

Figure 3-8: A schematic of the punch test case.

error behaviour was studied. Figures (3-9,3-10 and 3-11) we see that such local errors do predict the sensitive regions of the solutions, which in this case is a corner where stress concentration takes place. To study the behaviour of the global norm in a dynamic sense, the error growth is studied as shown in figure 3-12: Error studied at a time instant *wrt.* different mesh size, is shown in the next figure 3-13, where in, quadratic convergence in error-

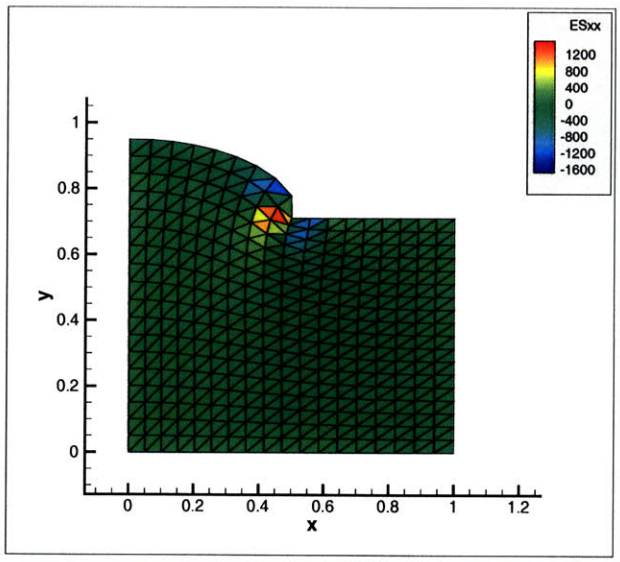

Figure 3-9: Error in stresses $\boldsymbol{\sigma}_{xx}$.

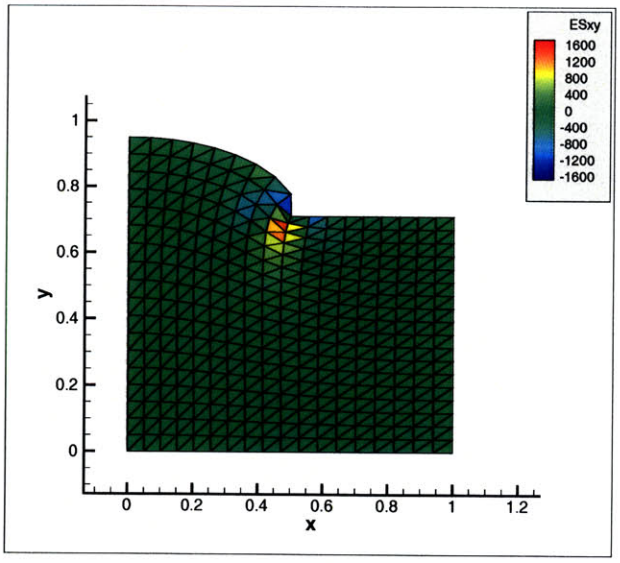

Figure 3-10: Error in stress $\boldsymbol{\sigma}_{xy}$.

estimate is shown. This was in agreement to the observations described by Zienkiewicz and Zhu [46, 47], even in the case of non-linear problems.

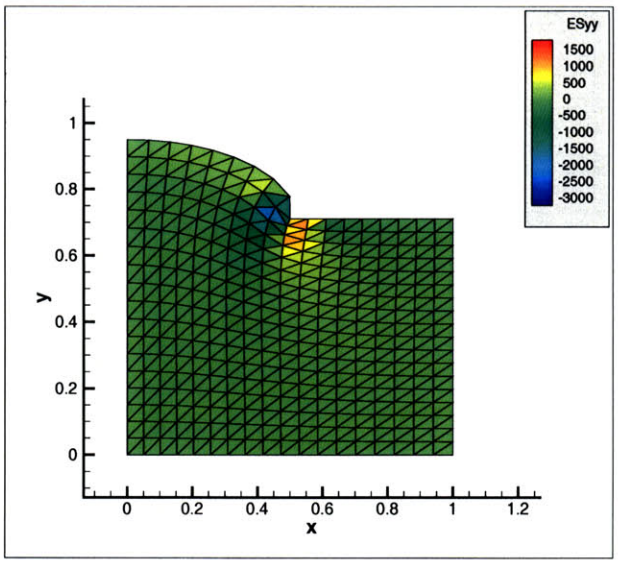

Figure 3-11: Error in stress $\boldsymbol{\sigma}_{yy}$.

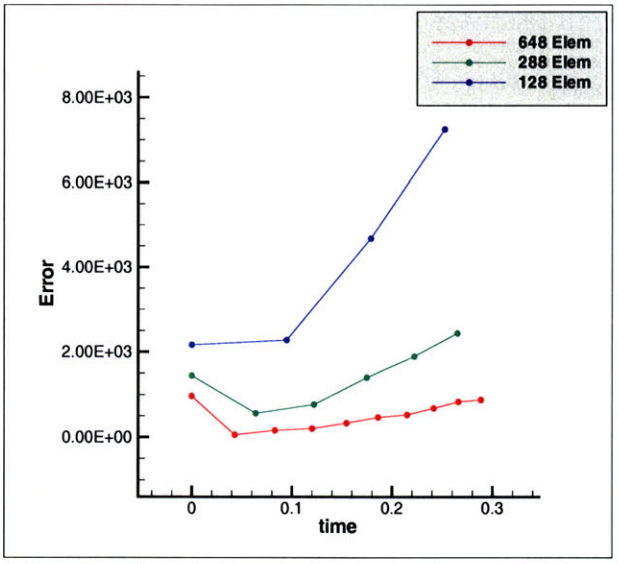

Figure 3-12: Error norm in stress $\|\bar{e}\|^{\mathrm{R}}$ at different instants in time for different mesh size.

3.5.2 Adaptation Criteria

Based on the Z^2 Error-Estimate, a simple adaptation criteria is implemented. We define a scalar θ^R as:

$$\theta_e^R = \frac{\|e\|_e^R}{\|\bar{e}\|^R} \tag{3.91}$$

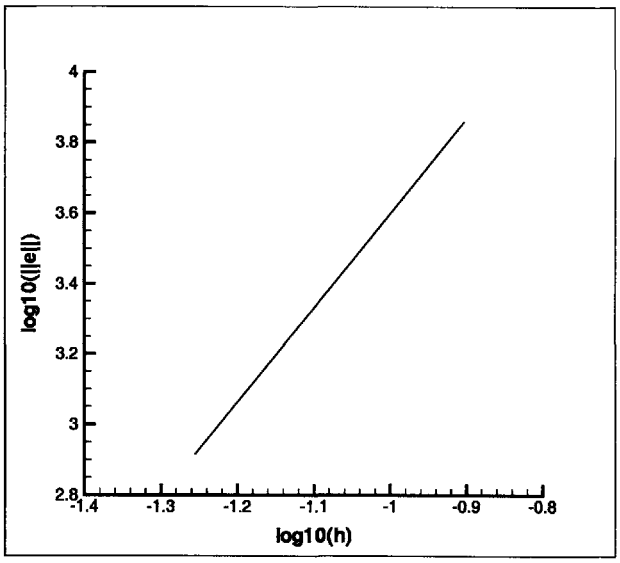

Figure 3-13: Mesh size dependence of Error norm in stress $\|\bar{\sigma}\|^{\mathrm{R}}$

And then elements with relatively higher values of theta were chosen for adaptation, typically ($\forall e\ \theta_e^R > C\theta_{e\,\max}^R$), where C was an input parameter typically chosen in the range ($0.5 < C < 1.0$).

Once the element was chosen, the edge length ratios (η_i) were obtained by $\left(\eta_i = \frac{2l_i}{\sum_j l_j}\right)$, where l_i is the length of the i^{th} edge, which varied from 0 to 1. Edge length ratio, close to zero or one, indicated mesh-skewness, which were collapsed or split or swapped. Edges with edge ratios close to 0 say ($\eta_i < 0.3$), were collapsed. Edges with edge ratios closer to 1 say ($\eta_i > 0.7$) or higher were swapped or split. In case of node movement, a local patch of nodes were considered, and the average (centroid) and the deviation of the node from the average was calculated. For higher deviation values, the node was moved towards the centroid.

The adaptation sequence used for all the operations, has been simple. Most mesh adaptation involved two timesteps ($t_n \rightarrow t_{n+1}$) and ($t_{n+1} \rightarrow t_{n+2}$). Only one operation was attempted within each pair of timesteps. Adaptation was attempted after constant intervals (number of time-steps). Diagonal swapping, node movement, edge-splitting and edge-collapsing were attempted in this sequence at every subsequent (or alternate) timestep pair. Depending on the need, the lowest (finest) hierarchical level of the grid was prescribed, in order to prevent over-refinement. The zero'th hierarchical level elements were not removed,

in order to prevent over-coarsening.

Now some examples using mesh adaptation procedures described so far, are presented in the next section.

3.6 Mesh Adaptation Examples

3.6.1 Spinning Plate

A unit thickness square plate, spinning without any constraint, was considered as a test case to illustrate the conservation properties of the proposed mesh adaptation procedures. The plate was made out of nearly incompressible rubber material with material properties, *viz.*, Youngs Modulus $E = 1.7 \times 10^7$ Pa, Poisson's ratio $\nu = 0.45$ and density $\rho = 1.1 \times 10^3$ kg/m^3. The plate rotated at 1000 RPM. The plate was meshed with 200 equal linear triangular elements as shown in Figure 3-14 (left) which also shows the pressure distribution at a given instant (right). The simulation was conducted using a mesh-adaptive solver, using all the above mentioned, adaptation procedures *viz.*, diagonal swapping, node movement, edge-splitting and edge collapsing. A simple mesh adaptation criteria based on the the mesh edge skewness and elemental stress was used. Figure 3-14, demonstrates how the mesh was refined where the mesh skewness and stresses were relatively larger. The center of mass was

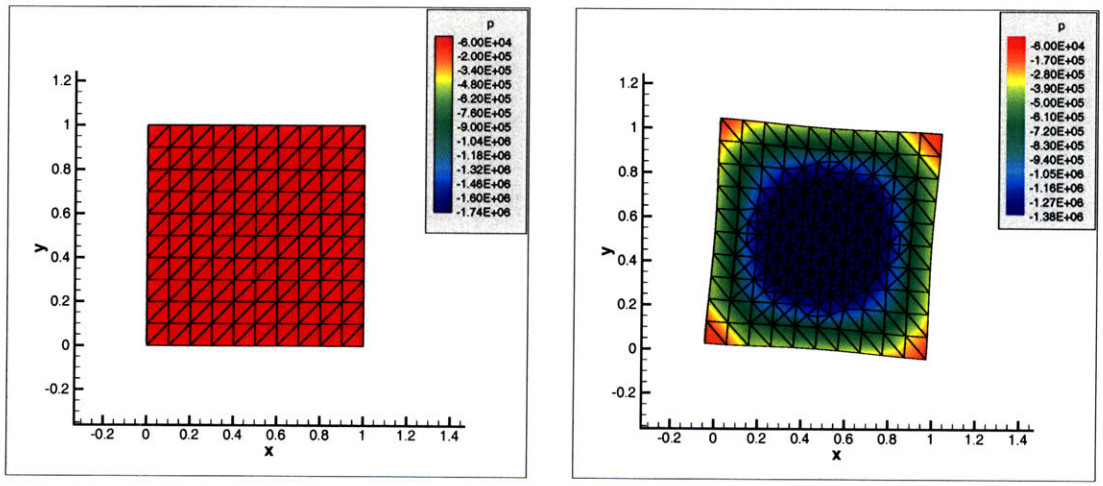

Figure 3-14: A Spinning plate simulation with adaptation.

initially at $\boldsymbol{X} = 0.5$, $\boldsymbol{Y} = 0.5$, and as a consequence of conservation of linear momentum $\boldsymbol{P}_{n,n+1}$, the center of mass would be expected to remain at the same location. Although due

to node movement, some minor fluctuation in the center of mass location could be expected. The angular momentum $\boldsymbol{H}_{n,n+1}$ would also be expected to remain constant during the time integration.

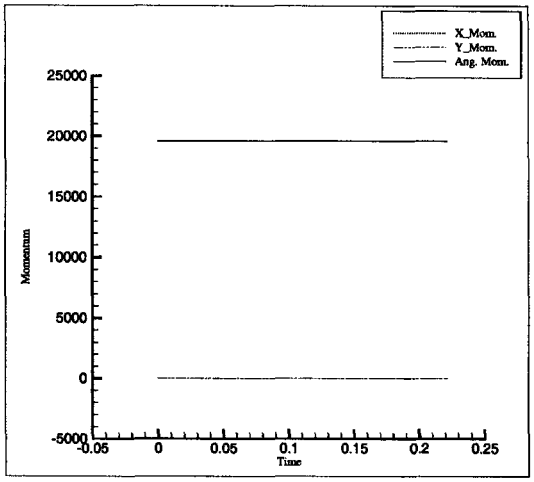

Figure 3-15: Linear and angular momentum history

As expected, the momentum remains conserved exactly, throughout the simulation as shown in Figure 3-15. The momentum calculated in each step was based on the $\boldsymbol{P}_{n,n+1}$ and $\boldsymbol{H}_{n,n+1}$ expressions described in each of of the adaptation procedures previously. There

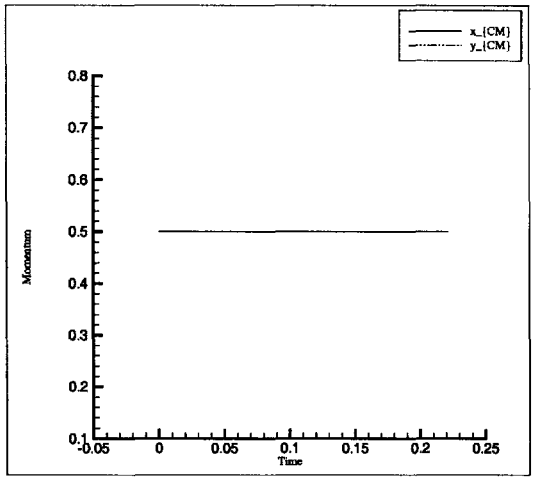

Figure 3-16: Location of center of mass.

was no noticeable change in the center of mass, as shown in Figure 3-16, which was also expected. Figure 3-17 shows the energy history during the simulation. Although there are slight fluctuations in the energy behaviour, initially, but with time, the energy remains more or less bounded, with no significant rise or dissipation as shown in Figure 3-17.

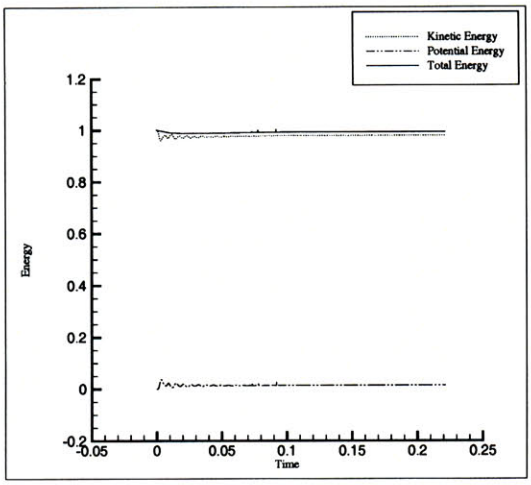

Figure 3-17: Energy history.

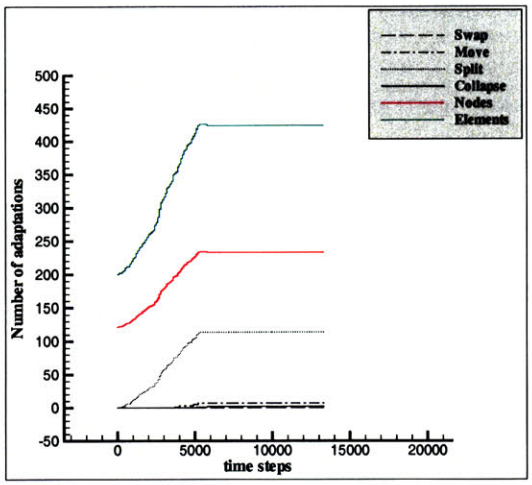

Figure 3-18: Mesh Adaptation history.

Figure 3-18, shows the adaptation history, with the number of operations conducted and the total number of nodes and elements during the course of adaptation.

3.6.2 An oscillating ring

A unit thickness circular ring, made up of nearly incompressible material ($E = 1.0\,\text{Pa}$, $\nu = 0.450$ and $\rho = 1.0\,\text{kg/m}^3$) is initially stretched and let to oscillate freely. This was chosen as another test case to study the momentum behaviour under large stretching and free oscillation. The ring was meshed using 576 triangular elements initially. At $t = 0$, the mesh is deformed as shown in Figure 3-19. The ring is let free to oscillate there after. Time integration was performed using the mesh-adaptative procedures, using only diagonal

swapping and node movement. The purpose, here was to address mesh-skewness, and hence no refinement and coarsening was conducted.

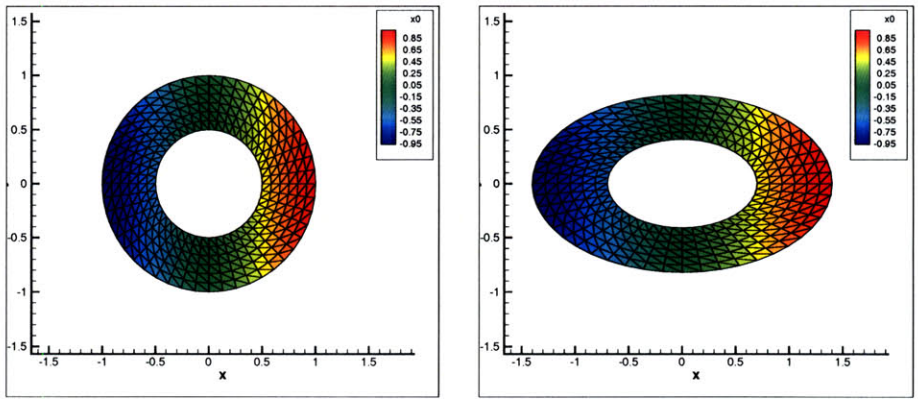

Figure 3-19: A circular ring(left) is initially stretched(right) and let to oscillate freely.

Figure 3-20 shows two arbitrary instances of the ring demonstrating multiple wave modes. Node movement can not be seen in the spatial configuration, but diagonal swaps can be clearly seen. Also to be noticed is that the ring remains centered at the same point Mesh adaptation was based on mesh skewness.

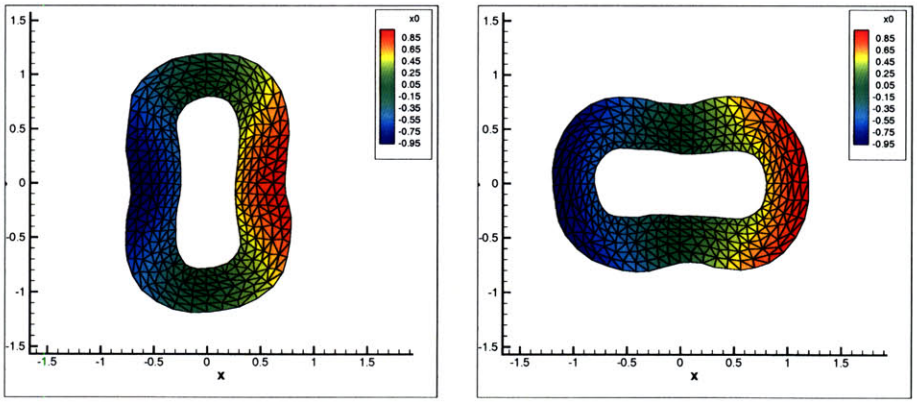

Figure 3-20: Deformation at intermediate step with adaptation.

Figure 3-21 demonstrates conservation of linear and angular momentum.

3.6.3 A Tensile test case

Next, a tensile test case is presented. This test case was chosen to observe the momentum behaviour in presence of external forces. In order to demonstrate the exact conservation of linear and angular momentum, a modified measure of momentum is calculated.

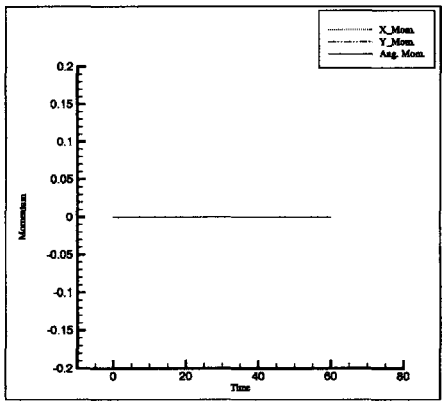

Figure 3-21: The momentum history for the oscillating ring.

Modified Momentum

The measure of the modified momentum can be computed from the basic idea of measuring the momentum, in absence of external forces. Subtracting the effects of external forces from the actual momentum, the following measure is devised.

$$\boldsymbol{P}'_{n,n+1} = \boldsymbol{P}_{n,n+1} - \sum_{0}^{n} \left[\left(\int_{V_0} \rho_0 \boldsymbol{g}_n dV_0 \right) + \sum_{a \in \Gamma} \boldsymbol{R}^a_{n+1} \right] \Delta t_n \tag{3.92}$$

$$\boldsymbol{H}'_{n,n+1} = \boldsymbol{H}_{n,n+1} - \sum_{0}^{n} \left[\left(\int_{V_0} \rho_0 \boldsymbol{x}_n \times \boldsymbol{g}_n dV_0 \right) + \sum_{a \in \Gamma} \boldsymbol{x}_n \times \boldsymbol{R}^a_{n+1} \right] \Delta t_n \tag{3.93}$$

Where $\boldsymbol{g}_n$ is the external acceleration, (say gravity etc.), and is computed, like the external forces are computed, (actually external force vector could also be used), while the external nodal forces, $\boldsymbol{R}^a_{n+1}$ can be obtained while applying the boundary conditions. The modified momentum thus obtained is expected to remain conserved, in spite of presence of external forces.

In the Figure 3-22 a square steel plate, with material properties ($E = 2.1 \times 10^{10}\,\text{Pa}$, $\nu = 0.3$ and $\rho = 7 \times 10^3\,\text{kg/m}^3$) is pulled rapidly by $\boldsymbol{v}_{\text{pull}} = 40m/s$ at its top surface, and reaches thrice its length within 0.05seconds.

Mesh adaptation was employed in the simulation, and the net momentum was conserved as is shown in Figure 3-23.

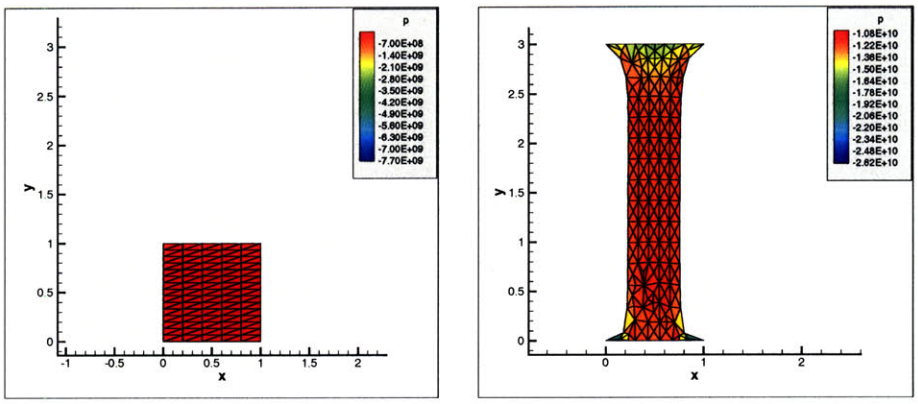

Figure 3-22: A Tensile test specimen (left) pulled to thrice its length (right).

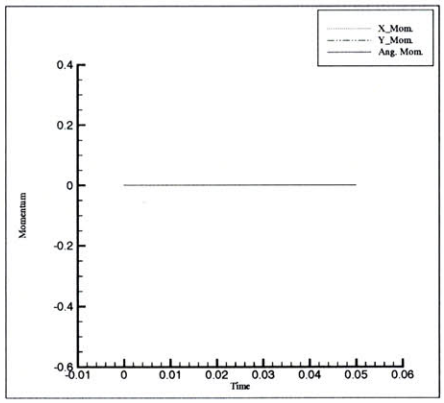

Figure 3-23: The Modified Momentum history for the Tensile test

3.6.4 A Punch test

Similar to the tensile test case another test case as that of a punching problem was considered. A flat square plate of unit length was constrained from the bottom and sides and punched into the top half with a prescribed punch velocity ($v_{\text{punch}} = 2$ m/s) as shown in Figure 3-24. Here a nearly incompressible rubber plate was chosen with material properties, ($E = 1.7 \times 10^7$ Pa, $\nu = 0.450$ and $\rho = 1.1 \times 10^3$ kg/m^3). The deformed configuration at $t = 0.25$s is shown in Figure 3-25.

The Modified momentum remains conserved as shown in the figure 3-26.

3.6.5 Plate Impact

In this example a plate impacting a rigid wall is shown. The Taylor Bar impact (TBI) is a standard benchmark in rapid dynamics problems involving large deformations. The

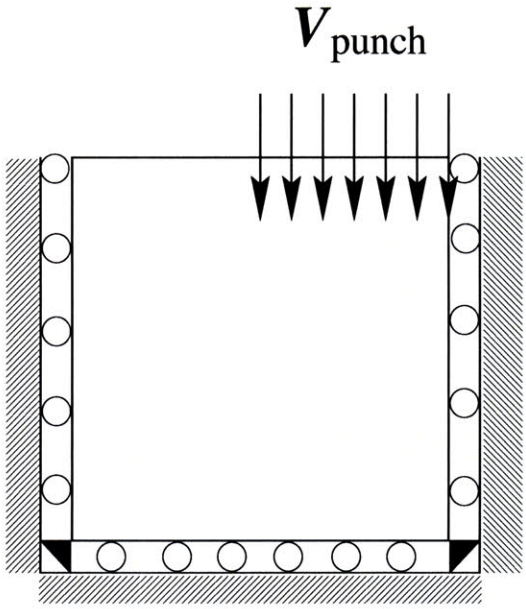

Figure 3-24: A schematic figure of the punch test case, showing boundary conditions.

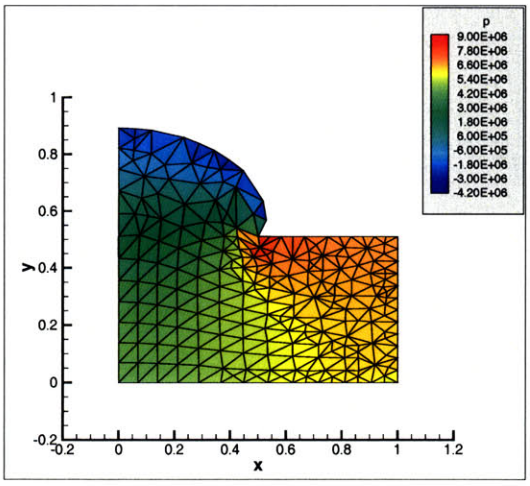

Figure 3-25: Mesh adaptation for a punch problem.

standard TBI problem involves plastic deformations of a rod, impacting a rigid wall. In this case a plate impacting a rigid wall is considered. Since only hyperelastic materials have been considered in this thesis, a modified TBI problem is presented where the constitutive relations are based on hyperelastic behaviour.

In this case, a plate of length $L = 32.4$mm and width $w = 6.4$mm impacts the rigid wall with a velocity of 227m/s. Using symmetry, only half of the plate is considered with appropriate boundary conditions, as shown in figure 3-27 The material properties of the plate were ($E = 5.85 \times 10^8$ Pa, $\nu = 0.495$, $\rho = 8930$ kg/m^3). The plate was discretized

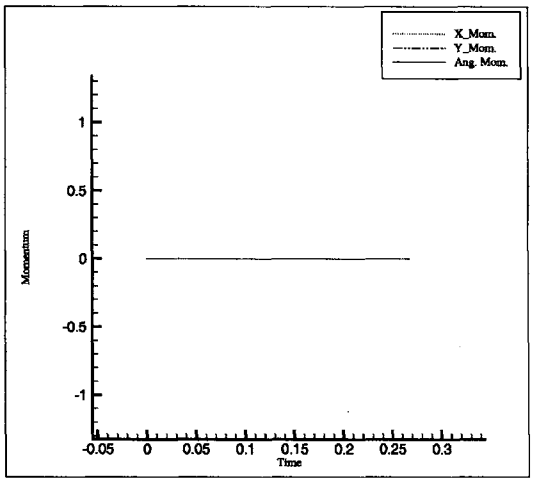

Figure 3-26: The Modified Momentum history for the punch Problem

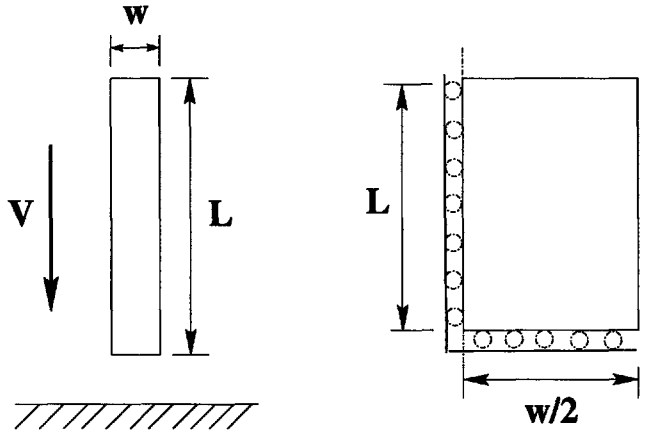

Figure 3-27: Schematic diagram of the plate impact problem.

using 200 elements and the solution was computed for 194μs. Figures 3-28 to 3-31 show the solution of the deformed plate at various time instants. The mesh gets refined in the regions of high error (Z^2 error) and high mesh skewness. Figure 3-31 shows adaptation near the contact where the mesh undergoes the most skewness. The plate touches the the wall at 14 μs. In figure 3-28 the plate is shown to collide with the rigid wall within the first 30 μs where the body distorts at the contact of the wall. With further motion untill 60 μs, the mesh distorts inside, where the mesh is adapted. All the kinetic energy of the plate is almost converted to internal potential energy by 90 μs as shown in figure 3-33 and 3-29. After 120 μs the plate springs back in the opposite direction (reaction). The plate springs back untill 150 μs, where it undergoes large necking type of deformation, where meshes are adapted as shown in figure 3-30. At roughly 180 μs, the plate leaves the rigid

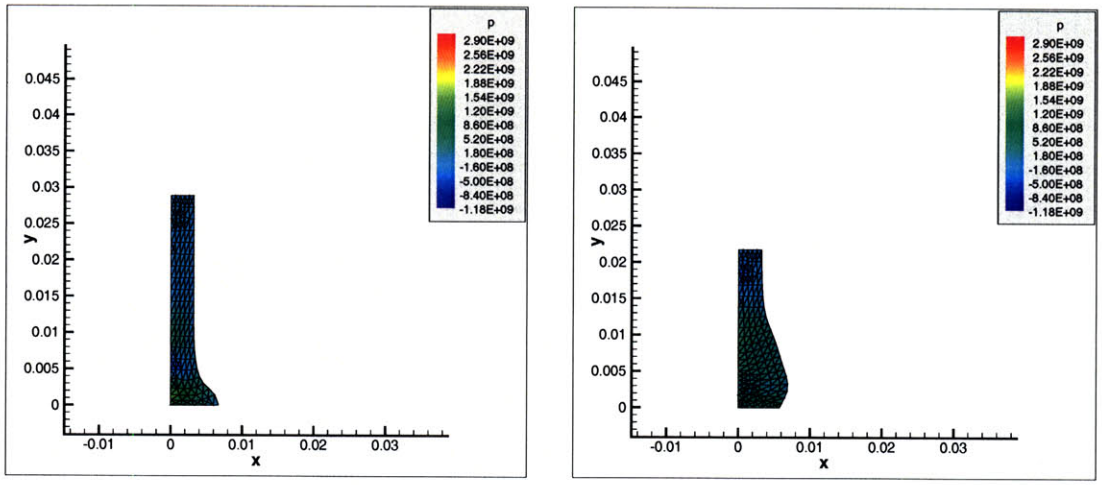

Figure 3-28: The plate at $t = 30\,\mu$s (left) and $t = 60\,\mu$s (right).

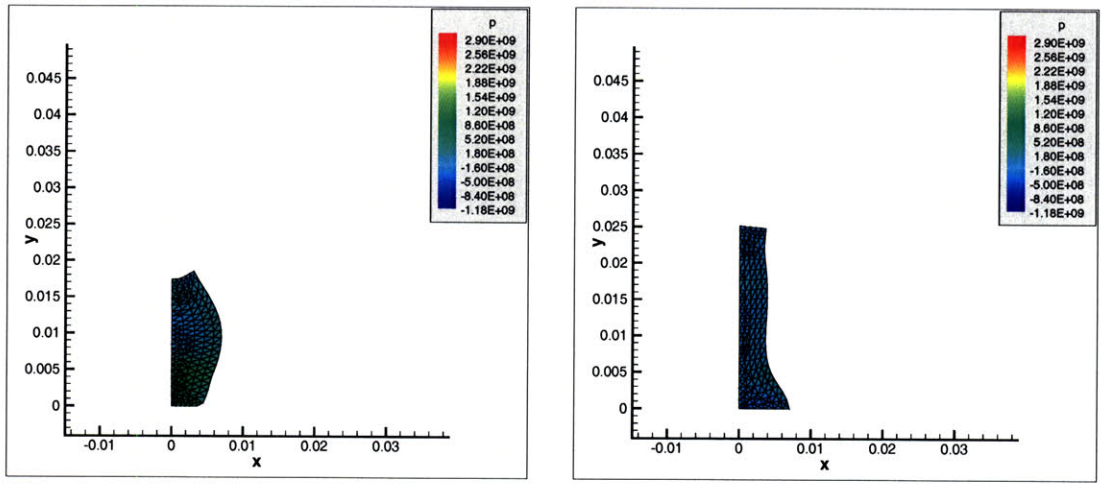

Figure 3-29: The plate at $t = 90\,\mu$s (left) and $t = 120\,\mu$s (right).

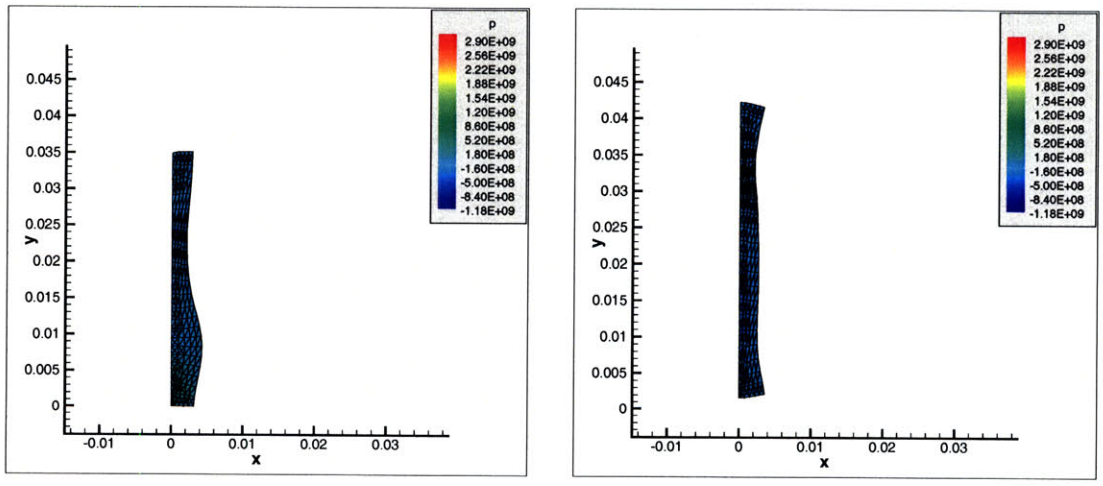

Figure 3-30: The plate at $t = 150\,\mu$s (left) and $t = 180\,\mu$s (right).

wall (bounce-off motion).

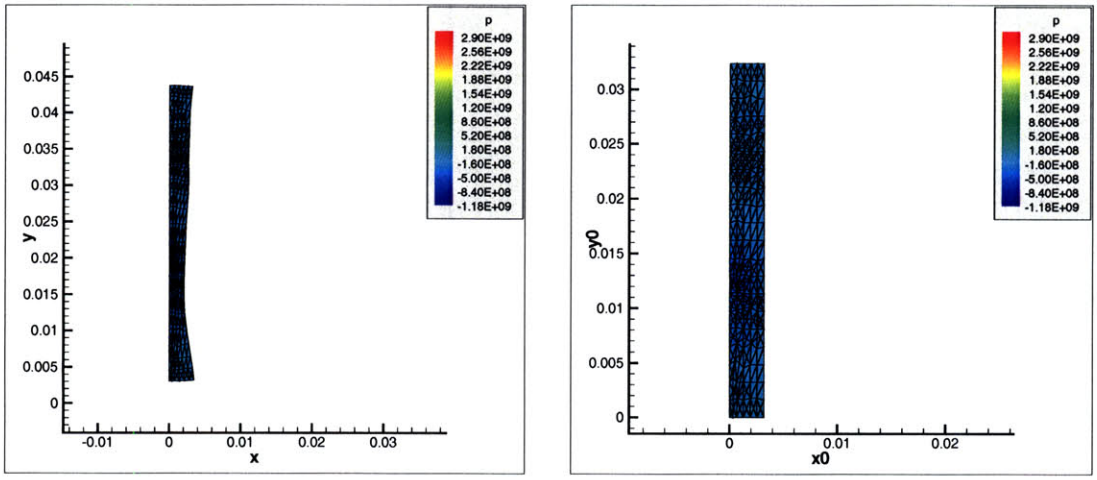

Figure 3-31: Deformed configuration of the plate at $t = 194\,\mu$s (left) and the corresponding mesh in the reference configuration (right).

The modified momentum in this case remained constant, as shown in figure 3-32.

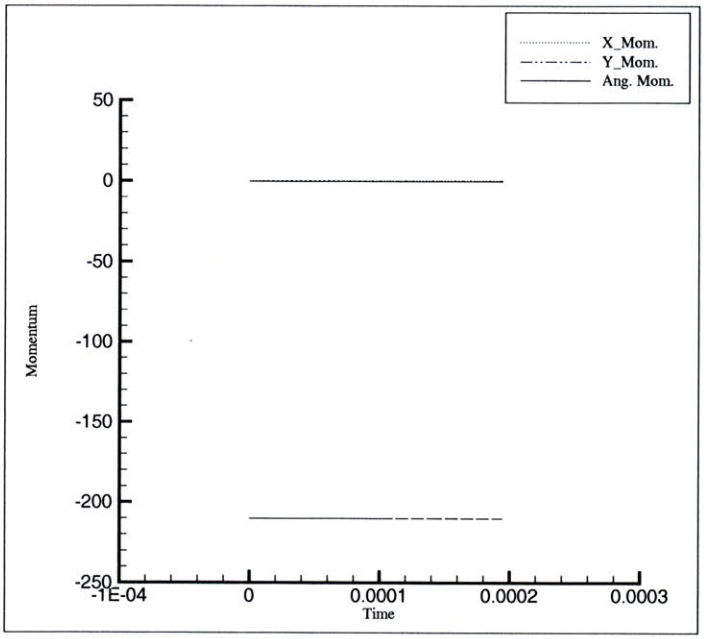

Figure 3-32: Modified Momentum history of the plate

Figure 3-33 shows the energy history. The energy has a slight decay over time due to viscous stabilization. The remeshing operations introduce small energy spikes, which are stabilized.

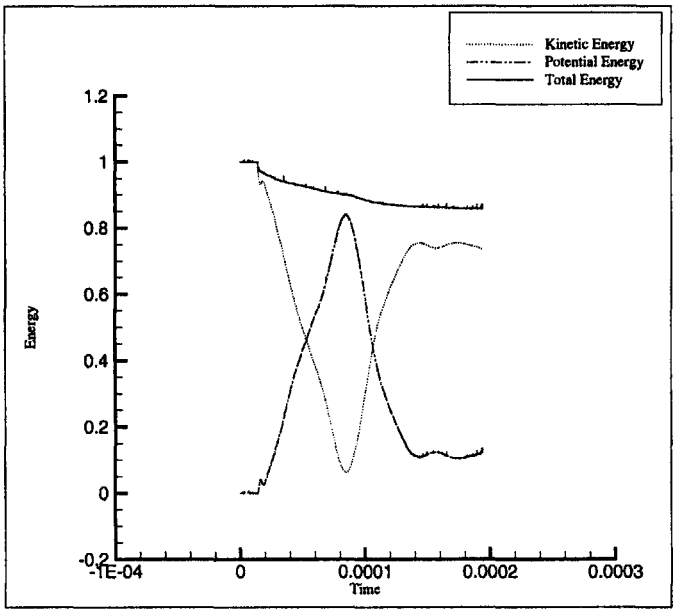

Figure 3-33: The Energy history.

3.7 Concluding Remarks

In this chapter variationally consistent time updates for local topological changes have been developed. The methods have been formulated using the space-time discretization described in chapter 2. These updates have been implemented in tandem to develop a simple mesh adaptation algorithm. A simple mesh adaptive criteria based on the Z^2 error-estimate has been used. The mesh adaptation algorithm thus obtained, is shown to conserve linear and angular momentum. In cases of external forces, a modified momentum is used to demonstrate the conservation of momentum. Simple cases of rapid dynamics have been shown to demonstrate the application of such methods. The existing adaptive procedures are explicit, and cause no significant extra expense over the standard explicit (central difference) scheme. Clearly, further work is required to augment the use of the algorithm to more complicated problems, where severe mesh distortions are encountered. Better mesh adaptation criteria would be required, to make the adaptation more effective.

Chapter 4

The Fractional time-step method

4.1 The Mixed Formulation

The internal potential energy depends on the constitutive relations of the materials in the system. In this research hyperelastic Neo-Hookean materials, undergoing large deformations and displacements, have been considered. The internal potential energy has been expressed in terms of displacements in chapter 2.

The expression for internal potential energy (Eqn. 2.4) is well suited for compressible or nearly incompressible materials. However, when the material approaches incompressibility, the bulk modulus, κ, becomes very large and this causes $\Pi_{\text{int}}(\mathbf{x})$, in (2.4), to be unbounded for all motions not satisfying $J = 1$. This is a constraint on the allowable deformations which, in practice, is difficult to enforce a priori. A more suitable formulation which permits computation of general motions is obtained by introducing the constraint, $J = 1$, through a Lagrange multiplier. It turns out that, it is actually possible to reformulate the internal potential energy, by introducing an additional pressure variable in such a manner that a formulation which is valid for both compressible and incompressible materials is obtained. This is generally referred to as the mixed formulation which uses pressure as a separate degree of freedom. In the compressible case, the pressure can be determined from the volumetric change as $p = \kappa(J-1)$, whereas in the incompressible limit, the pressure becomes a Lagrange multiplier and thus a separate variable, which enforces $J = 1$. The mixed

formulation can be written as:

$$\Pi_{\text{int}}(\mathbf{x}, p) = \Pi_{\text{iso}}(\mathbf{x}) + \Pi_{\text{vol}}(\mathbf{x}, p) , \tag{4.1}$$

where,

$$\Pi_{\text{iso}}(\mathbf{x}) = \int_{V_0} \frac{\mu}{2}(tr(\hat{\mathbf{C}}) - 3)dV_0 , \tag{4.2}$$

and,

$$\Pi_{\text{vol}}(\mathbf{x}, p) = \int_{V_0} p(J-1)dV_0 - \int_{V_0} \frac{p^2}{2\kappa}dV_0 . \tag{4.3}$$

For compressible materials, the constitutive equation relating the volumetric changes and the pressure is recovered by setting the variation of Π_{vol} with respect to p equal to zero. Thus the form (4.1-4.3) of the internal potential function, has the property that it is equivalent to the irreducible form (2.4), but as the material becomes incompressible, the second term in Π_{vol} disappears and only the constraint times the Lagrange multiplier, p, remains. As expected, for incompressible materials, $\Pi_{\text{vol}} \rightarrow 0$, and $\Pi_{\text{iso}} \rightarrow \Pi_{\text{int}}$. It is clear that when the form (4.1-4.3), is adopted, for the internal potential energy, the Lagrangian will also depend on the pressure, that is $\mathcal{L}(\mathbf{x}, \dot{\mathbf{x}}, p)$, and that the solution will need to be determined by requiring stationarity of the action integral, (2.2), with respect to $\mathbf{x}$ and p.

4.2 Fractional Step Variational Formulation

Here, the time integration algorithms, introduced in the previous section, is extended to the case in which the volumetric internal potential energy, and in turn the Lagrangian, is expressed in terms of the configuration $\mathbf{x}$, and the pressure, p, as given by equations (4.1-4.3).

Consider the following discrete Lagrangian between any two steps n and $n+1$,

$$L_{n,n+1}(\mathbf{x}_n, \mathbf{x}_{n+1}, p_{n+\frac{1}{2}}) = \frac{\Delta t}{2} M(\mathbf{v}_{n+1/2}, \mathbf{v}_{n+1/2}) - \Delta t\, \Pi_{\text{iso}}(\mathbf{x}_n) - \Delta t \Pi_{\text{ext}}(\mathbf{x}_n) \\ -\Delta t \int_{V_0} \frac{1}{2} p_{n+1/2}(J_{n+1} + J_n - 2)\, dV_0 + \Delta t \int_{V_0} \frac{p_{n+1/2}^2}{2\kappa}\, dV_0 \tag{4.4}$$

Note that a central difference approximation for the volumetric components has been used and that the pressure has been chosen to be evaluated at the half step. The stationary conditions of the action integral with respect to position at step n can now be obtained with the help of the expression $DJ[\delta\mathbf{v}] = J\text{div}\delta\mathbf{v}$, which leads to,

$$M\left(\delta\mathbf{v}_n, \frac{\mathbf{v}_{n+1/2} - \mathbf{v}_{n-1/2}}{\Delta t}\right) = F(\delta\mathbf{v}_n; \mathbf{x}_n) - T'(\delta\mathbf{v}_n; \mathbf{x}_n) - \int_{V_n} \frac{1}{2}(p_{n-1/2} + p_{n+1/2})\text{div}\delta\mathbf{v}_n\, dV_n \tag{4.5}$$

where $T'(\delta\mathbf{v}; \mathbf{x}) = D\Pi_{\text{iso}}(\mathbf{x}_n)[\delta\mathbf{v}]$ represents the isochoric, or deviatoric, component of the internal forces, and the domain of integration has been changed from V_0 to that in the configuration at time level n, V_n, noting that $dV_0 = J_n dV_n$. Note also that the divergence of $\delta\mathbf{v}_n$ is taken at the current configuration n. Introducing the additional velocity variable, $\mathbf{v}^*_{n+1/2}$, the above expression can now be re-arranged in a more traditional fractional step format as,

$$M\left(\delta\mathbf{v}_n, \frac{\mathbf{v}^*_{n+1/2} - \mathbf{v}_{n-1/2}}{\Delta t}\right) = F(\delta\mathbf{v}_n; \mathbf{x}_n) - T'(\delta\mathbf{v}_n; \mathbf{x}_n) - \frac{1}{2}\int_{V_n} p_{n-1/2}\text{div}\delta\mathbf{v}_n\, dV_n\ , \tag{4.6}$$

$$M\left(\delta\mathbf{v}_n, \frac{\mathbf{v}_{n+1/2} - \mathbf{v}^*_{n+1/2}}{\Delta t}\right) = -\frac{1}{2}\int_{V_n} p_{n+1/2}\ \text{div}\delta\mathbf{v}_n\, dV_n\ . \tag{4.7}$$

Assuming $\mathbf{x}_n$, $\mathbf{x}_{n+1}$ and $p_{n-1/2}$ are known, $\mathbf{v}^*_{n+1/2}$ can be determined explicitly from the first equation. However, the computation of $\mathbf{v}_{n+1/2}$ from the second equation, requires the solution of an additional equation for $p_{n+1/2}$. This equation is derived from the stationarity condition of the action integral with respect to the pressure. This gives,

$$M_\kappa(\delta p, p_{n+1/2}) = \int_{V_0} \frac{1}{2}(J_n + J_{n+1} - 2)\delta p\, dV_0 \tag{4.8}$$

where the notation

$$M_\kappa(p,q) = \int_{V_0} \frac{1}{\kappa} p\, q\, dV_0 \ ,$$

has been used. Note that for incompressible materials $\kappa \to \infty$ and the above expression enforces that the average volume ratio should be one.

The combined solution of equations (4.8) and (4.7) is described below in the context of a finite element discretization.

4.3 Finite Element Spatial Discretization

Consider now a standard linear tetrahedral finite element space consisting of M nodes for both the pressure and geometry of the solid. The finite dimensional approximations p_h and $\mathbf{x}_h$, are given by,

$$p_h = \sum_{a=1}^{M} N^a(\mathbf{X})\, p_h^a \ ; \qquad \mathbf{x}_h = \sum_{a=1}^{M} N^a(\mathbf{X})\, \mathbf{x}_h^a \ . \tag{4.9}$$

The discretization of equations (4.6) and (4.7) is expressed as,

$$\mathbf{M}\frac{\mathbf{v}^*_{n+1/2} - \mathbf{v}_{n-1/2}}{\Delta t} = \mathbf{F}_n - \mathbf{T}'_n - \frac{1}{2}\mathbf{G}_n\mathbf{p}_{n-1/2} \tag{4.10}$$

$$\mathbf{M}\frac{\mathbf{v}_{n+1/2} - \mathbf{v}^*_{n+1/2}}{\Delta t} = -\frac{1}{2}\mathbf{G}_n\mathbf{p}_{n+\frac{1}{2}} \tag{4.11}$$

where $\mathbf{M}$ is the mass matrix, $\mathbf{F}$ the vector of external forces, $\mathbf{T}'$ are the equivalent internal forces due to the deviatoric component of the stress, $\mathbf{v}^T_{n+1/2} = [\mathbf{v}^1_{h,n+1/2}, \ldots \mathbf{v}^a_{h,n+1/2}, \ldots]$ (with $\mathbf{v}^a_{h,n+1/2} = (\mathbf{x}^a_{h,n+1} - \mathbf{x}^a_{h,n})/\Delta t$) are the nodal velocities, $\mathbf{p}^T = [p^1_h, \ldots p^a_h, \ldots]$ the nodal pressures and the gradient-like matrix at time level n, $\mathbf{G}_n$, has nodal components $[\mathbf{G}]^{ab}_n$ given by,

$$[\mathbf{G}]^{ab}_n = \int_{V_n} N^b \nabla_n N^a \, dV_n \ . \tag{4.12}$$

Note that the weighting functions in expression (4.10) corresponding to the velocity degrees of freedom which are prescribed by boundary conditions are set to zero. As a result all the entries in the row of $\mathbf{G}_n$ corresponding to a prescribed boundary velocity component are

equal to zero (i.e. the corresponding N^b is zero). Similarly, the constitutive equation (4.8) becomes,

$$\mathbf{M}_\kappa \mathbf{p}_{n+1/2} = \frac{1}{2}(\mathbf{V}_n + \mathbf{V}_{n+1} - 2\mathbf{V}_0) \ , \tag{4.13}$$

where the components of the volumetric mass matrix and the vector of nodal volumes are given by,

$$[\mathbf{M}_\kappa]^{ab} = \int_{V_0} \frac{1}{\kappa} N^a N^b \, dV_0 \quad ; \quad [\mathbf{V}_n]^a = \int_{V_n} N^a \, dV_n \ . \tag{4.14}$$

Equations (4.11) and (4.13) represent a set of nonlinear equations for the nodal pressures due to the fact that the volume vector $\mathbf{V}_{n+1}$ depends nonlinearly on the nodal positions at $n+1$ which in turn are functions of the pressure at $n+1/2$. This can solved using a standard Newton-Raphson algorithm. In order to derive the incremental equation, note first that the linearization of the nodal volumes is expressed as,

$$D\mathbf{V}^{(i)}_{n+1}[\Delta \mathbf{x}^{(i)}_{n+1}] = \mathbf{G}^{T,(i)}_{n+1} \Delta \mathbf{x}^{(i)}_{n+1} \ , \tag{4.15}$$

where $\Delta \mathbf{x}^{(i)}_{n+1} = \mathbf{x}^{(i+1)}_{n+1} - \mathbf{x}^{(i)}_{n+1}$ and, $\mathbf{V}^{(i)}_{n+1}$ and $\mathbf{G}^{T,(i)}_{n+1}$, are calculated from the i-th iterate of $\mathbf{x}_{n+1}$, $\mathbf{x}^{(i)}_{n+1}$. In addition, combining $\mathbf{x}_{n+1} = \mathbf{x}_n + \Delta t \, \mathbf{v}_{n+1/2}$ and the linearized form of equation (4.11) gives,

$$\Delta \mathbf{x}^{(i)}_{n+1} = -\frac{1}{2} \Delta t^2 \mathbf{M}^{-1} \mathbf{G}_n \Delta \mathbf{p}^{(i)}_{n+1/2} \ , \tag{4.16}$$

where $\Delta \mathbf{p}^{(i)}_{n+1/2} = \mathbf{p}^{(i+1)}_{n+1/2} - \mathbf{p}^{(i)}_{n+1/2}$. Equations (4.15) and (4.16) can now be combined with expression (4.13) to yield a Newton-Raphson iteration process for the pressure increment $\Delta \mathbf{p}^{(i)}_{n+1/2}$,

$$(\mathbf{M}_\kappa + \frac{1}{4} \Delta t^2 \mathbf{G}^{\mathbf{T},(i)}_{n+1} \mathbf{M}^{-1} \mathbf{G}_n) \Delta \mathbf{p}^{(i)}_{n+1/2} = \frac{1}{2}(\mathbf{V}_n + \mathbf{V}^{(i)}_{n+1} - 2\mathbf{V}_0) - \mathbf{M}_k \mathbf{p}^{(i)}_{n+1/2} \ . \tag{4.17}$$

The initial value for the iteration is $\mathbf{p}^{(0)}_{n+1/2} = \mathbf{p}_{n-1/2}$, and, from (4.11), $\mathbf{x}^{(0)}_{n+1} = \mathbf{x}_n + \Delta t \mathbf{v}^*_{n+1/2} - (\Delta t/2) \mathbf{M}^{-1} \mathbf{G}_n \mathbf{p}^{(0)}_{n+1/2}$. Note that once a new pressure increment has been computed solving the linear system (4.17), the geometry is easily updated using expression (4.16).

In the next section a simplified form of this algorithm will be discussed, which avoids

the Newton-Raphson iteration.

For computational convenience both the mass matrix and volumetric mass matrix will be lumped. In the latter case doing this permits the direct evaluation of the nodal pressures from equation (4.13) to give,

$$p^a_{h,n+1/2} = \frac{\kappa}{2}(J^a_n + J^a_{n+1} - 2)\,; \qquad J^a_n = \frac{[\mathbf{V}_n]^a}{[\mathbf{V}_0]^a} \tag{4.18}$$

Note that in the compressible case, it is now possible to eliminate the pressure and redefine the incremental Lagrangian in a more conventional form as a function of nodal positions alone as,

$$L_{n,n+1}(\mathbf{x}_n, \mathbf{x}_{n+1}) = \frac{1}{2}\mathbf{v}^T_{n+1/2}\mathbf{M}\mathbf{v}_{n+1/2} - \Pi_{\text{iso}}(\mathbf{x}_n) - \Pi_{\text{ext}}(\mathbf{x}_n) + \Pi_{\text{vol}}(\mathbf{x}_{n+1/2}) \tag{4.19}$$

where the volumetric component is,

$$\Pi_{\text{vol}}(\mathbf{x}_{n+1/2}) = \sum_{a=1}^{M} V^a_0 U(\frac{1}{2}J^a_n + \frac{1}{2}J^a_{n+1})\,; \qquad U(J) = \frac{1}{2}\kappa(J-1)^2 \tag{4.20}$$

It is easy to verify that the incremental Lagrangian (4.19) leads to the same set of discrete equations. Note that equation (4.19) can be interpreted as using the central difference form for the deviatoric component of the internal energy and a mid-point form for the volumetric energy. The resulting scheme is therefore implicit in the pressure and should have a timestep only controlled by the speed of the shear wave.

4.4 Linearized Formulation

4.4.1 Linearization of the volume increment

The Newton-Raphson iteration that appears in the above evaluation of the nodal pressures can be eliminated if the volume increment per step is linearized. In effect, this is equivalent to the assumption that the displacements during the increment are small. This is in general a reasonable assumption to make given that the algorithms is still explicit with respect to the deviatoric component.

In order to calculate the pressure increment without the need for a Newton-Raphson iteration, consider the discretized constitutive equation (4.13) written in terms of the volume increment between steps as,

$$\mathbf{M}_\kappa \mathbf{p}_{n+1/2} = (\mathbf{V}_n - \mathbf{V}_0) + \frac{1}{2}\Delta\mathbf{V}_{n+1/2}\,; \qquad \Delta\mathbf{V}_{n+1/2} = \mathbf{V}_{n+1} - \mathbf{V}_n\,. \tag{4.21}$$

Assuming that the geometrical changes are small during the increments, the volume increment for a given node a can be expressed in terms of the divergence of the velocities as,

$$\begin{aligned} \Delta[\mathbf{V}_{n+1/2}]^a &= \int_{V_0} N^a (J_{n+1} - J_n)\, dV_0 && (4.22)\\ &\approx \Delta t \int_{V_n} N^a \operatorname{div} \mathbf{v}_{n+1/2}\, dV_n && (4.23)\\ &= \Delta t [\mathbf{G}_n^T \mathbf{v}_{n+1/2}]^a\,. && (4.24) \end{aligned}$$

The volumetric constitutive equation can therefore be linearized as,

$$\mathbf{M}_\kappa \mathbf{p}_{n+1/2} = (\mathbf{V}_n - \mathbf{V}_0) + \frac{\Delta t}{2}\mathbf{G}_n^T \mathbf{v}_{n+1/2}\,. \tag{4.25}$$

It is now possible to combine this expression with equation (4.11) for the mid step velocity to give a linear set of equations for the pressure as,

$$(\mathbf{M}_\kappa + \frac{1}{4}\Delta t^2 \mathbf{G}_n^T \mathbf{M}^{-1} \mathbf{G}_n)\mathbf{p}_{n+1/2} = (\mathbf{V}_n - \mathbf{V}_0) + \frac{\Delta t}{2}\mathbf{G}_n^T \mathbf{v}^*_{n+1/2} \tag{4.26}$$

The resulting time stepping algorithm can be summarized as shown in table 4.1.

4.4.2 First step

Finally it is clear that the first timestep requires special treatment, as the velocities and pressures at the previous half step are not known. (Note that the variational equilibrium equations 2.16 cannot be applied until two full configurations have been determined.) There are a number of ways in which this can be done, but the one which has been used in this research, and which appears to be more natural in the context of the above algorithm is

Steps for the Fractional time-step method:

1. Known : $\mathbf{x}_n$, $\mathbf{v}_{n-1/2}$, $\mathbf{p}_{n-1/2}$, $\mathbf{M}$, and $\mathbf{M}_\kappa$.
2. Calculate $\mathbf{F}_n$, $\mathbf{T}'_n$ and $\mathbf{G}_n$.
3. Calculate $\mathbf{v}^*_{n-1/2}$ using equation 4.10.
4. Calculate $\mathbf{p}_{n+1/2}$ and using equation 4.26.
5. Calculate $\mathbf{v}_{n+1/2}$ using equation 4.11.
6. Calculate $\mathbf{x}_{n+1}$ using $\mathbf{x}_{n+1} = \mathbf{x}_n + \Delta t\, \mathbf{v}_{n+1/2}$.

Table 4.1: Fractional time step algorithm

given by writing the equilibrium equation at time t_0 as,

$$\mathbf{M}\frac{\mathbf{v}^*_{1/2} - \mathbf{v}_0}{\Delta t/2} = \mathbf{F}_0 - \mathbf{T}'_0 - \frac{1}{2}\mathbf{G}_0\mathbf{p}_0 \,, \tag{4.27}$$

$$\mathbf{M}\frac{\mathbf{v}_{1/2} - \mathbf{v}^*_{1/2}}{\Delta t/2} = -\frac{1}{2}\mathbf{G}_0\mathbf{p}_{1/2} \,. \tag{4.28}$$

Note that if the initial configuration corresponds to the unstressed state of the body, last two terms on the right hand side of the first equation will vanish.

The above expression can be combined with the linearised constitutive equation written for the first half step as,

$$\mathbf{M}_\kappa\mathbf{p}_{1/2} = \frac{1}{2}\Delta\mathbf{V}_{1/2} \,; \qquad \Delta\mathbf{V}_{1/2} = \mathbf{V}_1 - \mathbf{V}_0 \approx \Delta t\, \mathbf{G}_0^T\mathbf{v}_{1/2} \,, \tag{4.29}$$

to give a set of linear equations for the pressure values at the first half step as,

$$(\mathbf{M}_\kappa + \frac{1}{8}\Delta t^2\mathbf{G}_0^T\mathbf{M}^{-1}\mathbf{G}_0)\mathbf{p}_{1/2} = \frac{\Delta t}{2}\mathbf{G}_0^T\mathbf{v}^*_{1/2} \,. \tag{4.30}$$

4.5 Linear Stability Analysis

It is clear from the previous section that the cost per step of the above algorithms is significantly greater than that of a standard explicit central difference, albeit it is still far

less than a typical implicit step, which inevitably involves solving a set of highly non-linear equations for the nodal positions. The use of this type of integration will therefore only be practical if the timestep size is considerably greater than that of an explicit step. The aim of this section is to prove that the linear stability limit for the fractional scheme is governed by the speed of the sheer wave, which for nearly incompressible problems will inevitably be far slower than the pressure wave. In order to prove this, consider first the geometrical incremental Lagrangian (4.19) for the small displacement linear elasticity case as,

$$\begin{aligned} L_{n,n+1}(\mathbf{u}_n, \mathbf{u}_{n+1}) &= \frac{\Delta t}{2}\mathbf{v}_{n+1/2}^T \mathbf{M}\mathbf{v}_{n+1/2} - \Delta t \Pi_{\text{ext}}(\mathbf{u}_n) \\ &\quad -\frac{\Delta t}{2}\mathbf{u}_{n+1/2}^T \mathbf{K}_{\text{vol}}\mathbf{u}_{n+1/2} - \frac{\Delta t}{2}\mathbf{u}_n^T \mathbf{K}_{\text{iso}}\mathbf{u}_n \end{aligned} \tag{4.31}$$

where as before $\mathbf{v}_{n+1/2} = (\mathbf{u}_{n+1} - \mathbf{u}_n)/\Delta t$, $\mathbf{u}$ is the vector of nodal displacements, and $\mathbf{K}_{\text{vol}}$ and $\mathbf{K}_{\text{iso}}$ represent the volumetric and isochoric (i.e. deviatoric) components of the stiffness matrix. Typically, for nearly incompressible materials $\mathbf{K}_{\text{vol}}$ will be far stiffer than $\mathbf{K}_{\text{iso}}$ and consequently it is important that it does not play a role in the evaluation of the critical timestep.

The corresponding stationary conditions lead now to the following set of linear equations,

$$\frac{1}{\Delta t^2}\mathbf{M}(\mathbf{u}_{n+1} - 2\mathbf{u}_n + \mathbf{u}_{n-1}) + \mathbf{K}_{\text{iso}}\mathbf{u}_n + \frac{1}{2}\mathbf{K}_{\text{vol}}(\mathbf{u}_{n+1/2} + \mathbf{u}_{n-1/2}) = \mathbf{F}_n \ . \tag{4.32}$$

The homogenous part of the above equation can be re-arranged to give,

$$\hat{\mathbf{M}}(\mathbf{u}_{n+1} + \mathbf{u}_{n-1}) + \Delta t^2(\mathbf{K} - \frac{2}{\Delta t^2}\hat{\mathbf{M}})\mathbf{u}_n = 0 \ , \tag{4.33}$$

where,

$$\hat{\mathbf{M}} = \mathbf{M} + \frac{4}{\Delta t^2}\mathbf{K}_{\text{vol}} \ ; \qquad \mathbf{K} = \mathbf{K}_{\text{vol}} + \mathbf{K}_{\text{iso}} \ . \tag{4.34}$$

Consider now the eigenvalue problem $\mathbf{K}\mathbf{w} = \lambda\hat{\mathbf{M}}\mathbf{w}$ and express the displacements as a linear combination of the corresponding eigenvectors as $\mathbf{u}_n = \sum_i r_n^i \mathbf{w}_i$. Substituting into

equation (4.33) leads to the following difference equation for the modal components,

$$r_{n+1}^i - (2 - \lambda_i \Delta t^2) r_n^i + r_{n-1}^i = 0 \tag{4.35}$$

which, upon substitution of $r_n^i = A^n$, where $|A| \leq 1$ for stability, quickly leads to the standard timestep condition,

$$\Delta t \leq \frac{2}{\sqrt{\lambda_{\max}}} \tag{4.36}$$

In order to derive an upper bound for $\lambda_{\max}$ note that,

$$\lambda_{\max} = \max_{\mathbf{v}} \left(\frac{\mathbf{v}^T \mathbf{K} \mathbf{v}}{\mathbf{v}^T \hat{\mathbf{M}} \mathbf{v}} \right) = \max_{\mathbf{v}} \left(\frac{\mathbf{v}^T \mathbf{K}_{\text{iso}} \mathbf{v} + \mathbf{v}^T \mathbf{K}_{\text{vol}} \mathbf{v}}{\mathbf{v}^T \mathbf{M} \mathbf{v} + (\Delta t^2/4) \mathbf{v}^T \mathbf{K}_{\text{vol}} \mathbf{v}} \right) \tag{4.37}$$

Introducing now the maximum eigenvalue of the deviatoric stiffness component as,

$$\lambda_{\max}^{\text{iso}} = \max_{\mathbf{v}} \left(\frac{\mathbf{v}^T \mathbf{K}_{\text{iso}} \mathbf{v}}{\mathbf{v}^T \mathbf{M} \mathbf{v}} \right) \tag{4.38}$$

gives,

$$\lambda_{\max} \leq \max_{\mathbf{v}} \left(\frac{\lambda_{\max}^{\text{iso}} \mathbf{v}^T \mathbf{M} \mathbf{v} + (4/\Delta t^2)(\Delta t^2/4) \mathbf{v}^T \mathbf{K}_{\text{vol}} \mathbf{v}}{\mathbf{v}^T \mathbf{M} \mathbf{v} + (\Delta t^2/4) \mathbf{v}^T \mathbf{K}_{\text{vol}} \mathbf{v}} \right) \leq \max \left(\lambda_{\max}^{\text{iso}}, (4/\Delta t^2) \right) \tag{4.39}$$

Given that stability requires $\lambda_{max}(\Delta t^2/4) \leq 1$, the critical timestep limit is given by,

$$\Delta t \leq \frac{2}{\sqrt{\lambda_{\max}^{\text{iso}}}} \tag{4.40}$$

Thus, for the linear case, it is seen, that the time step is constrained purely by the isochoric eigenvalues and is independent of the volumetric part. The fully incompressible case can either be similarly studied using the pressure as a separate independent variable or more easily as a limit case of the above derivation. The examples shown below will indicate that the stability properties demonstrated here for the nearly incompressible linear case do in fact extend to the nonlinear and fully incompressible cases.

Finally, the maximum eigenvalue $\lambda_{\max}^{\text{iso}}$ is estimated as

$$\lambda_{\max}^{\text{iso}} = \frac{2\mu}{\rho(h_e)_{\min}^2} , \tag{4.41}$$

where $(h_e)_{\min}$, is the smallest characteristic element length over the whole mesh.

4.6 Pressure Stabilization

In the incompressible limit $\kappa \rightarrow \infty$, and $\mathbf{M}_k$ in equations (4.26) or (4.17) vanishes. As a result, the linear system of equations becomes singular. This can be seen by realizing that multiple solutions can be obtained by adding any vector field $\mathbf{w}$ satisfying $\mathbf{G}_n\mathbf{w} = \mathbf{0}$ to a given solution. In the implementation of the Fractional Step algorithm, a pressure stabilization term was introduced to the discrete internal Potential Energy, to remedy this problem.

$$\Pi_{\text{sta}}(\mathbf{p}_{n+1/2}) = \frac{1}{2}\mathbf{p}_{n+1/2}(\mathbf{M}_{\kappa^*}^L - \mathbf{M}_{\kappa^*})\mathbf{p}_{n+1/2} \; ; \qquad \kappa^* = \frac{1}{\epsilon} \tag{4.42}$$

where ϵ represents a small stability parameter and $\mathbf{M}_{\kappa^*}^L$ denotes the lumped version of the volumetric mass matrix $\mathbf{M}_{\kappa^*}$. It is now simple to show that the equation for the pressure (4.26), now becomes,

$$(\mathbf{M}_\kappa + \mathbf{M}_{\kappa^*}^L - \mathbf{M}_{\kappa^*} + \frac{1}{4}\Delta t^2 \mathbf{G}_n^T \mathbf{M}^{-1} \mathbf{G}_n)\mathbf{p}_{n+1/2} = (\mathbf{V}_n - \mathbf{V_0}) + \frac{\Delta t}{2}\mathbf{G}_n^T \mathbf{v}_{n+1/2}^*, \tag{4.43}$$

and equations (4.10) and (4.11) remain unchanged. The introduction of the difference between the lumped and consistent version of the volumetric mass matrix eliminates the artificial pressure modes from the system and will obviously vanish as the mesh is refined for any choice of the stability parameter ϵ.

4.7 Examples

4.7.1 A Plane Strain Case

Consider a square flat plate of unit side length under plane strain. The left and bottom boundaries were restricted to move only tangentially, whereas the top and right boundaries are restricted to move normally, as shown in figure 4-1. Under the assumption of small

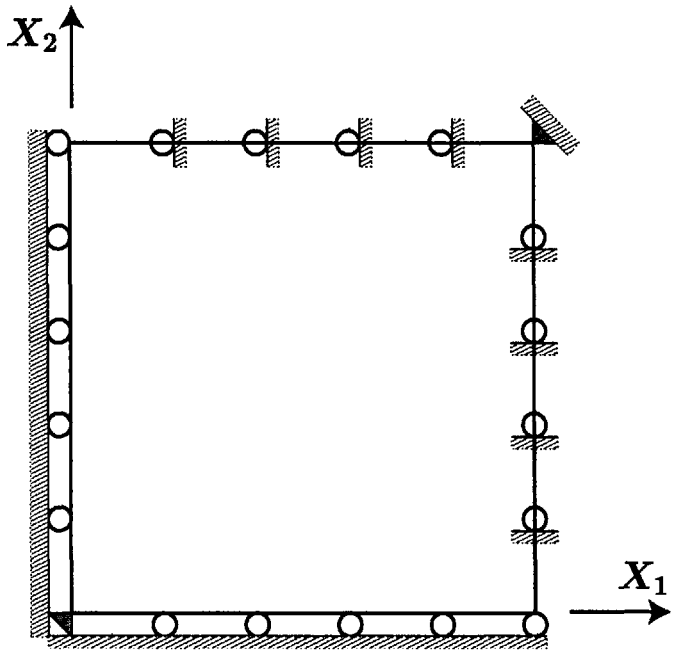

Figure 4-1: Two dimensional test case

displacements, $\mathbf{u} = \mathbf{x} - \mathbf{X}$, the isochoric and volumetric components of the internal energy become,

$$\Pi_{\text{iso}}(\mathbf{u}) = \int_V \mu\epsilon' : \epsilon' \, dV \; ; \qquad \epsilon' = \frac{1}{2}(\nabla\mathbf{u} + \nabla\mathbf{u}^T) - \frac{1}{3}(\operatorname{div}\mathbf{u})^2\mathbf{I} \tag{4.44}$$

$$\Pi_{\text{vol}}(\mathbf{u}, p) = \int_V p \operatorname{div}\mathbf{u} \, dV - \int_V \frac{p^2}{2\kappa} \, dV \; , \tag{4.45}$$

and the corresponding differential Euler-Lagrange equations can be reduced to,

$$(\lambda + \mu)\nabla(\operatorname{div}\mathbf{u}) + \mu\nabla^2\mathbf{u} = \rho\mathbf{u}_{tt} \tag{4.46}$$

where $\lambda = \kappa - \frac{2}{3}\mu$ is the standard Lame coefficient. An analytical solution for this problem is easily obtained. In particular, with the appropriate choice of initial condition the solution becomes, $(c_d = \sqrt{\frac{2\mu}{\rho}})$

$$\mathbf{u}(t) = U_0 \cos(\frac{c_d \pi t}{2}) \begin{bmatrix} \sin\left(\frac{\pi X_1}{2}\right) \cos\left(\frac{\pi X_2}{2}\right) \\ -\cos\left(\frac{\pi X_1}{2}\right) \sin\left(\frac{\pi X_2}{2}\right) \end{bmatrix} . \tag{4.47}$$

Note that this solution is only a function of μ, and is independent of the compressibility of the material. In order to test the formulation, the domain was discretized into 288 equal triangles, and run this problem with the fractional step algorithm proposed with a non-linear Neo-Hookean material as well as with the linearized small displacement potentials given by equations (4.44, 4.45). For values of U_0 below 0.001, no appreciable difference in the computed solutions is noticed.

Figure 4-2 shows the displacement of the point at $X_1 = 1$, $X_2 = 0$ versus the non-dimensional time, compared to the analytical solution. In this case the code was run assuming nearly incompressibility for a value of $\kappa/\mu = 5000$, which corresponds to a Poisson's ratio of $\nu = (1 - \mu/\kappa)/2 = 0.4999$. The agreement with the analytical solution is excellent. Note that if this problem had been run with an explicit code, the timestep would have been of the order of $\Delta t \sim (h_e)_{\min}/\sqrt{(\lambda + 2\mu)/\rho}$ which would have been about 35 times smaller than the timestep used in the calculation. Figure 4-3 shows the same calculation but now for a totally incompressible material $\nu = 0.5$. This case could not be run with an explicit code as, in this case, the size of the allowable timestep would go to zero. It is observed, that the results are undistinguishable from the previous nearly incompressible case, as expected. Finally, in figure 4-4 depicts the time history of the normalized total energy, E, showing also the contribution from the kinetic, $M(\mathbf{v_{n+1/2}}, \mathbf{v_{n+1/2}})/2$, and potential $\Pi_{\text{iso}}(\mathbf{x_n}) + \Pi_{\text{ext}}(\mathbf{x_n})$ components. Here, the potential energy due to volumetric deformation is equal to zero. It is clear that since the external forces do not do any work, the total energy should be conserved. Numerically, a small oscillation about the conserved value is observed, which, decreases when the discretization is refined. Nevertheless, the average level of the total energy does not decay but stays constant.

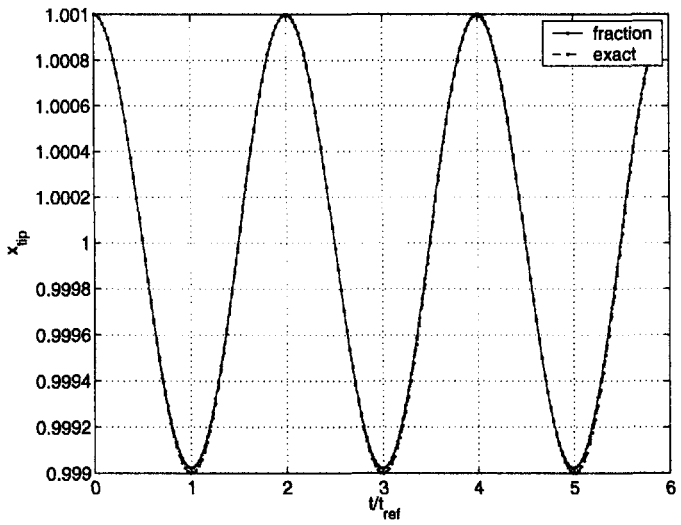

Figure 4-2: Displacement of point $X_1 = 1$, $X_2 = 0$ in time for nearly incompressible solution ($\nu = 0.4999$) compared with analytical solution.

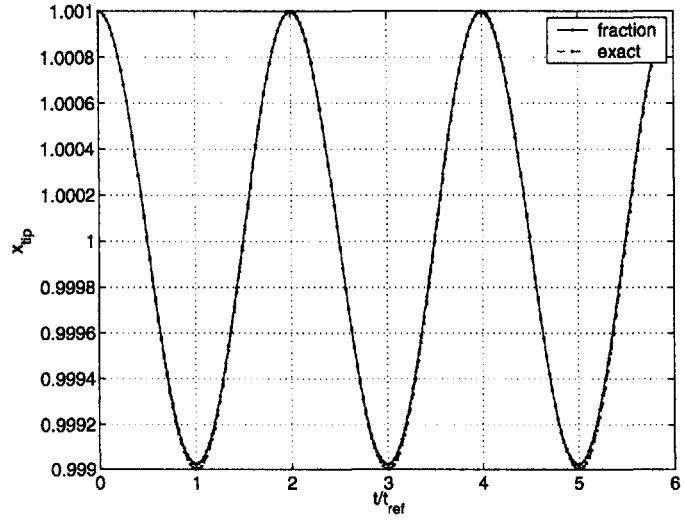

Figure 4-3: Displacement of point $X_1 = 1$, $X_2 = 0$ in time for incompressible solution ($\nu = 0.5$) compared with analytical solution.

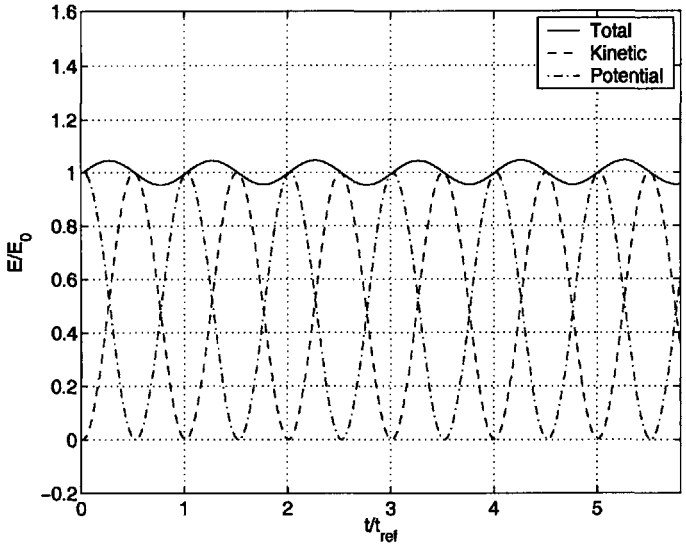

Figure 4-4: Energy History.

4.7.2 A spinning plate

A unit thickness square plate without any constraints is released without any initial deformation and an initial angular velocity of 1 rad/s, figure 4-5. This problem is chosen to illustrate the conservation properties of fractional time stepping algorithm proposed. The density of the plate and edge length are chosen to be unity. The Young's modulus given by, $3\mu/(1+\mu/(3\kappa))$ was chosen to be unity and the Poisson's ratio, $(1-\mu/\kappa)/2$, was 0.45. The plate was meshed with 288 equal linear triangular elements as shown in figure 4-6, which also shows the levels of the pressure distribution. Given that the center of mass is initially at zero velocity, it is expected to remain so. In addition, the angular momentum, $\int_{V_0} \mathbf{x}_{n+1} \times \mathbf{v}_{n+1/2} \rho_0 dV_0$, is expected to stay constant at its initial value. The time history of the linear and angular momentum are shown in figure 4-7. Note that the initial conditions used here, are such that there is no steady state solution, even in a rotating reference frame.

4.7.3 2D Beam bending

The bottom side of a unit thickness beam, moving at a constant velocity $V_0 = 0.1$, is instantly brought to rest as shown in figure 4-8. The density of the material of the beam, its Young's modulus, and the width of the beam are chosen to be unity. The Poisson's ratio, $(1-\mu/\kappa)/2$ of the material was 0.45 and the length of the beam was taken to be

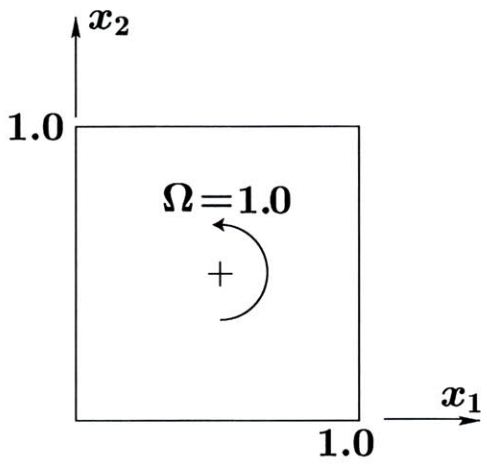

Figure 4-5: Spinning plate test case.

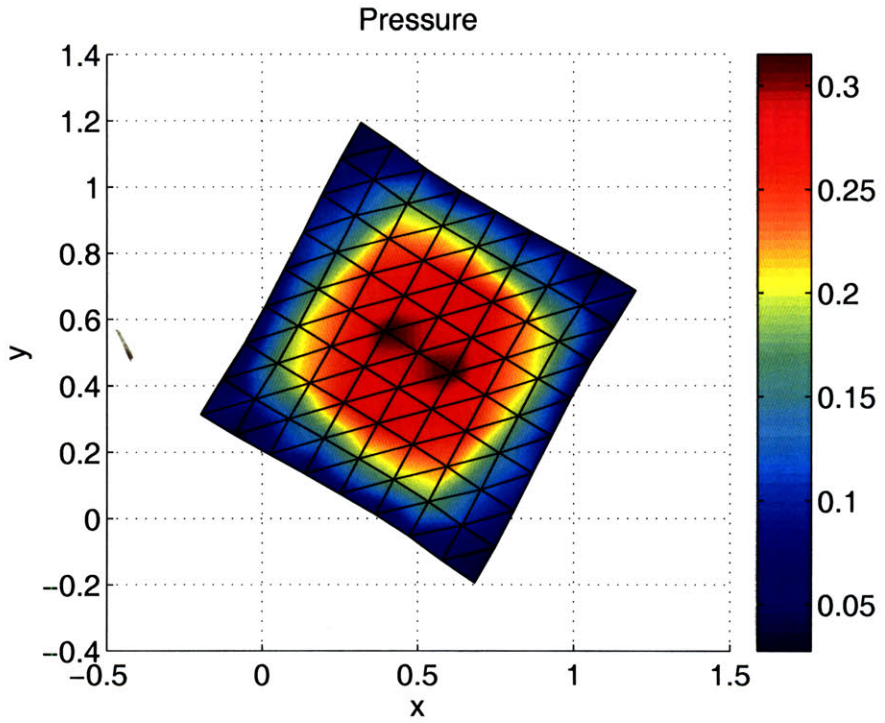

Figure 4-6: Finite element mesh and pressure distribution at a given instant.

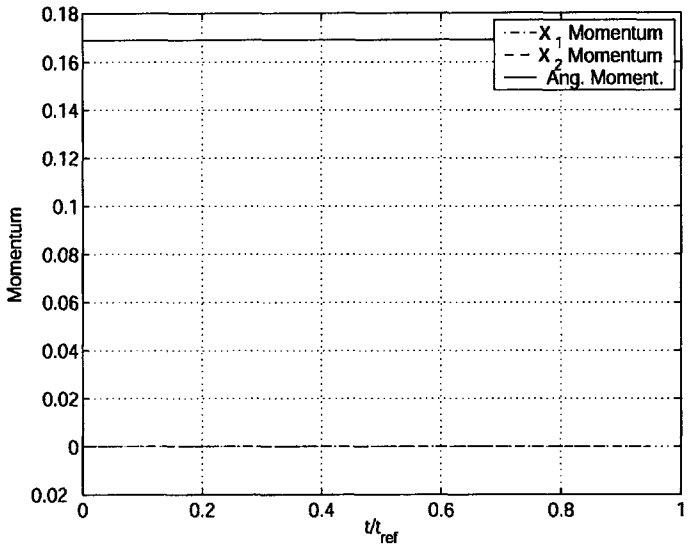

Figure 4-7: Linear momentum and angular momentum plots.

6.0. This problem is a non-linear and involves large deformations. The beam is was meshed with linear triangular elements as shown in figure 4-9 where the pressure distribution at a given time during the simulation is also shown.

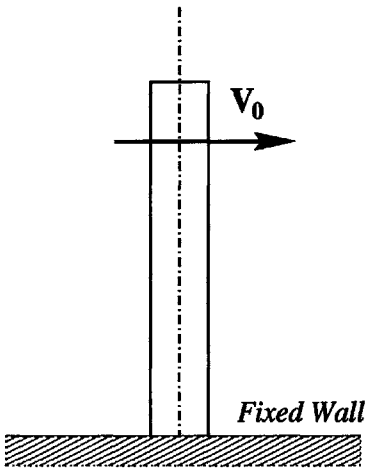

Figure 4-8: Beam bending

For this problem, the time evolution of the energy is shown in figure 4-10. Here, the potential energy is given by $\Pi_{\text{iso}}(\mathbf{x_n}) + \Pi_{\text{ext}}(\mathbf{x_n}) + \int_{V_0}(p_{n+1}/2)(J_{n+1} + J_n - 2)dV_0 - \int_{V_0}(p_{n+1}^2/2\kappa)dV_0$. Numerically, it is seen, that the energy oscillates about the exact constant value. Again, we note that the scheme is non-dissipative and therefore very well suited for long time integrations.

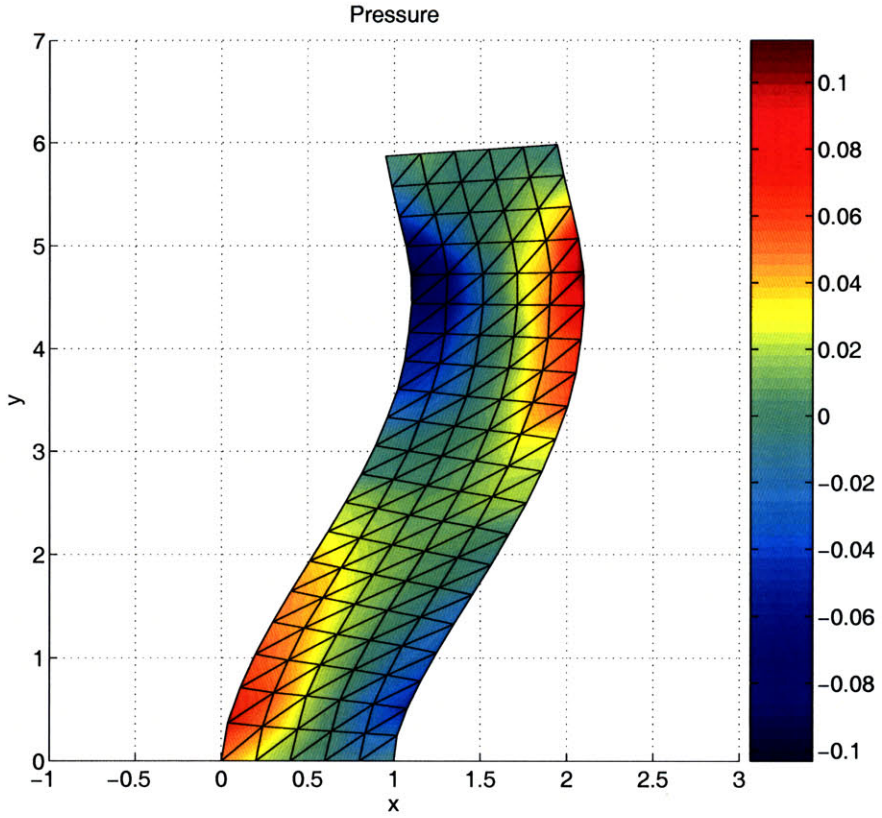

Figure 4-9: Pressure distribution in the beam.

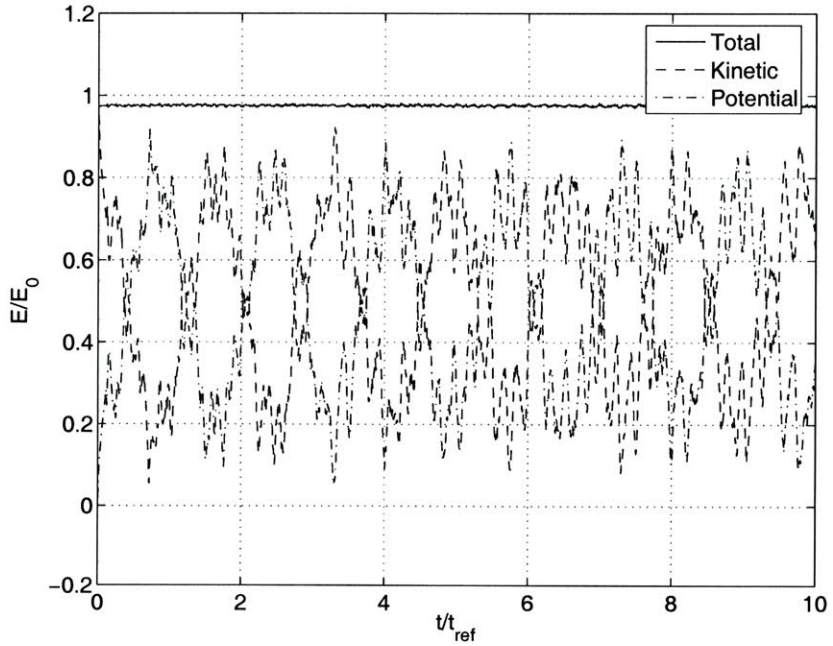

Figure 4-10: Energy fluctuations in the case of fractional method.

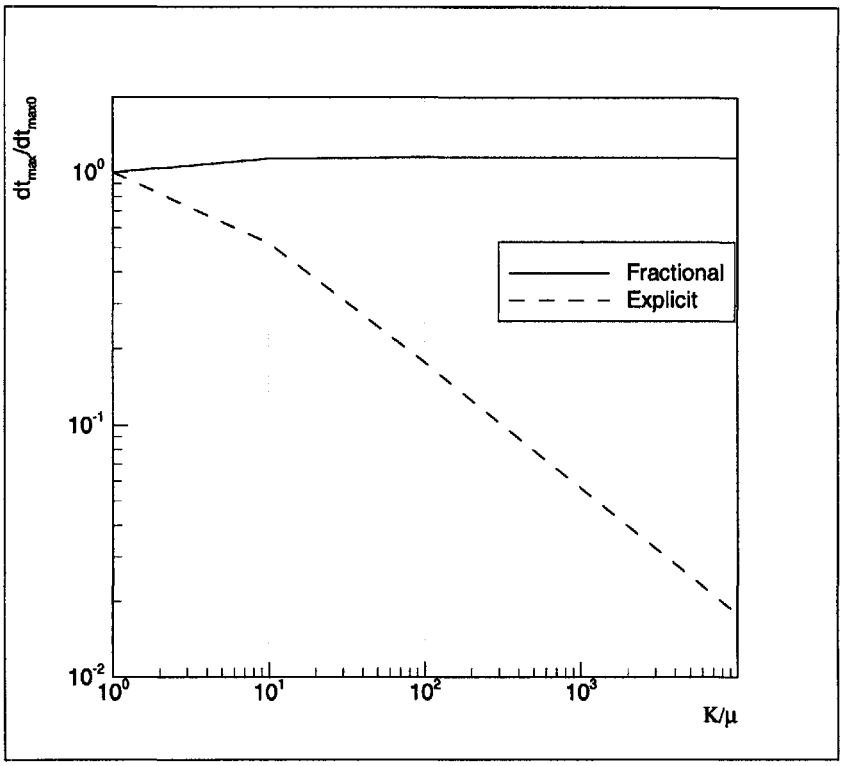

Figure 4-11: Dependency of maximum stable timestep on bulk modulus

4.8 Concluding Remarks

In this chapter a fractional step algorithm has been described, for the simulation of dynamic problems involving incompressible or nearly incompressible materials. The method has a variational interpretation and it can be easily shown to conserve exactly linear and angular momentum. In addition the method possesses excellent energy conservation properties which makes it well suited for long time integrations. The method requires the solution of a symmetric Poisson-like equation at each timestep for the pressure variable. This is clearly much cheaper than a fully implicit scheme requiring the solution of a non-symmetric system of equations involving three times as many unknowns (in 3D). For large values of κ, the timestep size of the presented method is approximately $(\sqrt{3}/2)(\sqrt{\kappa/\mu})$ times larger than the timestep of the standard explicit scheme. Significant advantage near incompressiblity limit (larger κ/μ ratio) as seen in figure 4-11. Further work is clearly needed in order to assess the range of problems for which the extra cost induced by the fractional step method is compensated by the larger step size permitted. For the presented algorithm the linearized

analysis shows that the timestep should be independent of κ and this is confirmed by the computations in the linear and the non-linear regimes.

Chapter 5

Fractional time-step method with mesh adaptation

In this chapter the fractional time-step method is extended to incorporate node movement. To develop the framework for doing so, the variational formulations are revisited. A combined formulation incorporating mixed formulation, (as presented in chapter 4), and node movement (as described in chapter 3), is developed.

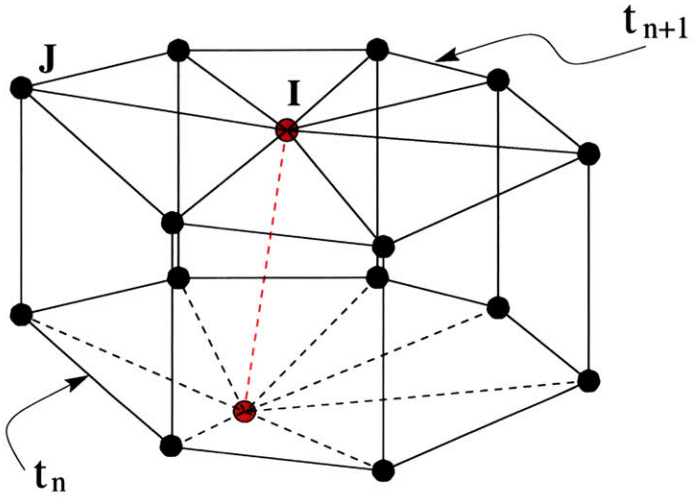

Figure 5-1: Space-time volume for node movement.

5.1 Variational Formulation

We recall from chapter 4, the variational formulation, where the Lagrangian for the Fractional time-step method (Eqn. 4.4) was written as:

$$\begin{aligned} L_{n,n+1}\left(\boldsymbol{x}_n, \boldsymbol{x}_{n+1}, p_{n+\frac{1}{2}}\right) &= K_{n,n+1}(\boldsymbol{x}_n, \boldsymbol{x}_{n+1}) - \Delta t\ \Pi_{\text{iso}}(\boldsymbol{x}_n) - \Delta t\ \Pi_{\text{ext}}(\boldsymbol{x}_n) \\ &\quad -\Delta t \int_{V_0} \frac{1}{2} p_{n+1/2}(J_{n+1} + J_n - 2)\, dV_0 + \Delta t \int_{V_0} \frac{p_{n+1/2}^2}{2\kappa}\, dV_0 \end{aligned} \tag{5.1}$$

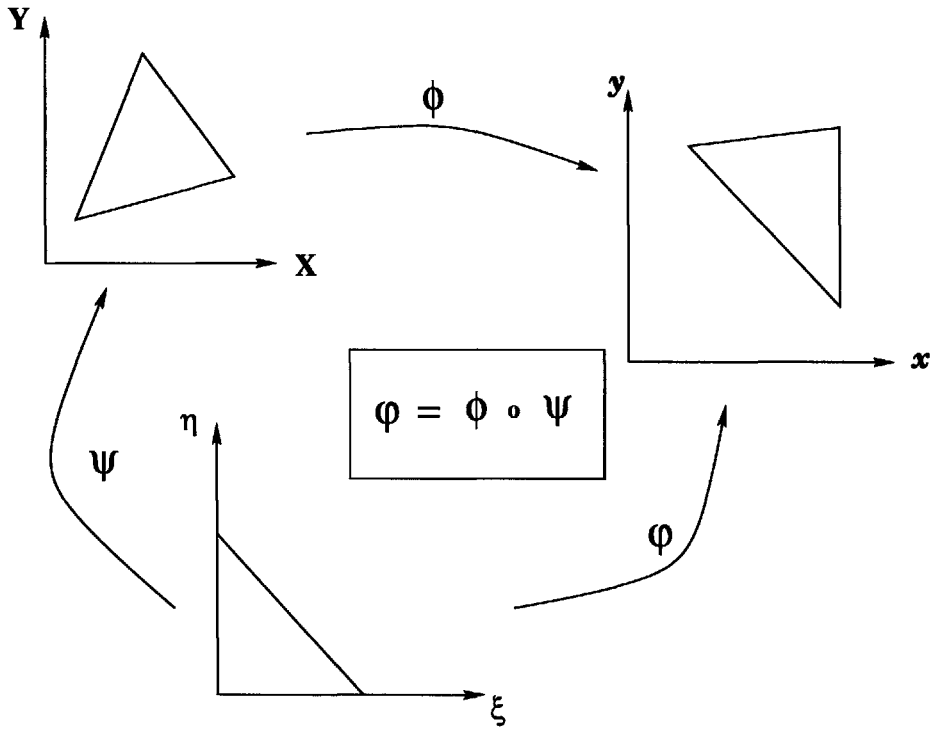

Figure 5-2: Node movement with an intermediate mapping.

To include the node movement algorithm into the time-integration, procedure, this Lagrangian is rewritten using the parametric space $V_\xi(\xi, \eta)$ as shown in the figure 5-2. The final expression becomes:

$$\begin{aligned} L_{n,n+1}\left(\boldsymbol{x}_n, \boldsymbol{x}_{n+1}, p_{n+\frac{1}{2}}\right) &= K_{n,n+1}(\boldsymbol{x}_n, \boldsymbol{x}_{n+1}) - \Delta t\ \Pi_{\text{iso}}(\boldsymbol{x}_n) - \Delta t\ \Pi_{\text{ext}}(\boldsymbol{x}_n) \\ &\quad - \int_t \int_{V_\xi} \frac{1}{2} p\ (J_{n+1} + J_n - 2)\, J_\xi dV_\xi dt + \int_t \int_{V_\xi} \frac{p^2}{2\kappa}\, J_\xi dV_\xi dt \end{aligned} \tag{5.2}$$

where (from chapter 3) the Kinetic Energy Integral $K_{n,n+1}$ can be expressed as :

$$K_{n,n+1}\left(\boldsymbol{x}_n, \boldsymbol{x}_{n+1}\right) = \frac{\Delta t}{2} \sum_I M_I^{n+1/2} \boldsymbol{v}_{n,n+1}^I . \boldsymbol{v}_{n,n+1}^I \tag{5.3}$$

where:

$$\begin{aligned}
M_I^{n+1/2} &= \frac{1}{2}\left(M_I^n + M_I^{n+1}\right) \\
\boldsymbol{v}_{n,n+1}^I &= \nu_{n+1/2}^I - \boldsymbol{F}_n^I \boldsymbol{V}_{n+1/2}^I \\
\nu_{n+1/2}^I &= \frac{1}{\Delta t}\left(\boldsymbol{x}_{n+1}^I - \boldsymbol{x}_n^I\right) \\
\boldsymbol{V}_{n+1/2}^I &= \frac{1}{\Delta t}\left(\boldsymbol{X}_{n+1}^I - \boldsymbol{X}_n^I\right) \\
\boldsymbol{F}_n^I &= \left(\frac{\int_{V_0} N_I^n \boldsymbol{F}_n dm}{\int_{V_0} N_I^n dm}\right)
\end{aligned}$$

The first pressure term on the right hand side of Eqn. 5.2 has only pressure as a time varying unknown within the space-time integral. Note that the term $(J_{n+1} + J_n - 2)$ does not vary with time within the space-time volume. Since pressure is an unknown at each node within two time levels, the integral $\left(\int_t p\, dt\right)$ can be approximated by $\Delta t\, p_{n+1/2}$ based on linear interpolation in time. The second pressure term is averaged over the two time levels, n and $n+1$. Now, the approximation to the Lagrangian becomes:

$$\begin{aligned}
L_{n,n+1}\left(\boldsymbol{x}_n, \boldsymbol{x}_{n+1}, p_{n+\frac{1}{2}}\right) &= K_{n,n+1}(\boldsymbol{x}_n, \boldsymbol{x}_{n+1}) - \Delta t\, \Pi_{\text{iso}}(\boldsymbol{x}_n) - \Delta t\, \Pi_{\text{ext}}(\boldsymbol{x}_n) \\
&\quad -\Delta t \int_{V_\xi} \frac{1}{2} p_{n+1/2}(J_{n+1} + J_n - 2)\, J_\xi dV_\xi \\
&\quad + \frac{\Delta t}{2} \int_{V_0^{n+1}} \frac{p_{n+1/2}^2}{2\kappa}\, dV_0^{n+1} + \frac{\Delta t}{2} \int_{V_0^n} \frac{p_{n+1/2}^2}{2\kappa}\, dV_0^n
\end{aligned} \tag{5.4}$$

Using stationarity *wrt.* $\boldsymbol{x}_n$ the following equations are obtained:

$$\begin{aligned}
&D_2 K_{n-1,n}(\boldsymbol{x}_{n-1}, \boldsymbol{x}_n)[\delta \boldsymbol{x}_n] + D_1 K_{n,n+1}(\boldsymbol{x}_n, \boldsymbol{x}_{n+1})[\delta \boldsymbol{x}_n] \\
&= F(\delta \boldsymbol{v}_n; \boldsymbol{x}_n) - T'(\delta \boldsymbol{v}_n; \boldsymbol{x}_n) - \int_{V_n} \frac{1}{2}(p_{n-1/2} + p_{n+1/2}) \text{div} \delta \boldsymbol{v}_n\, dV_n
\end{aligned} \tag{5.5}$$

Now using spatial interpolation, the following discrete update equations are obtained:

$$M_I^{n+1/2}\boldsymbol{v}_{n,n+1}^I - M_I^{n-1/2}\boldsymbol{v}_{n-1,n}^I = -\Delta t\boldsymbol{Q}_{n,n+1}^I + \Delta t\left(\boldsymbol{F}_n^I - \boldsymbol{T'}_n^I\right) - \frac{\Delta t}{2}\left(\boldsymbol{G}_n\left(p_{n+1/2}+p_{n-1/2}\right)\right)^I \quad (5.6)$$

where:

$$\boldsymbol{v}_{n,n+1}^I = \frac{1}{\Delta t}\left[\left(\boldsymbol{x}_{n+1}^I - \boldsymbol{x}_n^I\right) - \boldsymbol{F}_n^I\left(\boldsymbol{X}_{n+1}^I - \boldsymbol{X}_n^I\right)\right]$$

$$\boldsymbol{Q}_{n,n+1}^I = \sum_J \frac{m_J^{n+1/2}}{m_J^n}\left(\boldsymbol{v}_{n,n+1}^J \otimes \boldsymbol{V}_{n,n+1}^J\right)\int_{V_0} N_J^n \nabla_0 N_I^n dm$$

Clearly, this is an implicit expression. Hence, a fractional time-step is devised. Fractionally updated quantities $\boldsymbol{v}_{n,n+1}^*$ and $Q_{n,n+1}^*$ are introduced. The resulting steps look like:

$$M_I^{n+1/2}\boldsymbol{v}^{*I}_{n,n+1} - M_I^{n-1/2}\boldsymbol{v}_{n-1,n}^I = \Delta t\left[\boldsymbol{F}_n^I - \boldsymbol{T'}_n^I - \frac{1}{2}\left(\boldsymbol{G}_n p_{n-1/2}\right)^I - \boldsymbol{Q}_{n,n+1}^{*I}\right] \quad (5.7)$$

$$M_I^{n+1/2}\boldsymbol{v}_{n,n+1}^I - M_I^{n+1/2}\boldsymbol{v}^{*I}_{n,n+1} = \Delta t\left[\frac{-1}{2}\left(\boldsymbol{G}_n p_{n+1/2}\right)^I - \boldsymbol{Q}_{n,n+1}^I + \boldsymbol{Q}_{n,n+1}^{*I}\right] \quad (5.8)$$

where

$$\boldsymbol{Q}_{n,n+1}^{*I} = \sum_J \frac{m_J^{n+1/2}}{m_J^n}\left(\boldsymbol{v}^{*J}_{n,n+1} \otimes \boldsymbol{V}_{n,n+1}^J\right)\int_{V_0} N_J^n \nabla_0 N_I^n dm$$

In order to make the update in Eqn. 5.7, explicit, the neighbouring nodes of a chosen node, are not allowed to be moved within a given time level, as mentioned in chapter 3. This makes the node movement restrictive. Yet, employing node movement in successive time levels, all the nodes can be moved, during the course of simulation. Thus by introducing the fractional time-step, we obtain an explicit step, (Eqn. 5.7) followed by equation (Eqn. 5.8) which remains implicit.

Now, we look at the next stationarity relation *wrt.* $p_{n+1/2}$ to obtain the pressure update

:

$$\frac{1}{2}\left(M_\kappa^{n+1}(\delta p_{n+1/2}, p_{n+1/2}) + M_\kappa^n(\delta p_{n+1/2}, p_{n+1/2})\right) = \int_{V_0} \frac{1}{2}(J_n + J_{n+1} - 2)\delta p \, dV_0 \tag{5.9}$$

Now, applying the spatial interpolation, we obtain the discrete update equation similar to the one obtained in chapter 4 as :

$$\left[\frac{1}{2}\left(\boldsymbol{M}_\kappa^{n+1} + \boldsymbol{M}_\kappa^n\right)\right] \boldsymbol{p}_{n+1/2} = \boldsymbol{V}_n - \boldsymbol{V}_0 + \frac{\Delta t}{2}\boldsymbol{G}_n^T \boldsymbol{v}_{n,n+1} \tag{5.10}$$

Now, combining the two equations 5.10 and 5.8 we obtain:

$$\begin{aligned}&\left[\frac{1}{2}\left(\boldsymbol{M}_\kappa^{n+1} + \boldsymbol{M}_\kappa^n\right) + \frac{\Delta t^2}{4}\boldsymbol{G}_n^T \boldsymbol{M}_{n+1/2}^{-1}\boldsymbol{G}_n\right] \boldsymbol{p}_{n+1/2} \\ &= \boldsymbol{V}_n - \boldsymbol{V}_0 + \frac{\Delta t}{2}\boldsymbol{G}_n^T\left(\boldsymbol{v}_{n,n+1}^* - \boldsymbol{M}_{n+1/2}^{-1}\left(\boldsymbol{Q}_{n,n+1} - \boldsymbol{Q}_{n,n+1}^*\right)\right)\end{aligned} \tag{5.11}$$

Thus, we obtain an implicit set of equations, since $\boldsymbol{Q}_{n,n+1}$ depends on $\boldsymbol{v}_{n,n+1}$. The term $\left(\boldsymbol{Q}_{n,n+1} - \boldsymbol{Q}_{n,n+1}^*\right)$ is relatively smaller than $\boldsymbol{v}_{n,n+1}^*$. Hence, an approximation is introduced, where in $M_{n+1/2}^{-1}\left(\boldsymbol{Q}_{n,n+1} - \boldsymbol{Q}_{n,n+1}^*\right)$ is neglected as compared to $\boldsymbol{v}_{n,n+1}^*$.

This leads to a first order approximation in the solution of $p_{n+1/2}$. However, it does not disturb the momentum conservation property since no such approximation is used in Eqn. 5.8. The pressure increment already includes linearization, hence this approximation doesn't change the order of error in the $p_{n+1/2}$ computation. We obtain the simplified equation as:

$$\left[\frac{1}{2}\left(M_\kappa^{n+1} + M_\kappa^n\right) + \frac{\Delta t^2}{4}\boldsymbol{G}_n^T M_{n+1/2}^{-1}\boldsymbol{G}_n\right] \boldsymbol{p}_{n+1/2} = \boldsymbol{V}_n - \boldsymbol{V}_0 + \frac{\Delta t}{2}\boldsymbol{G}_n^T \boldsymbol{v}_{n,n+1}^* \tag{5.12}$$

Thus, Eqns. 5.7, 5.12 and 5.8 lead to the final algorithm, similar to the fractional step method without node movement, as:

Steps for the Combined Algorithm:

1. Known : $\boldsymbol{x}_n$, $\boldsymbol{v}_{n-1/2}$, $\boldsymbol{p}_{n-1/2}$, $\boldsymbol{M}_{n-1/2}$, and $\boldsymbol{M}_{\kappa}^{n}$.
2. Calculate $\boldsymbol{F}_n$, $\boldsymbol{T}_n'$ and $\boldsymbol{G}_n$.
3. Choose desired $\boldsymbol{V}_{n+1/2}^{I}$ based on criteria.
4. Calculate $\boldsymbol{v}_{n-1/2}^{*}$ using equation 5.7.
5. Calculate $\boldsymbol{M}_{n+1/2}$ and $\boldsymbol{M}_{\kappa}^{n+1}$
6. Calculate $\boldsymbol{p}_{n+1/2}$ and using equation 5.12.
7. Calculate $\boldsymbol{v}_{n+1/2}$ using equation 5.8.
8. Calculate $\boldsymbol{x}_{n+1}$ using $\boldsymbol{x}_{n+1} = \boldsymbol{x}_n + \Delta t\, \nu_{n+1/2}$.

Table 5.1: Fractional time step algorithm with Node movement

5.2 Implementation

5.2.1 Criteria

The combined algorithm is demonstrated by moving the nodes to the local average positions in the current configuration. Nodes were selected based on how far they were from the average location of their neighbouring patch, as shown in Fig. 5-1. Nodes were moved towards the average location. This reduced mesh skewness. Although the algorithm is restrictive within one time-step, ie., not all the nodes can be moved simultaneously, with frequent node movements, acceptable node positions were obtained. It has been observed that typically node adaptation in two or three consecutive time steps is generally sufficient to handle reasonable amount of mesh skewness.

5.2.2 Stabilization

As mentioned in chapter 4, pressure stabilization for the fractional time-step method, was required, in case of completely incompressible cases $\nu = 0.5$. The mesh adaptation, was implemented using similar pressure stabilization for completely incompressible cases only,

as mentioned in 4. The stabilized equations were obtained as:

$$\left[\frac{1}{2}\left(M_{\kappa}^{n+1}+M_{\kappa}^{n}\right)+\left(M_{\kappa^*}^{L\,n+1}-M_{\kappa^*}^{n+1}\right)+\frac{\Delta t^2}{4}\boldsymbol{G}_n^T M_{n+1/2}^{-1}\boldsymbol{G}_n\right]\ \boldsymbol{p}_{n+1/2}$$
$$=\ \boldsymbol{V}_n-\boldsymbol{V}_0+\frac{\Delta t}{2}\boldsymbol{G}_n^T\boldsymbol{v}_{n,n+1}^{*} \tag{5.13}$$

Where $\kappa^* = \frac{1}{\epsilon}$ with small values of ϵ, $(0 < \epsilon \lesssim 1/\mu)$ was found to be sufficient for eliminating any pressure chequered-boarding type of mechanisms.

5.3 Examples

In this section, some examples are presented using the combined algorithm (table 5.1). To demonstrate the momentum conservation behaviour the spinning plate case described in previous chapters was chosen. A beam bending problem was chosen to study the energy behaviour. All cases were chosen to be completely incompressible ($\nu = 0.5$).

5.3.1 A Spinning plate

A unit thickness(1m) square plate with unit edge-length ($L = 1\text{m}$) and material properties ($E = 1\,\text{Pa}$, $\nu = 0.5$ and $\rho = 1\,\text{kg/m}^3$), was spun at 1 rad/sec about its center.
Figure 5-3 shows the pressure distribution on the spinning plate at its current configuration, while, figure 5-4 shows the pressure distribution on the reference configuration. A stabilization parameter $\epsilon = 10^{-5}$ was used in this case.

Figures 5-5 and 5-6 show the momentum and energy history, where the momentum is conserved exactly in time and the energy remains bounded during the course of the simulation. Figure 5-7 shows the the number of nodes moved at different adaptation steps.

5.3.2 Beam Bending

A unit thickness beam, moving at a constant velocity $V_0 = 0.1\,\text{m/s}$, was instantly brought to rest by fixing the bottom end of the beam at time ($t = 0$), as shown in figure 5-8. The length of the beam was ($L = 6\text{m}$), and width of the beam was ($w = 1\text{m}$). Other material

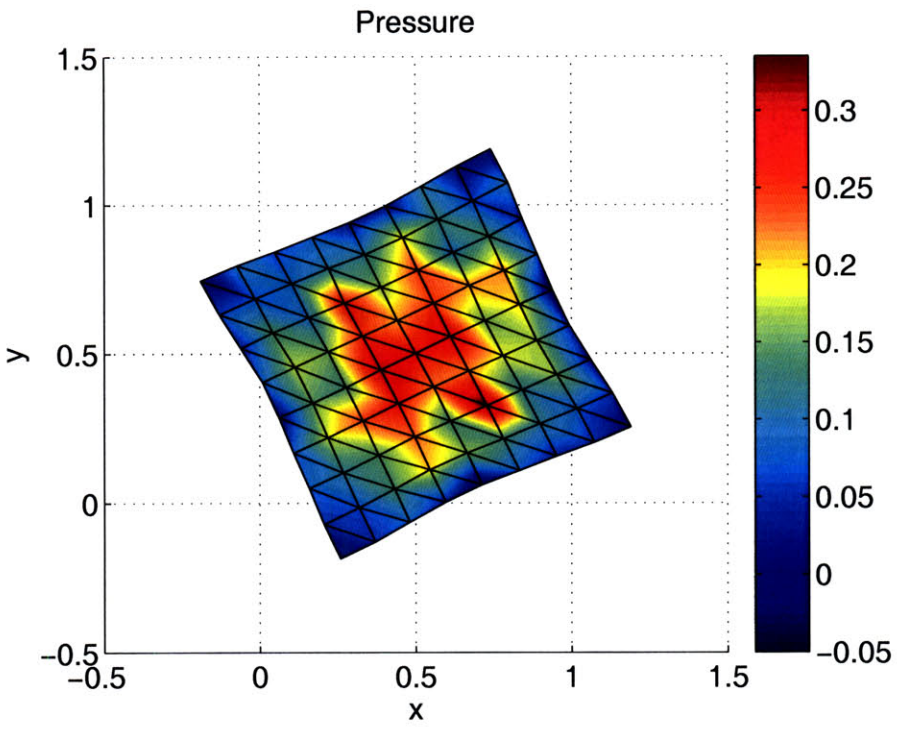

Figure 5-3: Pressure distribution on the spinning plate at the current configuration.

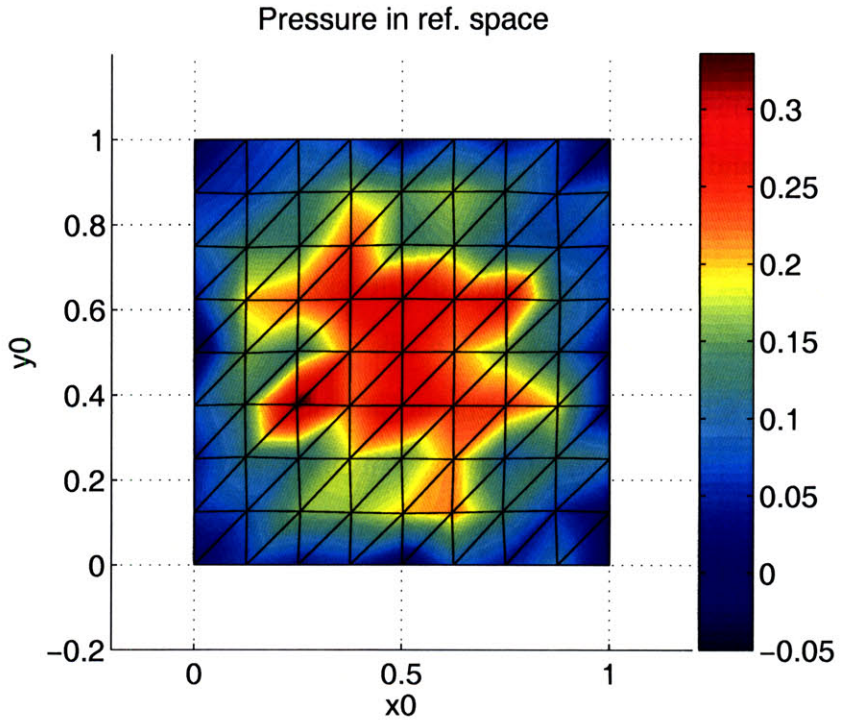

Figure 5-4: The pressure distribution in the reference configuration of the spinning plate.

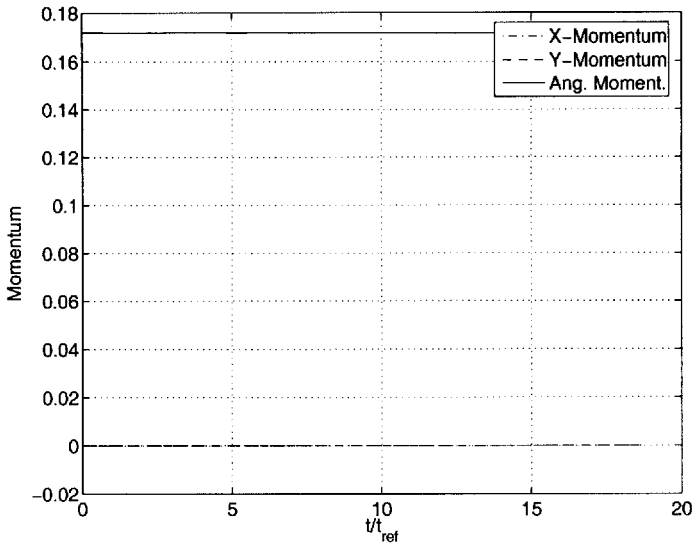

Figure 5-5: The momentum history.

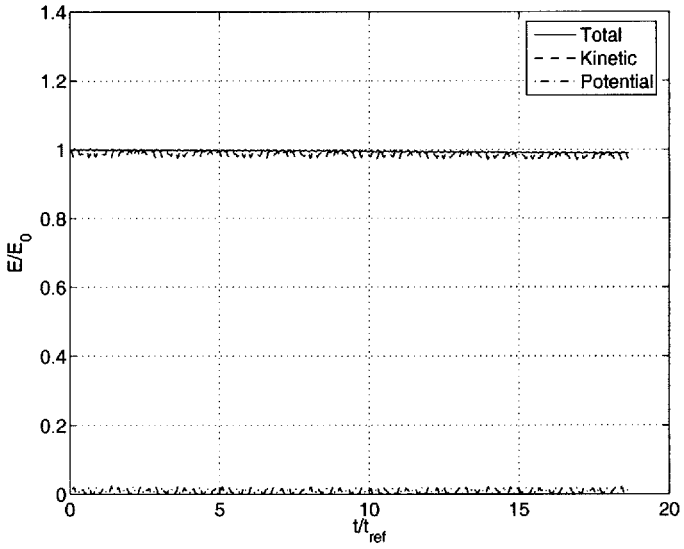

Figure 5-6: The Energy history.

properties were ($E = 1\,\text{Pa}$, $\nu = 0.5$ and $\rho = 1\,\text{kg/m}^3$).

The beam is was meshed with 400 linear triangular elements as shown in figure 5-9 where the pressure distribution at a given time is shown on the current configuration. The solution shown, is obtained at time $t = 10.0$s. Figure 5-10 shows the number of node movements conducted during the simulations.

The net energy at each time level was observed. The energy was the discrete energy obtained from the Variational formulation. Figure 5-12 shows the energy history without

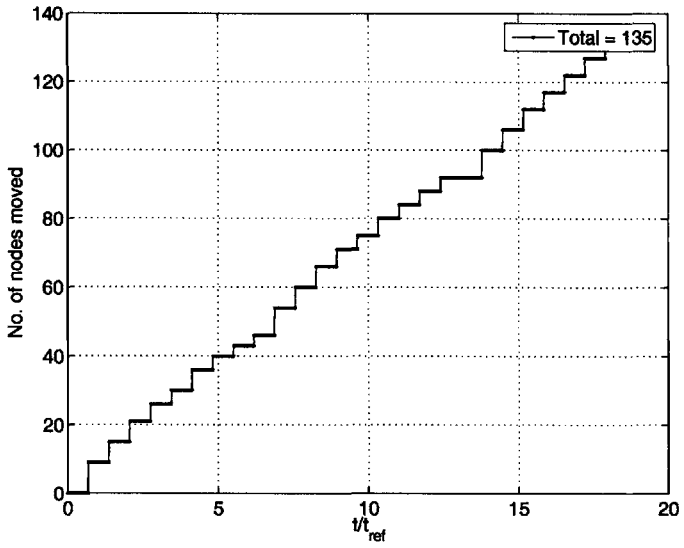

Figure 5-7: The Adaptation history showing the total number of node movements conducted.

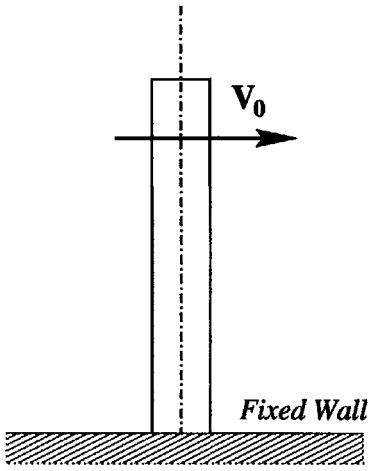

Figure 5-8: Beam bending

any node movement. Figure 5-11 shows the energy history with many node movements at different time levels. Distinct spikes of energy are observed at node movement steps. This might be attributed to the way the energy was measured at the adaptive step. Also small energy jumps might be expected, due to the approximations introduced within the adaptive step. It has to be noted that, energy remains bounded during the course of the simulation, without causing any instabilities or dissipation. Many nodes were moved at many time steps and yet the energy remained bounded, similar to the case of no node movement (figure 5-12).

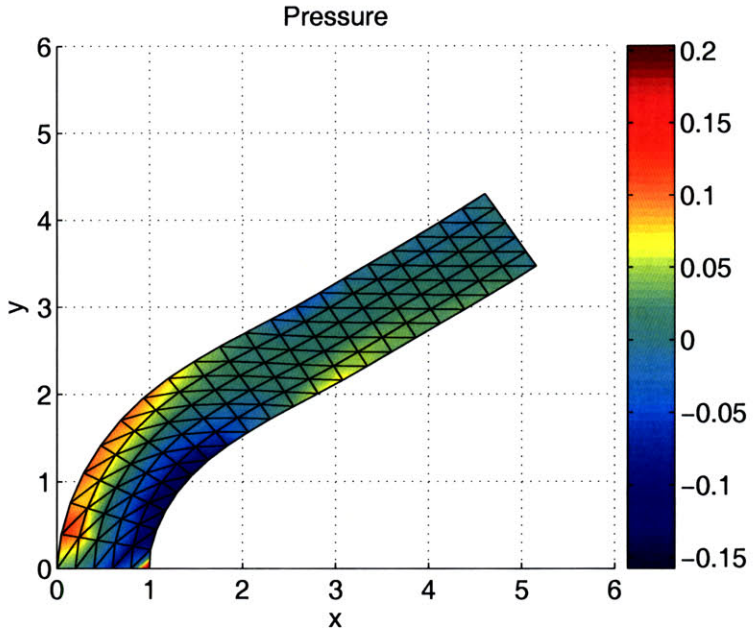

Figure 5-9: Pressure distribution in the beam on the current configuration.

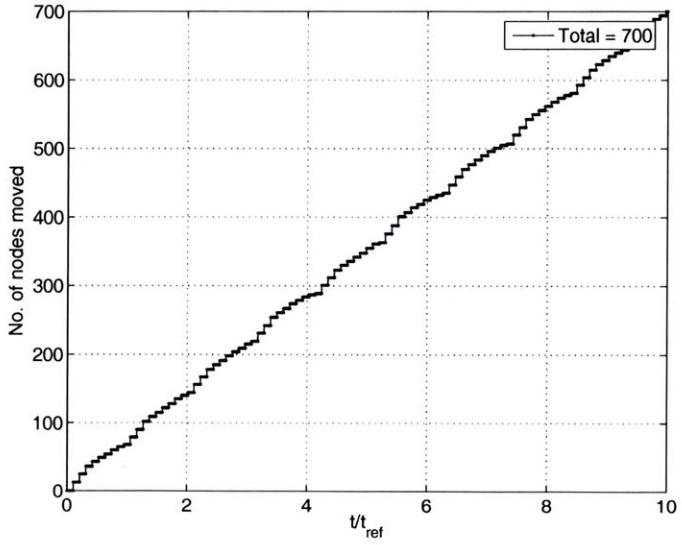

Figure 5-10: Total number of node movement at different time steps.

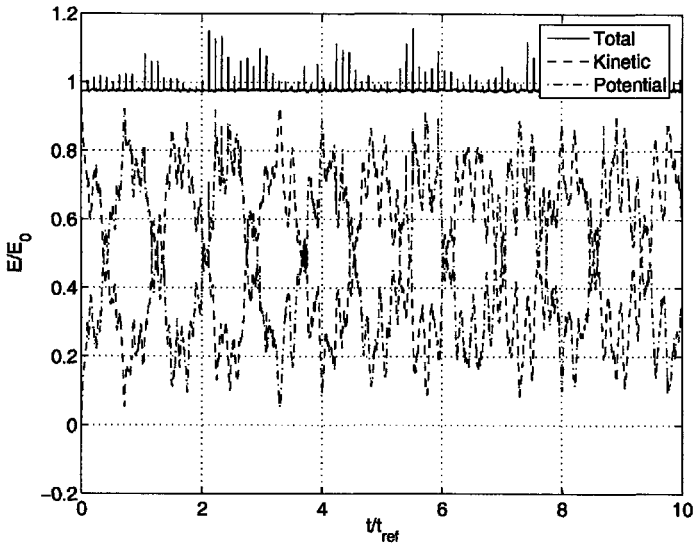

Figure 5-11: Energy history with many node movements.

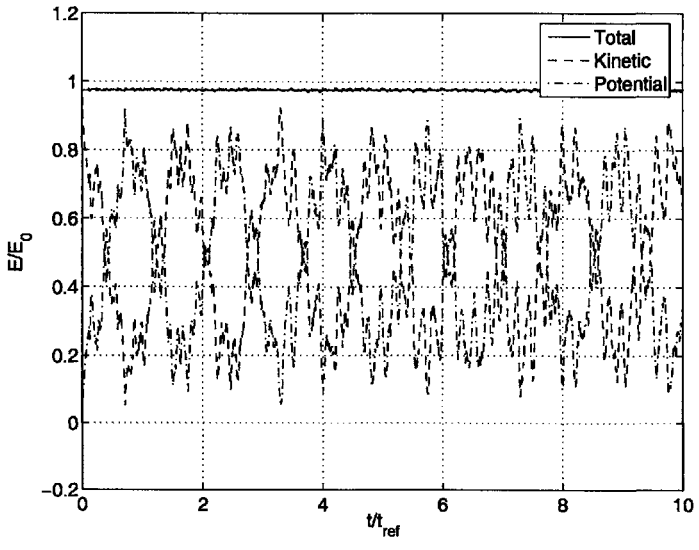

Figure 5-12: Energy history with no node movements.

The beam bending case was computed using a pressure stabilization $\frac{1}{\kappa^*} = \epsilon = 10^{-5}$ without which some chequered boarding type of mechanism in pressure was observed.

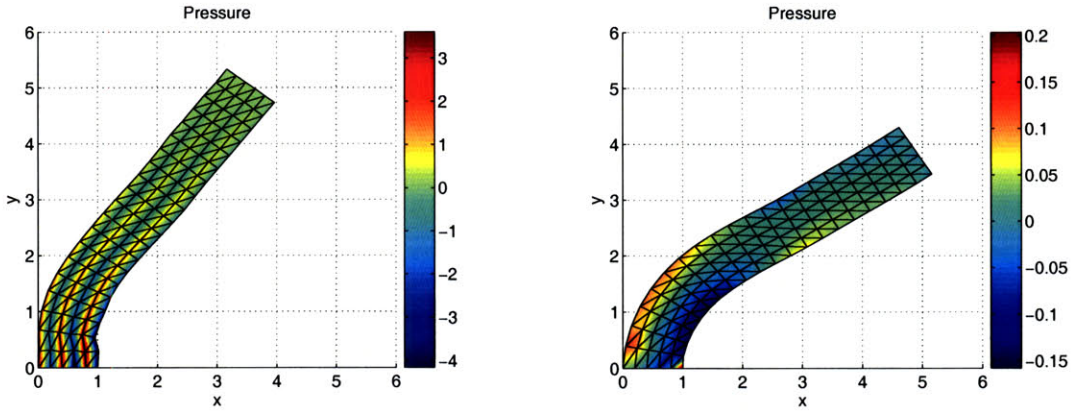

Figure 5-13: Incorrect pressure distribution(left) corrected by the use of pressure stabilization (right).

5.4 Concluding remarks

The combined algorithm worked as expected. The conservation properties of the fractional time-step method and the adaptation procedures could be combined, leading to an overall momentum conserving algorithm. There were some approximations within the pressure update step, in spite of which the momentum remained conserved, as would be expected of the Variational formulation, since the stationarity with respect to $\boldsymbol{x}_n$ was not disturbed. Although such approximation does introduce some first order errors in the pressure update, leading to errors in the total energy, these errors are reduced with mesh refinement.

Similar algorithms could be formulated, in case of other mesh adaptation procedures explained in chapter 3, which in principle may not be very simple to implement. Probably most of them could be simplified using some approximations in the pressure update part, enabling them to be implemented with ease.

Chapter 6

Conclusions

6.1 Summary

This thesis has developed upon the variational time integrators described in [5, 7, 11, 10] and other researchers, to extend to mesh-adaptation. With rapid-dynamics in mind, the developments have been in the realm of explicit methods and linear elements. Non linear effects due to large deformations/rotations and non-linear material property as that of hyperelastic materials have been incorporated and demonstrated satisfactorily. Simplified algorithms for local remeshing techniques like that of diagonal swapping, edge-splitting, node movement and edge collapsing have been developed and used together in conjunction with the time-integration algorithm, leading to effective mesh adaptation. Simple mesh adaptation criteria as that of Z^2 error-estimate [46, 47], have been used to obtain effective adaptation. Although advanced adaptation criteria like that of [48, 49] could be used for better adaptation. In all these processes, the linear and angular momentum were conserved exactly as ensured by the variational framework. Such mesh adaptation can be extremely useful in augmenting the performance of existing explicit codes like [1, 2, 3, 4] etc. The adaptation procedures come with minimal change to any explicit code structure.

The next contribution of this thesis has been in the development of a new Fractional time-step method for incompressible and nearly incompressible Lagrangian Dynamics, [71]. This method is built upon the variational statement incorporating the mixed formulation, where along with the position vectors, the pressure is an additional unknown at each node.

This method involves a fractional time step algorithm, where the first step is an explicit update of positions. Then an implicit step in pressure leads to the desired pressure increments. Another explicit update in positions, gives the final solution of positions and pressure. The implicit step leading to the pressure update has been obtained by linearizing the non-linear changes of volume $(J-1)$ to a linear formulation in terms of a divergence of velocity, $(\nabla \cdot \boldsymbol{v})$, leading to a simple "Poisson-like" set of equation which is easily solved at each step. Linear and Angular momentum gets conserved exactly during the time marching, making this method very suitable for rapid dynamics problems. The maximum allowable time-step depends solely on the shear wave speed and the mesh size, hence making it capable of solving completely incompressible cases. Significant advantage over standard explicit methods is obtained near the incompressibility limit, and advantage over implicit methods is found in the case of 3-D problems.

Another contribution of this thesis is the development of a combined algorithm, using the Fractional time-step method and node movement. This method can handle incompressible and nearly incompressible material behaviour. The method variationally consistent and hence conserves linear and angular momentum. It involves simple operations, and hence can be incorporated into existing codes with very few modifications. The method described in this thesis can be used for 2-D and 3-D cases. Node movement could be based on different error-estimators, chosen by the analyst. Recent research found in [39, 55] gives an example of global node movement, using error-estimates based on configurational error. Although elegant, global node movement becomes expensive due to it's implicit nature, whereas the method described in this thesis is reasonably inexpensive and easy to implement.

In this thesis, a variational stabilization term has been developed, which can be generically used in explicit methods. Such stabilization are typically required in explicit methods for rapid dynamics, due to large dispersive errors over long-time-integrations. The stabilization terms do not affect the conservation properties of the methods. Although being viscous in nature the effects on energy are minimal over long time integrations, as the energy decay rate is shown to be higher-order in the meshsize h. Nevertheless, it is still remains quite effective in reducing higher frequency noise in the solution, and has been observed to be effective in both linear and non-linear problems, some of which are presented in this thesis.

Another contribution of this thesis has been the development of the space-time discretization for variational integrators. Variational formulations require the integration of the kinetic and potential energy to formulate the discrete Lagrangian involving a space-time volume within time levels t_n and t_{n+1}. In this thesis, the space-time volume is subdivided into four-noded-tetrahedra wherein linear interpolation is used for integrating the kinetic and potential energy in time. It has been shown in this thesis, that for prismatic space-time volumes, this subdivision leads to the standard central difference scheme (leap-frog method) with lumped masses. This can be further extended to higher order methods using higher order interpolations. Extensions to 3D problems (involving four dimensional space-time volumes), although hard, will be pursued in the future.

6.2 Future work

Several directions open-up after the developments mentioned in this thesis. The following are a few directions that could be thought of in the immediate future:

- **Adaptation and Fractional time-step method:** Node movement and fractional time-step have been combined successfully. Other operations like that of diagonal swapping, edge splitting, edge collapsing could also be combined to allow full scale mesh adaptation, as shown in chapter 3.

- **Error Estimators:** Simple error-estimators have been used for mesh adaptation. Advanced ideas in error-estimation and adaptation criteria as found in [48, 49] can be used for more accurate error-reduction.

- **Extension to 3D:** The fractional time-step is generically applicable to 2D and 3D problems as shown in [71]. The combined algorithm with the fractional time-step method and the node movement is also applicable to 2D and 3D problems. Some operations like diagonal swapping, edge-splitting and edge-collapsing are designed only for 2D cases. 3D extensions from a variational framework would involve, complicated space-time-discretizations, which would be very challenging as well as of great interest.

- **Material Properties:** Although non-linear cases have been considered all throughout the thesis, some more complex material models as that of plasticity and/or viscoelasticity need to be studied. Some of these complex material behaviour involve information of state variables, which are evaluated and stored at the element. In case of mesh changes special attention would be necessary in transfer of state variables from the old mesh to the new mesh, which will be considered in future.

Bibliography

[1] J. O. Hallquist. Preliminary user's manual for dyna3d and dynap. Technical Report UCID-17268, University of California, Lawrence Livermore Laboratory, Livermore, California., 1976.

[2] J. O. Hallquist. Dyna2d - an explicit finite element and finite difference code for axisymmetric and plane strain calculations (user's guide). Technical Report UCRL-52429, University of California, Lawrence Livermore Laboratory, Livermore, California., March 1978.

[3] W. L. Cheng, R. R. Verderber, and J. O. Hallquist. Three-dimensional simulation of forging processes. *ASME Comput. Eng. Div. Ced.*, 5:95–100, 1992.

[4] S. W. Attaway, B. A. Hendrickson, S. J. Plimpton, D. R. Gardner, C. T. Vaughan, K. H. Brown, and M. W. Heinstein. A parallel contact detection algorithm for transient solid dynamics simulations using pronto3d. *Computational Mechanics*, 22:143–159, 1998.

[5] Kane C., Marsden J. E., Ortiz M., and West M. Variational integrators and the newmark algorithm for conservative and dissipative mechanical systems. *Int. J. Num. Meth. Engrg.*, 49:1295–1325, 2000.

[6] Zienkiewicz O. C., Rojek J., Taylor R. L., and Pastor M. Triangles and tetrahedra in explicit dynamic codes for solids. *Int. J. Num. Meth. Engrg.*, 43:565–583., 1998.

[7] Wendlandt J. and Marsden J. E. Mechanical integrators derived from a discrete variational principle. *Physica D*, 106:223–246, 1997.

[8] Ortiz M. A note on energy conservation and stability of nonlinear time-stepping algorithms. *Computers and Structures*, 24:167–168, 1986.

[9] Veselov A.P. Integrable discrete-time systems and difference operators. *Functional Analysis and its Applications*, 22:83–94, 1988.

[10] A. Lew, J. E. Marsden, M. Ortiz, and M. West. Asynchronous variational integrators. *Arch. Rational. Mech. Anal.*, 167(2):85–146, April 2003.

[11] Marsden J. E., Pekarsky S., and Shkoller S. Discrete euler-poincaré and lie-poisson equations. *Nonlinearity*, 12:1647–1662, 1999.

[12] Gonzalez O. Time integration and discrete hamiltonian systems. *Journal of Nonlinear Science*, 6:449–469, 1996.

[13] Gonzalez O. and Simo J. C. On the stability of symplectic and energy-momentum algorithms for non-linear hamiltonian systems with symmetry. *Comp. Meth. in Appl. Mech. Engrg.*, 134(3-4):197–222., 1996.

[14] Cornelius Lanczos. *The Variational Principles of Mechanics.* Dover, 1986.

[15] Jerrold E. Marsden and Thomas J. R. Hughes. *Mathematical Foundations of Elasticity.* Dover, 1983.

[16] Simo J. C., Tarnow N., and Wong K. K. Exact energy-momentum conserving algorithms and symplectic schemes for nonlinear dynamics. *Comp. Meth. in Appl. Mech. and Engrg.*, 100:63–116, 1992.

[17] Simo J. C. and Tarnow N. The discrete energy momentum integrators, conserving algorithms for nonlinear elastodynamics. *Zietschrift fuer Argewandte Mathematik und Physik*, 43:757–792, 1992.

[18] Simo J. C. and Gonzalez O. Assessment of of energy-momentum and symplectic schemes for stiff dynamical systems. *Proceesings of ASME Winter Annual Meeting, New Orleans*, December 1996.

[19] Newmark N. M. A method of computation for structural dynamics. *ASCE Journal of Engineering Mechanics Division*, 85:64–94, 1959.

[20] Pijaudier, G. Cabot, L. Bode, and A. Huerta. Arbitrary eulerian lagrangian finite element analysis of strain localization in transient problems. *Int. Journal. for Numerical Methods in Engrg.*, 38:4171–4191, 1995.

[21] P. Diez and A. Huerta. A unified approach to remeshing strategies for finite element analysis. *Comput. Methods Appl. Mech. Engrg.*, 176:215–229, 1999.

[22] M. Papadrakakis, G. Babilis, and P. Braouzi. Efficiency of refinement procedures for the p-version of the adaptive finite element method. *Engineering Computations*, 14(1):98–118, 1997.

[23] R. Radovitzky and Ortiz M. Error estimation and adaptive meshing in strongly non-linear dynamic problems. *Comput. Methods Appl. Mech. Engrg.*, 172(1-2):203–240, 1999.

[24] M. Ortiz and J. J. Quigley. Adaptive mesh refinement in strain localization problems. *Comput. Methods Appl. Mech. Engrg.*, 90:781–804, 1991.

[25] M. Rivara. Local modification of meshes for adaptive and or multigrid finite element methods. *J. Comp. Appl. Math.*, 36:79–89, 1991.

[26] M. Rivara. New longest edge algorithms for the refinement and/or improvement of unstructered triangulations. *Int. Journal. for Numerical Methods in Engrg.*, 40:3313–3324, 1997.

[27] H. L. De Cougny and M. S. Shephard. Parallel refinement of coarsening and refinement of tetrahedral meshes. *Int. J. Numer. Meth. Engng.*, 46:1101–1125, 1999.

[28] L. Freitag and P. Knupp. Tetrahedral element shape optimization via the jacobian determinant and condition number, 1999.

[29] J. F. Molinari and Ortiz. M. Three-dimensional adaptive meshing by subdivision and

edge-collapsing in finite-deformation dynamic-plasticity problems with application to adiabatic shear banding. *Int. J. Numer. Meth. Engng.*, 53:1101–1126, 2002.

[30] G. T. Camacho and M. Ortiz. Adaptive lagrangian modeliing of ballistic penetration of metallic targets. *Comput. Methods Appl. Mech. Engrg.*, 142:269–301, 1997.

[31] T. D. Marusich and M. Ortiz. Modelling and simulation of high speed machining. *Int. J. Numer. Meth. Engng.*, 38:3675–3694, 1995.

[32] R. C. Batra and K. I. Ko. An adaptive mesh refinement technique for the analysis of shear bands in plane strain compression of a thermoviscoplastic solid. *Computational Mechanics*, 10:369–379, 1992.

[33] H. Borouchaki, P. Laug, A. Cherouat, and K. Saanouni. Adaptive remeshing in large plastic strain with damage. *Int. J. Numer. Meth. Engng.*, 63:1–36, 2005.

[34] Somnath Ghosh and Suresh Raju. R-s adapted arbitrary lagrangian-eulerian finite element method for metal forming problems with strain localization. *Int. Journal. for Numerical Methods in Engrg.*, 39:3247–3272, 1996.

[35] S. B. Petersen and P. A. Martins. Finite element remeshing: A metal forming approach for quadilateral mesh generation and refinement. *Int. J. Numer. Meth. Engng.*, 40:1449–1464, 1997.

[36] D. Y. Kwak, J. S. Cheon, and Y. T. Im. Remeshing for metal forming simulations-part i: Two dimensional quadrilateral remeshing. *Int. J. Numer. Meth. Engng.*, 53:2463–2500, 2002.

[37] Tobias Erhart, Wolfgang Wall, and Ekkehard Ramm. Robust adaptive remeshing strategy for large deformation transient impact simulations. *Int. Journal. for Numerical Methods in Engrg.*, 65:2139–2166, 2006.

[38] J. C. A. Costa and M. K. Alves. Layout optimization with h-adaptivity of structures. *Int. J. Numer. Meth. Engng.*, 58:83–102, 2003.

[39] P. Thoutireddy and Ortiz M. A variational r-adaptation and shape-optimization method for finite-deformation elasticity. *Int. J. Numer. Meth. Engng.*, 61:1–21, 2004.

[40] I. Babuska and B. A. Szabo. On the rate of convergence of finite element method. *Int. Journal. for Numerical Methods in Engrg.*, 18:323–341, 1982.

[41] D. W. Kelly, J. Gago, O. C. Zienkiewicz, and I. Babuska. A posteriori error analysis and adaptive processes in the finite element method. *Int. Journal. for Numerical Methods in Engrg.*, 19:1593–1619, 1983.

[42] O. C. Zienkiewicz and J. Z. Zhu. A simple error estimator and adaptive procedure for practical engineering analysis. *Int. Journal. for Numerical Methods in Engrg.*, 24:337–357, 1987.

[43] X. D. Li and N. E. Wiberg. A postprocessed error estimate and an adaptive procedure for the semi-discrete finite element in dynamic analysis. *Int. J. Numer. Meth. Engng.*, 37:3585–3603, 1994.

[44] G. M. Hulbert and I. Jang. Automatic time-step control algorithms for structural dynamics. *Comput. Methods Appl. Mech. Engrg.*, 126:155–178, 1995.

[45] Thomas Grätsch and Klaus-Jürgen Bathe. A posteriori error estimation techniques in practical finite element analysis. *Computers and Structures*, 83:235–265, 2005.

[46] O. C. Zienkiewicz and J. Z. Zhu. The superconvergent patch recovery and a-posteriori error estimates, part 1: The recovery technique. *Int. Journal. for Numerical Methods in Engrg.*, 33:1331–1364, 1992.

[47] O. C. Zienkiewicz and J. Z. Zhu. The superconvergent patch recovery and a-posteriori error estimates, part 2: Error estimates and adaptivity. *Int. Journal. for Numerical Methods in Engrg.*, 33:1365–1382, 1992.

[48] Pierre Ladevéze and Nicolas Moës. A new *a posteriori* error estimation for nonlinear time-dependant finite element analysis. *Comput. Methods Appl. Mech. Engrg.*, 157:45–68, 1997.

[49] J. P. Combe, Pierre Ladevéze, and J. P. Pelle. Discretization error estimation for transient dynamic simulation. *Advances in Engineering Software*, 33:553–563, 2002.

[50] Pierre Ladevéze and J. P. Pelle. *Mastering Calculations in Linear and Nonlinear Mechanics.* Springer, Mechanical Engineering Series, 2004.

[51] I. Romero and L. M. Lacoma. A methodology for the formulation of error estimators for time integration in linear solid and structural dynamics. *Int. J. Numer. Meth. Engng.*, 66:635–660, 2006.

[52] Weizhang Huang. Variational mesh adaptation: isotropy and equidistribution. *J. Comput. Phys.*, 174(2):903–924, 2001.

[53] Weizhang Huang and Weiwei Sun. Variational mesh adaptation ii: error estimates and monitor functions. *J. Comput. Phys.*, 184(2):619–648, 2003.

[54] W. Cao, R. C. Gonzalez, W. Huang, and R. D. Russell. Variational mesh adaptation methods for axisymmetrical problems. *SIAM J. Numer. Anal.*, 41(1):235–257, 2003.

[55] Gurtin, M.E. *Configurational Forces as Basic Concepts of Continuum Physics.* Springer, New York, 2000.

[56] E. Stein (ed.). *Error-Controlled Adaptive FEMs in Solid Mechanics.* Wiley, 2003.

[57] R. Lohner, K. Morgan, and O. C. Zienkiewicz. An adaptive finite element procedure for compressible high speed flows. *Comput. Methods Appl. Mech. Engrg.*, 51:441–465, 1985.

[58] R. Lohner. Adaptive remeshing for transient problems. *Comput. Methods Appl. Mech. Engrg.*, 75:195–214, 1989.

[59] J. Peraire, M. Vahdati, K. Morgan, and O. C. Zienkiewicz. Adaptive remeshing for compressible flow computations. *J. Comp. Phys.*, 72:449–466, 1987.

[60] O. Hassan, E. J. Probert, K. Morgan, and J. Peraire. Mesh generation and adaptivity for the solution of compressible viscous high speed flows. *Int. Journal. for Numerical Methods in Engrg.*, 38:1123–1148, 1995.

[61] E. J. Probert, O. Hassan, and K. Morgan. An adaptive finite element method for transient compressible flows with moving boundaries. *Int. Journal. for Numerical Methods in Engrg.*, 32:751–765, 1991.

[62] J. Stewart, A. R. Thareja, R. R. Wieting, and K. Morgan. Application of finite elements and remeshing techniques to shock interference on a cylindrical leading edge. *AIAA Paper*, 87-0032, 1988.

[63] O. C. Zienkiewicz and J. Wu. Automatic directional refinement in adaptive analysis of compressible flows. *Int. Journal. for Numerical Methods in Engrg.*, 37:2189–2210, 1994.

[64] M. Parashivoiu, J. Peraire, and A. T. Patera. A posteriori finite element bounds for linear functional outputs of elliptic partial differential equations. *Comput. Methods Appl. Mech. Engrg.*, 150:289–312, 1997.

[65] D.A. Venditti and D.L. Darmofal. Anisotropic grid adaptation for functional outputs: application to two-dimensional viscous flows. *J. of Comp. Phys.*, 187:22–46, 2003.

[66] Chorin A. J. Numerical solution of the navier-stokes equations. *Math. Comput.*, 22:745–762, 1968.

[67] Bonet J. and Burton A. J. A simple averaged nodal pressure tetrahedral element for nearly incompressible dynamic explicit applications. *Comm. Num. Meth. Engrg.*, 14:437–449, 1998.

[68] Bonet J., Marriott H., and Hassan O. Stability and comparison of different linear tetrahedral formulations for nearly incompressible explicit dynamic applications. *Int. J. Num. Meth. Engrg.*, 50:119–133, 2001.

[69] J. Bonet, H. Marriott, and O. Hassan. An averaged nodal deformation gradient linear tetrahedral element for large strain explicit dynamic applications. *Comm. Num. Meth. Engrg.*, 17:551–561, 2001.

[70] F. Armero and J. C. Simo. A-priori stability estimates and unconditionally stable product formula algorithms for non-linear coupled thermoplasticity. *International Journal of Plasticity*, 9:149–182, 1993.

[71] S. K. Lahiri, J. Bonet, J. Peraire, and L. Casals. A variationally consistent fractional time-step integration method for incompressible and nearly incompressible lagrangian dynamics. *Int. Journal. for Numerical Methods in Engrg.*, 63:1371–1395, 2005.

[72] Javier Bonet and Richard D. Wood. *Nonlinear continuum mechanics for finite element analysis.* Cambridge University Press, 1997.

[73] Gerhard A. Holzapfel. *Nonlinear Solid Mechanics.* John Wiley & Sons Ltd., 2000.

[74] Ted Belytschko, Wing Kam Liu, and Brian Moran. *Nonlinear Finite Elements for Continua and Structures.* John Wiley & Sons Ltd., 2000.

[75] C. R. Dohrmann, M. W. Heinstein, J. Jung, S. W. Key, and W. R. Witkowski. Node-based uniform strain elements for three node triangular and four-node tetrahedral meshes. *Int. J. Numer. Meth. Engng.*, 47:1549–1568, 2000.

[76] Armero F. and Simo J. C. . Formulation of a new class of fractional step methods for the incompressible mhd equations that retains the long-term dissipativity of the continuum dynamical system. *Fields Institute of Communications*, 10:1–23, 1996.

[77] O. C. Zienkiewicz and J. Z. Zhu. Analysis of the zienkiewicz-zhu *a-posteriori* error estimator in the finite element method. *Int. Journal. for Numerical Methods in Engrg.*, 28:2161–2174, 1989.

[78] O. C. Zienkiewicz and J. Z. Zhu. Error estimates and adaptive refinement for plate bending problems. *Int. Journal. for Numerical Methods in Engrg.*, 28:2839–2853, 1989.

[79] F. Armero and E. Petocz. Formulation and analysis of conserving algorithms for dynamic contact/impact problems. *Comput. Methods Appl. Mech. Engrg.*, 158:269–300, 1998.

[80] F. Armero and E. Petocz. A new dissipative time-stepping algorithm for frictional contact problems: Formulation and analysis. *Comput. Methods Appl. Mech. Engrg.*, 179:151–178, 1999.

[81] W. E. Carrol and R. M. Barker. A theorem for optimum finite element idealizations. *Int. Journal. for Numerical Methods in Engrg.*, 9:883–895, 1973.

[82] I. Babuska and M. Suri. The p and h version of the finite element: an overview. *Comput. Methods Appl. Mech. Engrg.*, 82:5–26, 1990.

[83] O. C. Zienkiewicz and A. W. Craig. Adaptive refinement, error estimates, multigrid solution and hierarchic finite element method concept. *Accuracy Estimates and Adaptivity for Finite Element.*, pages 25–59, 1986.

[84] J. T. Oden, L. Demkowwicz, W. Rachaowicz, and T. A. Westermann. Toward a universal h-p adaptive finite element strategy - part 2. a posteriori error adaptation. *Comput. Methods Appl. Mech. Engrg.*, 77:113–180, 1989.

[85] R. Actis, B. Szabo, and C. Schwab. Hierarchic models for laminated plates and shells. *Comput. Methods Appl. Mech. Engrg.*, 172:79–107, 1999.

[86] O. J. B. A. Pereira, J. P. M. Almeida, and E. W. A. Maunder. Adaptive methods for hybrid equilibrium finite element methods. *Comput. Methods Appl. Mech. Engrg.*, 1-4:19–39, 1999.

[87] G. L. Goudreau and J. O. Hallquist. Recent developments in large scale lagrangian hydrocodes. *Comput. Methods Appl. Mech. Engrg.*, 33:725–757, 1982.

[88] G. C. Bessette, E. B. Becker, L. M. Taylor, and D. L. Littlefield. Modeling of impact problems using an h-adaptive, explicit lagrangian finite element method in three dimensions. *Comput. Methods Appl. Mech. Engrg.*, 192:1649–1679, 2003.

[89] Klaus-Jürgen Bathe. *Finite Element Procedures.* Prentice Hall Inc., New Jersey, USA., 1996.